

Winter 2007

Prediction of interference Pathloss Inside Commercial Aircraft Using Modulated Fuzzy Logic and Neural Networks

Madiha Jamil Jafri
Old Dominion University

Follow this and additional works at: https://digitalcommons.odu.edu/ece_etds

 Part of the [Electrical and Computer Engineering Commons](#)

Recommended Citation

Jafri, Madiha J.. "Prediction of interference Pathloss Inside Commercial Aircraft Using Modulated Fuzzy Logic and Neural Networks" (2007). Doctor of Philosophy (PhD), dissertation, Electrical/Computer Engineering, Old Dominion University, DOI: 10.25777/w6x2-7g98
https://digitalcommons.odu.edu/ece_etds/83

This Dissertation is brought to you for free and open access by the Electrical & Computer Engineering at ODU Digital Commons. It has been accepted for inclusion in Electrical & Computer Engineering Theses & Dissertations by an authorized administrator of ODU Digital Commons. For more information, please contact digitalcommons@odu.edu.

**PREDICTION OF INTERFERENCE PATHLOSS INSIDE COMMERCIAL
AIRCRAFT USING MODULATED FUZZY LOGIC AND NEURAL NETWORKS**

by

Madiha Jamil Jafri

B.S. December 2003, Old Dominion University, Norfolk, Virginia

M.S. August 2004, Old Dominion University, Norfolk, Virginia

A Dissertation Submitted to the Faculty of
Old Dominion University in Partial Fulfillment of
the Requirements for the Degree of

DOCTOR OF PHILOSOPHY

ELECTRICAL AND COMPUTER ENGINEERING

OLD DOMINION UNIVERSITY

December 2007

Approved by:

Linda Vahala (Director)

Ravindra Joshi (Member)

Frederic McKenzie (Member)

Zia Razzaq (Member)

ABSTRACT

PREDICTION OF INTERFERENCE PATHLOSS INSIDE COMMERCIAL AIRCRAFT USING MODULATED FUZZY LOGIC AND NEURAL NETWORKS

Madiha Jamil Jafri
Old Dominion University, 2007
Director: Dr. Linda Vahala

Although several modeling techniques have been used to model indoor radio wave propagation and coupling patterns, to date no efficient model exists that calculates indoor-outdoor radio wave propagations on commercial aircraft. Due to the complexity of an aircraft structure, with the additive introduction of creeping wave phenomenon and unknown back-door propagation values from the exterior aircraft antenna to the avionics bay, numerical modeling approaches using Method of Moments (MoM) or Finite Difference Time Domain (FDTD) prove too complex with limitations. This dissertation presents an expert neuro-fuzzy (NF) model for Interference pathloss (IPL) predictions inside an Airbus 320 (A320) airplane, for radio systems from 75 to 1585 MHz. This novel model generates IPL pattern through fuzzy logic, incorporating linear expert knowledge into the patterns. The model also uses feed-forward neural networks to derive meanings from complicated or imprecise data, extract patterns and detect trends in the IPL data that are too complex to be noticed by either humans or other computer techniques. Unlike previous approaches, the model presented is robust in incorporating both low to high band frequencies. It is also computationally efficient and reliable.

This dissertation is dedicated to . . .

my late grandfather for creating the dream,
my parents for fostering the determination,
and my husband for facilitating the achievement

ACKNOWLEDGEMENTS

There are many people who have contributed to the successful completion of this thesis. I would like to extend a special thanks to my advisor, Dr. Linda Vahala for her support, guidance and patience throughout my research. I would also like to thank Drs. Sacharia Albin, Ravindra Joshi, Frederic McKenzie and Zia Razzaq for being an important part of my defense committee. Many thanks to Linda Marshall for always answering my panicked e-mails and for keeping me on track with paperwork and registration needs at ODU. This research could not have progressed this far without the hard work and tremendous support of Mr. Jay Ely from the NASA Langley Research Center. I would like to sincerely thank him for all of his time spent editing conference papers and for having the patience to teach me the fundamental concepts behind this research. Mr. Ely was instrumental in defining research problems on which I have concentrated.

I would also like to extend a special thanks to the HIRF Lab Team at NASA Langley Research Center for their continuous support and mentorship. Traveling to conferences and test sites as well as personal financial support was made possible by the generous 4-year fellowship program by the NASA Headquarters (Graduate Student Researchers Program). I am further grateful to the personnel at United Airlines, Delta Airlines, Eagles Wings Inc. and NASA's Aviation Safety Program whose joint partnership enabled me to obtain the useful data upon which this work builds.

While attempting to complete this study, I have had the opportunity to work with three very understanding employers. I would like to thank Dr. C. J. Reddy and his staff at Applied EM for their guidance with antenna design theory and complementary access and training to critical modeling software. I would then like to thank Dr. Vince Calhoun (along with his staff and my friends at the MIND Institute) for his rigorous training in my technical writing skills and for broadening my knowledge from pattern prediction in electrical engineering to pattern prediction in complex biological systems, such as the human brain. Finally, I would like to thank my friends and mentors at Lockheed Martin, in particular, Koeunyi Bae and Kenneth Massa, for their tremendous support and understanding during the last phase of this study.

I would like to thank my family for their belief in my abilities that kept me determined, and for their immense assistance, love and support in all other aspects of life. My late grandfather, Siraj-ul-Hassan Jafri, wished for me to one day work for NASA and get a PhD when I was eight years old! His belief in me and the wish always remained with me and guided me to this path ever since elementary school. My parents, Jamil and Ghazala, laid down the nurturing foundation, paid my bills, did my laundry, cooked wonderful food for me and sometimes even spoon-fed me (literally!) during times when I had to sit in front of the computer or study for hours, probably providing me with the most love and least responsibility of any other PhD student. Thank you for doing so much for me without asking for a single favor in return. I could not have come this far without you two. I would also like to thank my siblings and their spouses for showing so much appreciation for my hard work and for being there for me whenever needed: Faiza, Mehdi, Faraz, Aniq, Osman, Amber, and Reda. Special thanks to Reda for being the most responsible little sister and for taking the time to run countless errands for me during my candidacy exam, defense and final dissertation submission. I also appreciate the support provided by my cousins, aunts and uncles, especially my uncle Dr. Jawed Jafri, whose own hard work and sacrifices for his doctorate degree gave me more courage.

Last but not least, a simple thank you is not sufficient for my husband, Hamid, who sacrificed more than two years of his life in doing way too great a share of house chores than he ever bargained for or imagined when taking wedding vows with me. I hope to make up for the lost moments in the many years to come. Thanks for providing me with the love and belief in my abilities which kept me going until the finish line. I would also like to thank Hamid's parents and family for their prayers, humor and support: Tariq and Ruqia (parents), Sarwat and Arif.

TABLE OF CONTENTS

Chapter	Page
1. INTRODUCTION TO MODELING TECHNIQUES AND PROBLEM STATEMENT	
	1
1.1 Review and Evaluation of General Computational Modeling Techniques	1
1.1.1 Finite Element Methods	2
1.1.2 Method of Moments	3
1.1.3 Finite-Difference Time Domain Method	4
1.1.4 Transmission Line Matrix Method	4
1.1.5 Fuzzy Logic	5
1.1.6 Neural Networks	6
1.2 Introduction to EMI Phenomenon onboard Aircraft	7
1.2.1 Classification of Portable Electronic Devices (PEDs)	7
1.2.2 Review of Rules and Regulations of PEDs on Aircraft	8
1.2.3 Threat Assessment Overview of PEDs on board Aircraft	9
1.3 Dissertation Objectives and Scope	11
1.4 Problem Assumptions, Conditions and Contributions	12
 2. DATA ANALYSIS OF ELECTROMAGNETIC INTERFERENCE ON AIRCRAFT	
	14
2.1 Reasons for Vulnerability of Aircraft systems due to PED-related Emissions	14
2.2 Introduction to Aircraft Schematics and Details	16
2.3 Aircraft Systems of Concern	21
2.4 Coupling Phenomenon to Aircraft Systems	22
2.5 Graphical Representation of Collected IPL Data	23

Chapter	Page
3. METHODOLOGY	42
3.1 Overview of Techniques used for EMI prediction inside Commercial Aircraft.....	43
3.1.1 Far Field Techniques.....	44
3.1.2 Method of Moments.....	45
3.1.3 The Finite-Difference Time Domain Method.....	46
3.1.4 Fuzzy Logic	49
3.1.5 Neural Networks	51
3.2 Selected Model's Design Detail.....	52
3.2.1 Input Data Selection.....	52
3.2.2 Neuro Fuzzy Model: System Architecture	60
3.2.3 Neuro-Fuzzy Models' Linear IPL Predictions.....	60
3.2.3.1 Distance Calculations for Fuzzification.....	61
3.2.3.2 Fuzzification: Generation of Rules	67
3.2.3.3 Inference: Application of Rules on Calculations	72
3.2.3.4 Composition: Summation of Fuzzified Outputs	73
3.2.3.5 Defuzzification: Conversion from Fuzzified to Crisp Outputs.....	73
3.2.3.6 Data Reduction.....	75
3.2.4 Neuro-Fuzzy Model's Non-linear IPL predictions	75
4. RESULTS AND EVALUATION OF NFIS EMI MODEL.....	76
4.1 IPL Data Collection.....	76
4.2 Training Data Selection	77
4.3 NFIS Model Results and Evaluation.....	78
4.3.1 IPL Prediction: A320 VHF-L	81
4.3.2 IPL Prediction: A320 DME-L	85
4.4 Comparison and Conclusion on EMI Modeling Techniques.....	89

Chapter	Page
5. CONTRIBUTIONS AND FURTHER RECOMMENDATIONS	91
5.1 Summary of the Contributions.....	91
5.2 Conclusions about the Model Structure.....	92
5.3 Conclusion about NFM.....	92
5.4 Conclusion about Applications Domain.....	93
5.5 Recommendation for Future Work.....	94
 APPENDICES.....	 95
Appendix A: IPL Measurement Overview.....	96
Appendix B: Fuzzy Logic System Definition.....	108
Appendix C: Neural Networks Definition.....	113
Appendix D: Measured IPL Data.....	117
 BIBLIOGRAPHY.....	 140
 VITA.....	 146

NOMENCLATURE

ASRS	Aviation Safety Reporting System
ATC	Air Traffic Control
CW	Continuous Wave
dB	Decibel
DME	Distance Measuring Equipment
EMC	Electromagnetic Coupling
EMI	Electromagnetic Interference
FAA	Federal Aviation Administration
FAR	Federal Aviation Regulation
FCC	Federal Communication Commission
FCR	Federal Communication Regulation
FDTD	Finite-Difference Time Domain
FEM	Finite Element Method
GPS	Global Positioning System
GS	Glideslope
IPL	Interference Pathloss
LOC	Instrument Landing System Localizer
MB	Marker Beacon
MoM	Method of Moment
NFM	Neuro-fuzzy Model
NN	Neural Network
PED	Portable Electronic Device
RF	Radio Frequency
RTCA	Requirement and Technical Concepts of Aviation (Committee)
TCAS	Traffic Alert Collision Avoidance System
TCL	Test Cable Loss
TLM	Transmission Line Matrix
VHF	Very High Frequency (Communication System)
VOR	VHF Omnidirectional System

LIST OF FIGURES

Figure	Page
1. Interference to Avionics from PEDs: ASRS Entries By Year [41].....	10
2. Interior View of an Aircraft Fuselage During Maintenance [44].....	16
3. Interior Schematic of B737 [45].....	17
4. Interior Schematic of B757 [45].....	17
5. Interior Schematic of A319 [45].	17
6. Interior Schematic of A320 [45].	18
7. Antenna Locations on B737 (3-D).	19
8. Possible Antenna Locations for GPS on B737.....	19
9. Antenna Locations of B737.....	20
10. Antenna Locations on B757.....	20
11. Antenna Locations for A319.	20
12. Antenna Locations for A320.	20
13. IPL Data for GS-L in Horizontal Polarization (B737).	25
14. IPL Data for TCAS-U in Vertical Polarization (B737).....	25
15. IPL Data for VHF-L in Vertical Polarization (B737).	25
16. IPL Data for LOC-L in Horizontal Polarization (B737).	25
17. IPL Data for GS-L in Horizontal Polarization (B757).	27
18. IPL Data for LOC-L in Horizontal Polarization (B757).	27
19. IPL Data for TCAS-U in Vertical Polarization (B757).....	28
20. IPL Data for TCAS-L in Vertical Polarization (B757).	28
21. IPL Data for ATC-U in Vertical Polarization (B757).	29
22. IPL Data for ATC-L in Vertical Polarization (B757).	29
23. IPL Data for DME-L in Vertical Polarization (B757).	29
24. IPL Data for MB in Horizontal Polarization (B757).....	29
25. IPL Data for DME-R in Vertical Polarization (B757).	30
26. IPL Data for GPS-L in Vertical Polarization (B757).	30
27. IPL Data for GPS-L in Horizontal Polarization (B757).	31
28. IPL Data for VHF-R in Vertical Polarization (B757).	31
29. IPL Data for VHF-L in Vertical Polarization (B757).	31

Figure	Page
30. IPL Data for VHF-C in Vertical Polarization (B757).	32
31. IPL Data for VOR-L in Horizontal Polarization (B757).	32
32. IPL Data for GS-L in Horizontal Polarization (A319).	34
33. IPL Data for LOC-L in Horizontal Polarization (A319).	34
34. IPL Data for DME-L in Vertical Polarization (A319).	34
35. IPL Data for VHF-L in Vertical Polarization (A319).	34
36. IPL Data for ATC-B in Vertical Polarization (A319).	35
37. IPL Data for ATC-T in Vertical Polarization (A319).	35
38. IPL Data for VHF-R in Vertical Polarization (A319).	36
39. IPL Data for VHF-C in Vertical Polarization (A319).	36
40. IPL Data for GS-L in Horizontal Polarization (A320).	37
41. IPL Data for LOC-L in Horizontal Polarization (A320).	37
42. IPL Data for DME-L in Vertical Polarization (A320).	37
43. IPL Data for VHF-L in Vertical Polarization (A320).	37
44. IPL Data for ATC-T in Vertical Polarization (A320).	38
45. IPL Data for ATC-B in Vertical Polarization (A320).	38
46. IPL Data for GPS-L in Vertical Polarization (A320).	39
47. IPL Data for GPS-L in Horizontal Polarization (A320).	39
48. IPL Data for VHF-C in Vertical Polarization (A320).	39
49. Mean IPL Data for All Systems in B737.	40
50. Mean IPL Data for All Systems in B757.	40
51. Mean IPL Data for All Systems in A319.	41
52. Mean IPL Data for All Systems in A320.	41
53. Schematic of Current Calculation Using Method of Moments.	45
54. Reduced Aircraft Model.	46
55. Wire Mesh Representation for Method of Moments.	46
56. Reduced Wire Mesh Representation for Method of Moments.	46
57. VHF Prediction in Vertical Polarization using FDTD [53].	48
58. VHF Prediction in Horizontal Polarization using FDTD [53].	48
59. Rectangular Aircraft Model.	49

Figure	Page
60. IPL Pattern Prediction (top) for VHF-L using Fuzzy Logic.	50
61. IPL Pattern Prediction for VHF-L using Neural Networks.....	51
62. Auto-CAD Drawings of B737 [61].....	56
63. Auto-CAD Drawings of B757 [62].....	57
64. Auto-CAD Drawings of A319 [63].....	58
65. Auto-CAD Drawings of A320 [64].....	59
66. Detailed System Architecture for Neuro Fuzzy Model.....	61
67. Flowchart for Linear Module of NFM.	61
68. Distance Calculations from Window to Antenna, Fuselage Mounted.	63
69. Distance Calculations from Window to Antenna, Nose Mounted.	65
70. Distance Calculations from Window to Antenna, Tail Mounted.	66
71. Fuzzy Rule 1a: Coupling with respect to location of Main Exits.	69
72. Fuzzy Rule 1b: Coupling with respect to location of Emergency Exits.	69
73. Fuzzy Rule 2a: Coupling with respect to location of Antenna, nose mounted.	70
74. Fuzzy Rule 2b: Coupling with respect to location of Antenna, fuselage mounted.....	70
75. Fuzzy Rule 2c: Coupling with respect to location of Antenna, tail mounted. ..	70
76. Fuzzy Rule 3a: Coupling with respect to Antenna Polarization, nose mounted, horizontal.....	72
77. Fuzzy Rule 3b: Coupling with respect to Antenna Polarization, tail/fuselage mounted, vertical.....	72
78. Fuzzy Rule 3c: Coupling with respect to Antenna.....	72
79. Demonstration of Fuzzy Inference.	73
80. NN for prediction of Minimum and Maximum IPL values.	74
81. Padding and Mapping of Windows to Distance (cm) (B737).....	79
82. Padding and Mapping of Windows to Distance (cm) (B757).....	79
83. Padding and Mapping of Windows to Distance (cm) (A319).....	80
84. Padding and Mapping of Windows to Distance (cm) (A320).....	80
85. Fuzzified IPL Pattern for VHF-L (A320).....	82
86. Minimum and Maximum IPL Prediction for VHF-L (A320).	82

Figure	Page
87. Defuzzified and Real IPL Pattern for VHF-L (A320).....	82
88. Actual vs. Predicted IPL Pattern for VHF-L (A320).	84
89. Actual, Predicted and Training Data for VHF-L (A320).	84
90. Mean IPL Patterns for VHF-L from all Aircraft (B737, B757, A319, A320). .	85
91. Fuzzified IPL Pattern for DME-L (A320).....	86
92. Minimum and Maximum IPL Prediction for DME-L (A320).	86
93. Defuzzified and Real IPL Pattern for DME-L (A320).	86
94. Actual vs. Predicted IPL for DME-L (A320).	87
95. Actual, Predicted and Training Data for DME-L (A320).	88
96. Mean IPL Patterns for DME-L from all Aircraft (B757, A319 and A320).	88

LIST OF TABLES

Table	Page
1. Summary of Suspected Cases of PED Interference [41].....	10
2. Aircraft Systems of Concern with Operating Frequencies.....	18
3. Aircraft Systems of Concern in the Event of Interference [34].	22
4. Aircraft Characteristics for B737, B757, A319 and A320.	62
5. Available IPL Data.....	77

CHAPTER 1

INTRODUCTION TO MODELING TECHNIQUES AND PROBLEM STATEMENT

Mathematical modeling has been used to describe relationships among the observed variables from a system for decades [1]. It is an extremely useful tool for studying different types of observable processes in nature and to link observations together into some pattern [1, 2]. In this dissertation, a novel combination of neural networks and fuzzy logic (neuro-fuzzy model) is proposed, which is applied to the modeling of electromagnetic interference (EMI) onboard commercial aircraft. The proposed neuro-fuzzy model has a wide application area; however, EMI patterns inside the aircraft are selected to be modeled to help scientists and engineers better understand the electromagnetic wave propagation phenomenon due to portable electronic devices (PEDs) inside commercial aircraft. This research should assist in understanding coupling characteristics due to PED emissions with aircraft systems in order to assist in making better rules and regulations regarding the use of PEDs on aircraft. A few numerical techniques, previously used for modeling the EMI problem, are also reviewed and conclusions have been presented to consider why these techniques are not as effective for the application of concern.¹

1.1 Review and Evaluation of General Computational Modeling Techniques

Computer techniques have revolutionized the way in which electromagnetic problems are analyzed. Antenna and microwave engineers rely heavily on computer methods to analyze and help evaluate new designs and design modifications. Computer methods for analyzing problems in electromagnetics generally fall into one of three categories: analytical techniques, numerical techniques and expert systems. Analytical techniques make simplifying assumptions about the geometry of a problem in order to apply a closed-form (or table look-up) solution. Numerical techniques attempt to solve fundamental field equations directly; subject to the boundary constraints posed by the geometry. Expert systems do not calculate the fields directly; rather, they estimate values for the parameters of interest based on a rules database. Analytical techniques can be

¹ MLA Handbook format is followed in this dissertation.

useful tools when the important EM interactions of the configuration can be anticipated. However, most EM problems of interest are too unpredictable to be modeled using this approach.

Numerical techniques generally require more computation than analytical techniques or expert systems, but they are very powerful EM analysis tools. Without making *a priori* assumptions about which field interactions are the most significant, the numerical techniques analyze the entire geometry provided as input. They calculate the solution to a problem based on a full-wave analysis. A number of different numerical techniques for solving electromagnetic problems are available. Each numerical technique is well-suited for the analysis of a particular type of problem. The following sections outline the four major numerical modeling techniques that have been used to analyze EMI source configurations with some success.

Each of the techniques discussed below is best-suited to analyze different configurations. No one technique can be used to model all EMI sources; however, each of these techniques can be applied to a number of EMI source configurations. Two or more of these techniques, collectively, represent a potentially powerful set of tools for the EMI engineer. These four major techniques have been extended to form other new techniques to fit more focused objectives. To limit the scope of this dissertation, these extended techniques (the Generalized multipole technique [3], Conjugate gradient method [4], Boundary element method [5], Uniform theory of diffraction [6], to name a few) will not be discussed in this study. The following sections discuss the major numerical techniques, followed by a discussion of the last type of modeling technique, called expert systems, which includes Fuzzy Logic and Neural Networks.

1.1.1 Finite Element Methods

The Finite Element Methods (FEM) have been in use for many years for a variety of applications and have been recently applied to some EMC problems [7-11]. These are a volume-based technique where the solution space is split into small elements, referred to as the finite element mesh. The field in each element is approximated by low order polynomials with unknown coefficients. These approximation functions are substituted into a variational expression derived from Maxwell's equations, and the resulting system

of equations is solved to determine the coefficients. Once these coefficients are calculated, the fields are then determined within each element.

The major advantage that FEM have over other modeling techniques stems from the fact that the electrical and geometrical properties of each element can be defined independently. This permits the problem to be set-up with a large number of small elements in regions of complex geometry and fewer, larger elements in relatively open regions. Thus, it is possible to model configurations that have complicated geometries and many arbitrarily-shaped dielectric regions in a relatively efficient manner. Commercial FEM codes are available that have graphical user interfaces (GUIs) [12].

The FEM are well-suited for shielding applications with apertures. However, as volume-based techniques, these are not well-suited for applications with long wires or applications with long distances between the model and the measurement location. In the complex and large aircraft structure, the entire volume must be broken into smaller elements causing the memory requirements to far exceed normal computer resources (less than 3 GB in memory). Therefore, FEM are not considered to be a possible modeling option for the EMC problem for this dissertation.

1.1.2 Method of Moments

Like FEM analysis, the method of moments (MoM) is a technique for solving complex integral equations by reducing them to a system of simpler linear equations. In contrast to the variational approach of the FEM, however, MoM employs a technique known as the method of weighted residuals. The concept of MoM was largely popularized by Harrington [13]. The technique commonly uses a full-wave frequency-domain approach whereby the radio frequency (RF) currents are found everywhere on a metal structure due to a specified source. Once the currents are known, the radiated fields can be found by summing the contribution from each current element.

MoM techniques applied to integral equations are not very effective when applied to arbitrary configurations with complex geometries or inhomogeneous dielectrics. They are also not well-suited for analyzing the interior of conductive enclosures. Nevertheless, MoM techniques do an excellent job of analyzing a wide variety of important three-dimensional electromagnetic radiation problems with long-wires or in applications with appreciable distances to the observation point. Several non-commercial

general-purpose MoM computer programs are available [5, 13-16]. The MoM technique is more applicable to EMC study onboard large aircraft, and will, therefore, be studied in more detail in later chapters.

1.1.3 Finite-Difference Time Domain Method

The finite-difference time domain (FDTD) method has become very popular for EMI and EM coupling (EMC) problems over the past few years. FDTD is a full-wave, volume-based approach, where the volume of space containing the problem is partitioned into small cubes, and Maxwell's equations are solved directly using a central difference scheme. The FDTD utilizes a time-stepping, or "leap frog", approach where inputs are time-sampled analog signals. The region being modeled is represented by two interleaved grids of discrete points. One grid contains the points at which the magnetic field is evaluated, while the second grid contains the points at which the electrical field is evaluated [17].

In the FDTD method, because the basic elements are cubes, curved surfaces on a scatterer must be stair-cased. For many configurations, this does not present a problem; however, for configurations with sharp, acute edges, an adequately staircased approximation may require a very small grid size. This can significantly increase the computational size of the problem. Therefore, the FDTD technique is not practical for applications with long wires or applications with long distances between the source and the measurement location because of the amount of computer memory required. However, due to the partitioning into small cubes, the material parameters (conductivity, permeability and permittivity) can be specified as necessary. The inside of the enclosure can be as complex as necessary. The possibility of computing EM propagation in a complex cavity makes FDTD a good candidate for the EMC problem in this dissertation; therefore, it will be studied in more detail in later chapters.

1.1.4 Transmission Line Matrix Method

The Transmission Line Matrix (TLM) method is similar to the FDTD method in terms of its capabilities, but its approach is unique. A general overview of the TLM method and a two-dimensional TLM code is provided in a book by Hofer [18]. Like FDTD, analysis is performed in the time domain and the entire region of the analysis is gridded. Instead of interleaving the E-field and H-field grids, however, a single grid is

established and the nodes of this grid are interconnected by virtual transmission lines. These coupled transmission lines are used to solve for voltages and currents within the transmission line structure. Once the final solution is found, the voltages and currents are converted into electrical and magnetic fields .

Although TLM can be used for aperture modeling (as in the case of FDTD), it is best suited for applications where direct connection of lumped circuit elements are needed (as in the case of printed circuit boards). The TLM method is not well-suited for applications with long wires or long distances between the source and the measurement location for the same reason as the FDTD technique. Due to the lack of applicability to EMC-related computation on aircraft, the TLM method will not be further discussed.

1.1.5 Fuzzy Logic

The concept of Fuzzy Logic was conceived by Lotfi Zedah [20] who presented a way of processing data by allowing partial set membership rather than crisp set membership. Fuzzy Logic is a problem-solving control system methodology that can be implemented in hardware, software, or a combination of both. Fuzzy Logic's approach to control problems mimics how a person would make decisions, only much faster.

The four-step fuzzy reasoning procedures employed by applications include fuzzification, which establishes the fact base of the fuzzy system. It identifies the input and output of the system and then identifies the appropriate if-then rules and uses raw data to derive a membership function. At this point, one is ready to apply fuzzy logic to the system. As inputs are received by the system, inference, the second step, evaluates all if-then rules and determines their truth values. If a given input does not precisely correspond to an if-then rule, then partial matching of the input data is used to interpolate an answer. The third step is composition, which combines all fuzzy conclusions obtained by inference into a single conclusion. Different fuzzy rules might have different conclusions, so it is necessary to consider all rules. There are a number of composition methods available. The final step of defuzzification converts the fuzzy value obtained from composition into a "crisp" value; this process is often complex since the resulting fuzzy set might not translate directly into a crisp value. Defuzzification is necessary, since controllers of physical systems require discrete signals [21].

Expert systems are often discarded for EMC modeling due to the complexity of EM wave propagation phenomenon. Tayarani [22] was able to successfully predict the input impedance of a monopole antenna using fuzzy logic. Furthermore, fuzzy logic was successfully used to replace the traditional FEM approach in a cylinder rubber compression problem [9]. The prediction of complex impedance along with replacement of traditional analytical techniques provides a promising future for using fuzzy logic to predict EMC propagation phenomenon on large aircraft from measured data. Furthermore, EMC wave propagation has been predicted successfully using Fuzzy logic in the Master's thesis of Jafri [23]. The model proposed in this dissertation requires an extensive understanding of fuzzy logic by the reader; therefore, more details on the concept of fuzzy logic can be found in Appendix B.

1.1.6 Neural Networks

Neural Networks (NNs) are another form of expert system and process information in a similar way the human brain does. With the remarkable ability to derive meanings from complicated or imprecise data, the NNs can be used to extract patterns and detect trends that are too complex to be noticed by either humans or other computer techniques. A trained neural network can be thought of as an "expert" in the category of information it has been given to analyze. This expert can then be used to provide projections given new situations of interest and answer "what if" questions. The network is composed of a large number of highly interconnected processing units (neurons) working in parallel to solve a specific problem. It has great ability to learn and then generalize. These two most important properties make neural networks good candidates to solve complex, large-scale problems [24, 25].

In the work reported in reference [26], full wave electromagnetic models of microwave components are replaced with NNs, which map devices' physical and geometrical parameters (inputs) to devices' S-parameters (outputs) through training. This successful mapping, along with other related work [27, 28], provides a promising future for the use of NNs for EMC wave propagation modeling. The reader is expected to be knowledgeable about the functionality of NNs and how they are implemented in MATLAB's Neural Networks Toolbox. A brief overview of NN functionality can be found in Appendix C.

1.2 Introduction to EMI Phenomenon onboard Aircraft

A major contribution of this dissertation is a comparative analysis of numerical models with expert systems and to effectively generate the best modeling technique to be used for predicting EMC patterns onboard commercial aircraft due to the radiation from PEDs. The following sections provide the reader with an overview of various portable electronic devices and their assessment of electromagnetic interference with aircraft antenna systems.

1.2.1 Classification of Portable Electronic Devices (PEDs)

A PED is any electronic device that is capable of receiving, storing or transmitting information without a permanent wired link. PEDs can be classified as either intentional or non-intentional transmitters. Intentional transmitters must transmit a signal to accomplish their function; therefore, they are designed to radiate energy [29]. Typical examples of intentionally transmitting PEDs are cellular phones, wireless local-area networks (such as Bluetooth and IEEE 802.11), personal area networks, Citizens-Band two-way radios, remote control toys, and two-way pagers [30].

The non-intentional transmitters, on the other hand, do not need to transmit a signal to accomplish their function; however, like any electrical device, they emit some level of electromagnetic radiation [31]. Therefore, unintentional transmitters only generate spurious emissions at arbitrary frequencies as a result of their electric and electronic parts. Non-intentional transmitters include portable computers such as laptop computers and personal organizers. Some other examples are system receivers, tape recorders, CD players, handheld TVs, electric shavers, game players, cameras, MP3 players, DVD players and camcorders [30].

Medical devices, such as hearing aids, heart pacemakers, blood pressure monitors, electronic-device-embedded man-made human organs, and other human-body-monitoring sensors and devices are typically non-intentionally transmitting PEDs. However, medical devices with wireless technology, such as RF-activated infusion pumps which can only be programmed by means of a remote RF transmitter, would be classified as intentional transmitters when the remote is being used [30].

1.2.2 Review of Rules and Regulations of PEDs on Aircraft

In the US, regulations and recommendations on airborne use of PEDs are established by the Federal Aviation Administration (FAA), the Federal Communication Commission (FCC) and the Requirements and Technical Concepts for Aviation (RTCA), [30]. The FAA is a government agency responsible for regulating aviation. Its mission is to secure the safety, security, and efficiency of aviation systems during operations partly through the issuance of Federal Aviation Regulations (FARs). The FAA regulation on the airborne operation of PEDs is described in FAR Section 91.21 [32-34]. FAR Section 91.21 was initially established in May, 1961, to prohibit the operation of portable frequency modulated radio receivers aboard US-carrier and US-registered aircraft. Later, laptop computers, electronic games and CD players became items of concern. In the last fifteen years, cell-phone usage onboard aircraft has become an item of further concern. In 1993, the FAA issued an Advisor Circular (AC 91.21-1) (revised in 2000, and again in 2006), which provided guidance to the airlines in establishing compliance to FAR 91.21, as well as recommended procedures for airlines and test criteria for manufacturers [35].

The FCC establishes, and is in charge of, all policies used in governing interstate and international communications by radio, television, wire, satellite and cable. The Federal Communication Regulations (FCRs) are established to obtain maximum effectiveness from the use of the systems in connection with the safety of life and property. The FCRs also apply to the operation of PEDs, if the operation imparts or potentially imparts any negative effect on the operational efficiency of the nation's communication network. The associated regulation is the US code of Federal Regulation (Title 47, Part 22, Subpart H), which states that cell phones, installed in or carried onboard airplanes, must not be used while such airplanes are airborne. Therefore, the FCC prohibits the use of cellular phones on board aircraft while airborne [33, 34, 36].

The RTCA is a private, non-profit organization that develops consensus based recommendations regarding communications, navigation, surveillance, and air-traffic management issues. RTCA serves as a federal advisory committee, and provides its recommendations as the basis of the policy, program and regulatory decision by the FAA. The RTCA released its first report regarding PEDs in 1963 (DO-119) [37], followed by a revised second report in 1988 (DO-199) [38]. In 1992, the US government requested that

the RTCA resolve outstanding questions on PEDs to ensure air safety. The government specified that unnecessary restrictions should not be placed on untested PEDs, and it sought to gain an understanding of multiple effects and emissions from intentional radiators, such as remote-control devices and cell phones [30]. In 1996, the committee issued its report (DO-233), which made the recommendation of modifying FAR 91.21 so that the use of any PED is prohibited on airplanes during any critical phase of flight; and so that the use of any PED having the capability to intentionally transmit electromagnetic energy is prohibited in an airplane at all times, unless testing has been conducted to ascertain its safe use. Furthermore, the report recommended additional research and PED testing efforts, as well as in increasing public awareness campaign on the potential hazards from PEDs [39].

1.2.3 Threat Assessment Overview of PEDs on board Aircraft

Despite the existence of various authorities responsible for putting limitations on the use of PEDs on aircraft, passengers still question the existence of an interference problem onboard aircraft due to the use of PEDs. The electromagnetic emissions from the passenger-carried PEDs on commercial airplanes have been reported as being suspected or sometimes confirmed as being responsible for anomalous events during flight. The operation of PEDs produces electromagnetic emissions that can interfere with the airplane systems.

There are a number of databases which have been established to collect potential or actual accident information involving aircraft. The best known is FAA's Aviation Safety Reporting System (ASRS), run by NASA, wherein avionics problems that may have resulted from the influence of passenger electronic devices are recorded [40]. The incidents in ASRS are submitted voluntarily, and the information provided by the reporter is not investigated further.

Figure 1 summarizes the incident entries in the ASRS by the year. Using the ASRS database, this figure has been updated from the figure presented in Strauss' work which included incidents reported up to year 2000 [41]. One of the important limitations of the reported incidents includes the lack of knowledge about underreporting. Underreporting can be influenced by reports being filed elsewhere, the event not being recognized as interference, or the flight crew not attaching significance to the event.

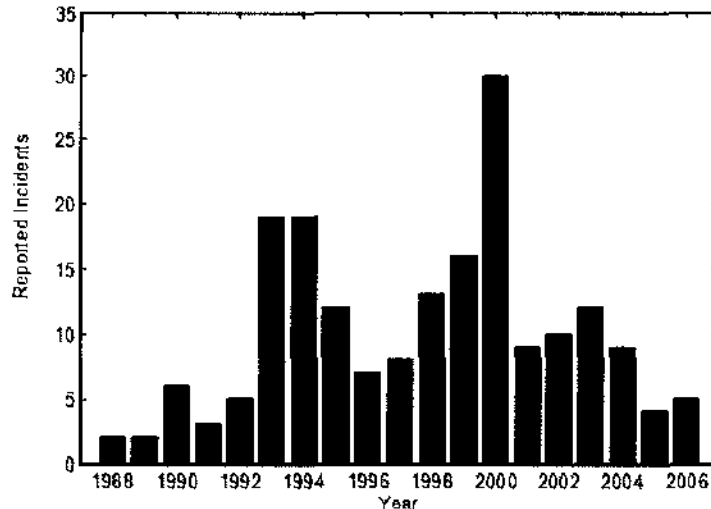


Figure 1. Interference to Avionics from PEDs: ASRS Entries By Year [41].

As analyzed by Strauss, the peak entry in the figure first appears in 1993, coinciding with Congressional interest that prompted RTCA DO-233. Entries declined over the next few years, coinciding with airlines' adoption of policies that require passengers to turn off PEDs below 10,000 ft. After 1996, the trend appears to increase, possibly due to the increasing number of flights, consumer electronic proliferation, aging aircraft systems, and/or passenger non-compliance with airline policies.

Table 1 provides a sampling of suspected cases of PED interference, along with the systems affected and the suspected device up to year 1999 from [41]. The most cited combination of PED-Avionics interference was from cellular phones affecting the VOR navigation system. Cellular phones and laptops computers were involved in the 4 most frequent combinations.

Table 1. Summary of Suspected Cases of PED Interference [41].

PED Used – Avionics Affected	Occurrences
Cellular Phones – VOR	20
Laptop – VOR	15
Cellular Phones – Navigation	9
Laptop – Navigation	9
Electronic Game – VOR	8
Cellular Phone – ILS	6
Cellular Phone – Aircraft radio	6
AM/FM Radio – VOR	6
AM/FM Radio – Navigation	5

The analysis presented in this section confirms that there is indeed proof of the presence of interference onboard commercial aircraft due to passengers' use of PEDs. Since the interference phenomenon is hazardous and difficult, if not impossible, to replicate during flight, it is crucial to understand the problem more critically to possibly locate where the probability of interference due to PEDs is the highest onboard aircraft.

1.3 Dissertation Objectives and Scope

The major objectives of this study may be separated into two parts. Part I is an inverse modeling approach, involving the building of a system model through analysis of the measured data. The measured data includes interference pathloss (IPL) data, obtained through the cooperative agreement between NASA Langley Research Center, Eagles Wing Incorporated, United Airlines and Delta Airlines. This type of data is used because it provides a good understanding of coupling throughout the airplane. The measurement of IPL data is also standardized throughout the aviation industry. IPL data collection has been previously published in various references by the author [23, 27, 28, 42, 43]. The detailed technique of obtaining IPL data is also included in Appendix A of this dissertation. Chapter 2 of the dissertation includes a detailed graphical analysis of the IPL data collected to date on Boeing 737 (B737), B757, Airbus 319 (A319) and A320. The details in chapter 2 will enable the reader to comprehend and gain 'expert knowledge' on the EMI phenomenon on selected aircraft as well as become introduced to the various challenges which need to be resolved before modeling the EMI patterns.

Part II of the objectives involve the neuro-fuzzy modeling of the IPL data inside aircraft using combinatory modeling approaches of fuzzy logic and neural networks. In order to achieve these objectives, chapter 3 includes an overview of previous techniques used for modeling the EMI phenomenon and provides the advantages as well as limitations of these techniques. This chapter then proposes the novel architecture of neuro-fuzzy model which overcomes many of the limitations of previous models. The neuro-fuzzy model is then evaluated in chapter 4 by comparing the actual IPL patterns in chapter 2 to the simulated and predicted results from the model. The final chapter summarizes the contributions in this study for researchers, as well as includes proposed improvements which shall further assist in understanding and prediction with EMI phenomenon onboard commercial aircraft.

1.4 Problem Assumptions, Conditions and Contributions

All modeling techniques are based on some assumptions; some are large while others are smaller and more reasonable. When evaluating the model, the practicality of the assumptions for the model must be compared to the validity of the model's output with actual measured results. The neuro-fuzzy model proposed in this study is based upon the following assumptions:

1. The measured IPL data is accurate and within acceptable levels of experimental error.
2. The trends observed in the measured IPL data are accurate and repeatable if verified with further experimental trials.
3. Aircraft dimension and characteristics (i.e. number and location of doors and windows) are available to be used during modeling.
4. Aircraft antenna position and characteristics (i.e. location and polarization characteristics) are available to be used during modeling.

After accepting the above assumptions, the model is developed under the following conditions and requirements:

1. The model shall be computationally efficient, producing results in less than an hour on a standard laptop (instead of a supercomputer).
2. The model shall be reliable, producing repeatable results.
3. The model shall utilize the expert knowledge of EMI engineers, who have analyzed IPL data extensively and have made expert observations that may not be summarized in simple calculations.
4. The model shall be accurate, predicting IPL patterns that resemble the measured IPL patterns closely, including matching the mean, minimum and maximum IPL values in decibels.
5. The model shall have a broad spectrum prediction capability, being able to predict IPL patterns for systems operating in both low and high-band frequencies.

The work presented in this dissertation along with the proposed model is based on the following contributions:

1. The extensively collected IPL data is presented for the first time as part of Appendix D, which includes raw IPL data values on B737, B757, A319 and A320

along with the calibration values used before using the data for modeling. This data can be studied in numerous further studies.

2. A detailed methodology for collected IPL data is presented in Appendix A, which may be used by EMI researchers to further collect IPL data in a similar manner, so that the results may be comparable.
3. The collected IPL data is presented graphically for the first time in one comprehensive study, so that expert knowledge can be gained and IPL patterns among different aircraft structure and antenna systems may be compared.
4. The first effective model is proposed in this study that satisfies all the requirements set above including: efficiency, reliability, incorporation of expert information, accuracy as well as lack of dependency on operating frequencies.

CHAPTER 2

DATA ANALYSIS OF ELECTROMAGNETIC INTERFERENCE ON AIRCRAFT

After a brief introduction to the functionality of the common PEDs as well as the rules and regulations placed by agencies on airlines and PED manufacturers, it is important to understand the relationship between the PEDs relative to the aircraft radio systems that may possibly be affected. As mentioned in the previous chapter, the use of PEDs is often prohibited onboard aircraft due to their electromagnetic emissions, which may interfere with the avionics systems, most commonly radio navigation and communications. The next few sections provide a brief overview of the aircraft structure and the currently known reasons on why it becomes vulnerable to PED-related emissions

2.1 Reasons for Vulnerability of Aircraft systems due to PED-related Emissions

The problem of PED interference increases due to the aluminum air-frame of the aircraft, which can act as a shield, a resonant cavity, or a phased array. The radiation from the PEDs can couple to the avionics through the antennas, the wiring, or directly into the receiver of the aircraft [44]. Statistical reports presented in the Introduction chapter show that the navigation systems are the most vulnerable to PED-related emissions from within the aircraft's fuselage.

The navigation systems are vulnerable for two reasons: they have parts devised to detect and act on signals coming from the 'outside' and they are radio-based systems, which are particularly susceptible to low levels of interference. Since the aircraft control systems are located entirely within the aircraft, they are shielded from absolutely any signals not coming from one of their own devices. The control systems are also not radio-based, but are based entirely on electrical signals conducted through wires, similar to most computer networks. Navigation avionics, on the other hand, must have some designed sensitivity to environmental radio signals in order to perform their function [33].

According to Bruce Nordwall, the antennas of radio-based avionics may be affected by electromagnetic field intensities of as small as a microvolt per meter. But being outside the aircraft, the antennas get some protective attenuation from the fuselage of radiation originating inside the aircraft. Non-radio signals generally have higher signal

levels, and so are less susceptible to low interference levels [33]. According to Dave Walen, manager of electromagnetic effects for Boeing Commercial Airplane Group, “these are the instruments that we cannot harden because they are built to receive very small signals. We rely on those sensitive receivers to pick up small signals in space and that is the primary concern we have with carry-on electronic devices.” [44]

The hull of the metal aircraft forms an effective electromagnetic boundary between the outside and the inside of an aircraft. Electromagnetic signals find it hard to get in, or to get out. That is why the navigation and the radio antennae on the aircraft need to be placed outside the aircraft hull. But while outside, they must be sensitive. The navigation electronics inside the hull can be in principle just as well and securely shielded as control avionics, because there is no need at all for navigation systems to be sensitive to the electromagnetic signals coming from the inside of the aircraft. However, there are many reasons for these systems to be insensitive because there are many other electronics working in the same area as well [33].

Once the antennas have picked up the signals, they run through coaxial cables to communications or navigation receivers generally located below the floor of the cockpit. The output of those receiver boxes then goes to cockpit indicators or to other computers in the plane, or both. Most navigation signals, for example, go to a cockpit indicator and also to the autopilot computers. The wires that connect the receivers to the indicators or computers are twisted, shielded pairs, or twisted, shielded triples, depending on whether the signal is digital or analogue.

Often the wires from the antennas to the receivers run along the fuselage inside the aircraft skin, passing less than a meter from a PED wielding passenger. The thin sheet non-conducting material that forms the inside of the passenger compartment, typically fibreglass, offers no shielding whatsoever between the PED and the wiring. Boeing's Walen confirmed to Spectrum that wires critical to the functioning of the aircraft are generally shielded. American Airlines' Degner believes that because the cables are so well shielded most of the interference from PEDs is due to radiation that the antennas pick up, and then transmit to the cockpit instruments or the navigation computers [44].

Shielding could be damaged during servicing or could degrade over time. Figure 2 shows a detailed view of a fuselage during maintenance. The effectiveness of shielding

also depends upon good grounding. This is difficult to maintain over time because of the nature of aluminum's surface chemistry: aluminum oxidizes rapidly in air, thereby increasing the resistance of the electrical connection to ground. In that case, the wires could pick up interfering signals directly. Even with shielding in mint condition, electromagnetic interference can still couple to the aircraft's navigation or communication systems. Although the aluminum skin of the aircraft forms an excellent electromagnetic shield, it has holes through which the radiation can escape. In airliners, the greatest leakage of signals is through the windows as well as the doors [44].

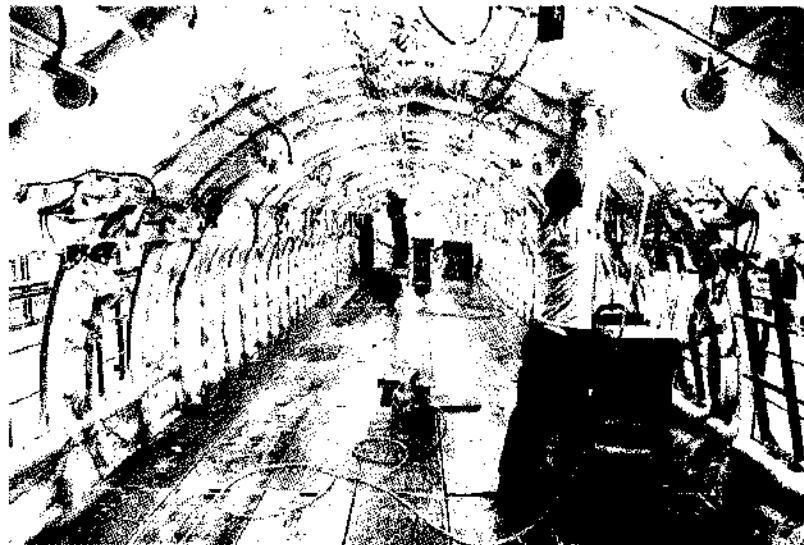


Figure 2. Interior View of an Aircraft Fuselage During Maintenance [44].

2.2 Introduction to Aircraft Schematics and Details

For this research, testing was performed on out-of-service, United - Boeing 737 (B737) and Boeing 757 (B757) series as well as Delta – Airbus 319 (A319) and Airbus 320 (A320) series. As a standard, the left half of all aircraft, when facing the cockpit of the plane, is referred to as the “port” side of the aircraft as usually the left side is used by passengers for boarding and leaving the plane. The right side of the aircraft is referred to as the starboard side, which is usually not used by passengers for boarding purposes.

The B737-200 aircraft has four exit doors. Two of the doors are located in the front side of the aircraft, referred to as L1 and R1 in this paper. The other two doors are located in the rear of the aircraft near the tail, referred to as L2 and R2. L1 and L2 are located on the port side, while R1 and R2 are located on the starboard side. There are also two emergency exits located near the wings of the aircraft; these are referred as LE

and RE for exits on port and starboard side, respectively. The emergency exits are located at window #16 of both port and starboard side of the aircraft on a standard B737.

Figure 3 [45] shows the locations of all the exit doors as well as emergency exits on a B737. Also shown in this figure are the port side exits 1, 3 and 5 and the starboard side exits 2, 4 and 6. The B737 aircraft has 32 windows on each side of the aircraft, including the window for the emergency exit. As explained in Chapter 2, the greatest emissions from PEDs is thought to leak out toward the aircraft systems through the doors and windows of the aircraft; therefore, it is necessary to know the exact locations of the doors and windows to analyze the electromagnetic patterns thoroughly.

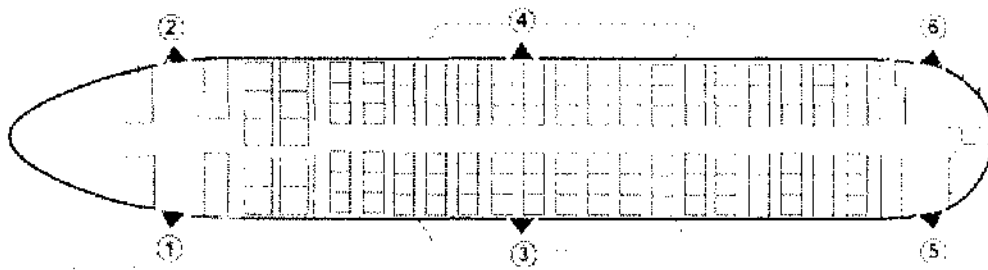


Figure 3. Interior Schematic of B737 [45].

Figure 4, Figure 5 and Figure 6 show the exit configurations for B757, A319 and A320, respectively [45].

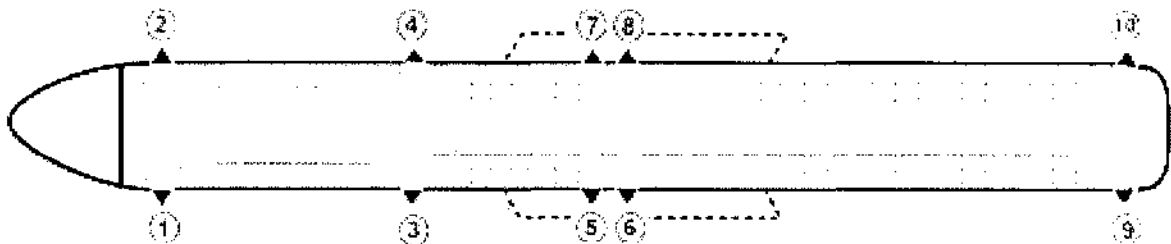


Figure 4. Interior Schematic of B757 [45].

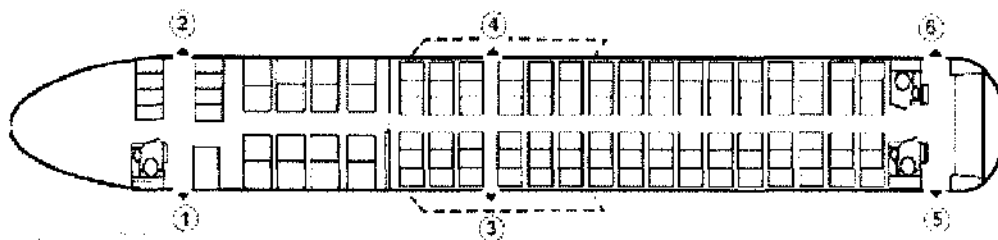


Figure 5. Interior Schematic of A319 [45].

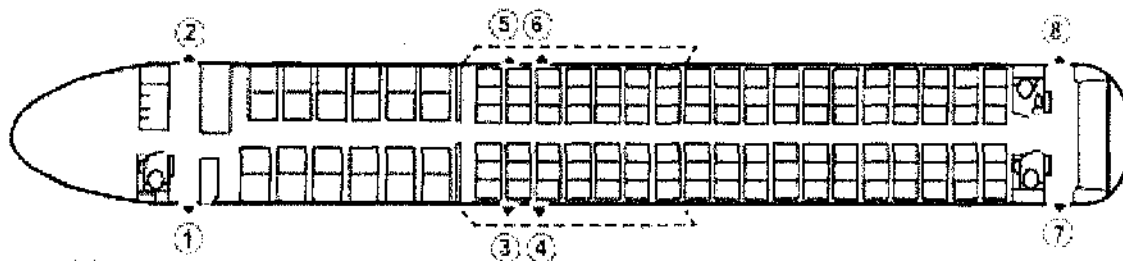


Figure 6. Interior Schematic of A320 [45].

For measuring IPL data, the aircraft systems considered included the systems mentioned in Table 2 along with their operating frequencies. Figure 7 shows the approximate locations and detailed antenna shapes of GS, TCAS, VHF and the LOC, while the possible locations of GPS are pointed out in Figure 8 for B737 systems.

Table 2. Aircraft Systems of Concern with Operating Frequencies.

Aircraft System	Operating Frequency (MHz)
MB	75
LOC-L	108.1 – 111.95
VOR	108 – 117.95
VHF-L	118 – 137
VHF-R	118 – 137
VHF-C	118 – 137
GS	328.6 – 335.4
DME-L	962 – 1213
DME-R	962 – 1213
ATC-T/U	1030
ATC-B/L	1030
TCAS-U	1090
TCAS-L	1090
GPS	1575±2

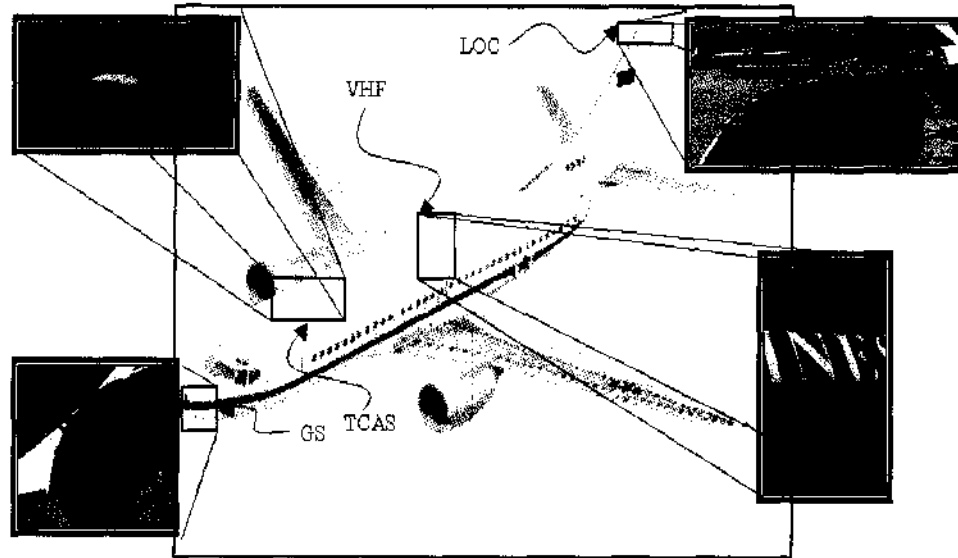


Figure 7. Antenna Locations on B737 (3-D).

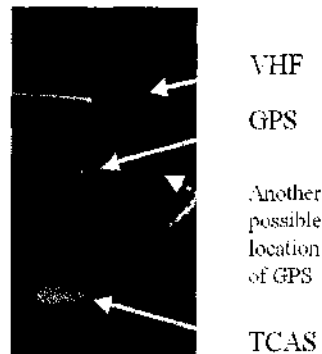


Figure 8. Possible Antenna Locations for GPS on B737.

As shown in Figure 7, GS is located in the nose of the aircraft; the TCAS is located directly on top of the second window of the aircraft, on the center of the fuselage. Figure 8 shows two possible locations of the GPS system, behind the TCAS approximately on top of window #9. As shown in the figure, unlike TCAS, the GPS antenna is not installed along the top centerline of the aircraft, but instead, is slightly offset to the starboard side of the airplane. VHF is located behind the GPS antenna on top of the emergency exit, or window 16. Finally, the LOC system is installed on the tip of the tail of the aircraft. In some aircraft, the LOC is installed in the nose of the aircraft, along with the GS antenna; however, in B737, the system is installed in the tail. Figure 9, Figure 10, Figure 11 and Figure 12 show the antenna configurations, along with exit locations, for B737 (repeat), B757, A319 and A320, respectively.

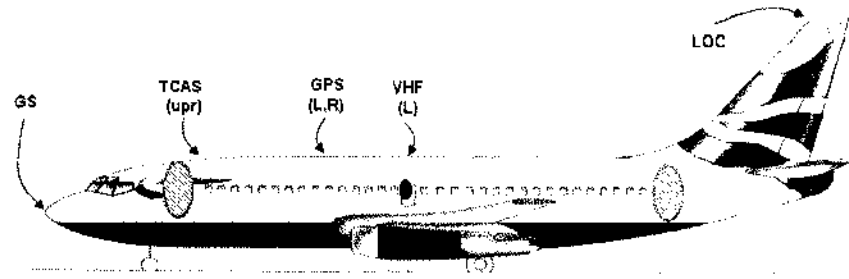


Figure 9. Antenna Locations of B737.

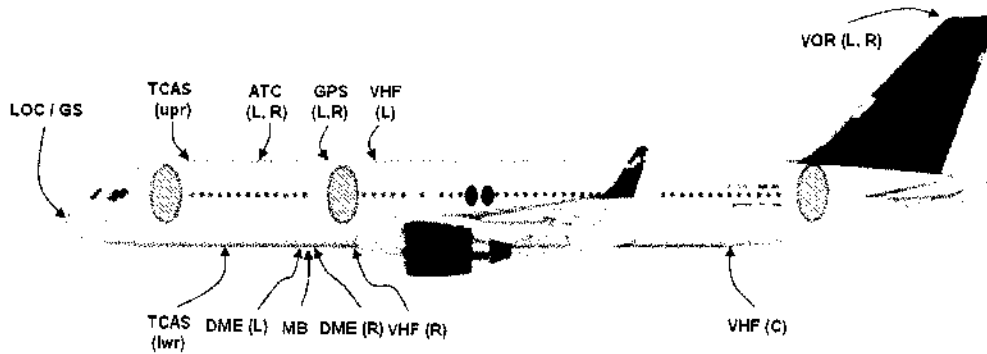


Figure 10. Antenna Locations on B757.

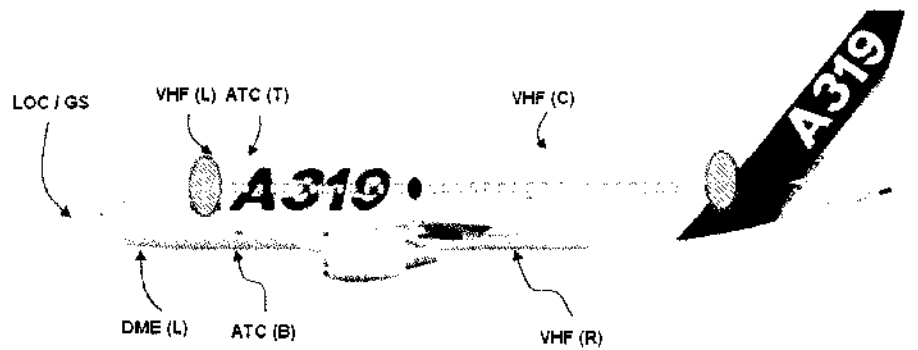


Figure 11. Antenna Locations for A319.

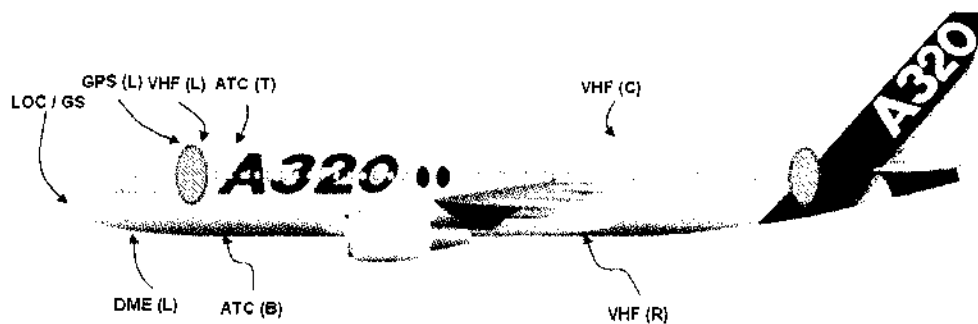


Figure 12. Antenna Locations for A320.

2.3 Aircraft Systems of Concern

Table 3 provides a list of avionics systems that are of concern in the event of interference along with their operational frequencies. Out of the possible aircraft systems mentioned in Table 3, most at risk are those that have antennas located at various points outside the skin of the aircraft to pick up the navigation and communication signals. The highlighted systems will be studied in the research. In general, manufacturers of the systems listed in the table are responsible for designing immunity into their products. According to Bennett Kobb, editor of Spectrum Guide, “there can be substantial differences in the level of interference immunity between what is technically possible, what is cost effective, and what is reasonable for policy makers to expect from manufacturers.”[44]

In terms of functionality of the major systems, OMEGA navigation, at the low end of the frequency spectrum, is used to determine aircraft position through ground-based transmitters. VOR, or the VHF omnidirectional range finder, is a radio beacon that is used to navigate from point to point. The Glide slope system is used during landings. Above 1 GHz is the DME (distance-measuring equipment), which gauges the space between the aircraft and a ground-based transponder and is used throughout the flight, from take-off to landing. Also in the spectrum above 1 GHz are TCAS (Traffic Alert Collision Avoidance System), GPS (Global Positioning System), and cockpit weather radar systems [44].

Among the systems listed above, all avionics systems are susceptible to interference from high levels of electromagnetic radiation. Some systems, however, are more susceptible than others. As mentioned in previous section, for addressing susceptibility, avionics systems can be divided into two broad classifications, radio-based and non-radio. The radio-based systems have an antenna where on-channel field intensities of only microvolts per meter can be a serious interference threat. Non-radio systems do have signals traveling between their components' parts. The signal levels are, however, significantly greater than those received by the radio-based systems and the susceptibility to low levels of interference is significantly reduced. On the other hand, the radio systems antennas are mounted outside of the aircraft and their susceptibility to interference from radiating devices inside the aircraft benefits from the attenuation of the

aircraft fuselage. Interconnecting wires that may serve as ingress points for non-radio systems are inside the fuselage and can be very close to PED radiators and receive much higher field intensity.

Table 3. Aircraft Systems of Concern in the Event of Interference [34].

More Susceptible		Less Susceptible
Glide Slope (329 – 335 MHz)	LORAN-C (100 kHz)	ADF (190 – 2000 kHz)
Localizer (108 – 112 MHz)	MODE-S (1030 MHz)	Autopilot (non-radio)
TCAS (1030, 1090 MHz)	MLS (5031 – 5091 MHz)	EFIS (non-radio)
VOR (108 – 118 MHz)	SATCOM (1) (1545-1555 MHz)	Flux Gate Compass (non-radio)
GPS (1575 MHz)	SATCOM (2) (1610 – 1626.5 MHz)	Low-Freq. Wx Map (50 kHz)
VHF COMM (118 – 137 MHz)	SATCOM (3) (1645.5 – 1655.5 MHz)	NAV Computers (non-radio)
DME, (TACAN) (978-1215 MHz)	Marker Beacon (75 MHz)	Radio Altimeter (GPX) (4.3 GHz)
ATCRBS XPDR (1030 MHz)		Weather Radar (9.375 GHz)
OMEGA (10 – 14 kHz)		HF (2 MHz – 30 MHz)

2.4 Coupling Phenomenon to Aircraft Systems

The common PEDs operate at frequencies from a few tens of kilohertz for AM radios to greater than 3 Gigahertz for laptop computers. When the harmonics of these signals are taken into account, the emitted frequencies cover nearly the entire range of navigation and communication frequencies used on the aircraft. The frequency and intensity of the radiation also depend on the mode in which the device is being operated. Also, different types of avionics have different sensitivities, making the likelihood of interference very random and unpredictable. A radiation source may cause total destruction of a navigation signal on one channel while nearby channels are completely unaffected. Another type of signal may be sensitive to the modulation of the signal or to the number of individual radiators [44]. Experimentation by Devereux, et. al., showed effective vulnerability of major navigation systems (VOR, VHF, Glide slope and GPS) due to low powered RF sources located in passenger cabin, baggage compartments, avionics and cargo bay areas .

Interestingly, the technology of cellular phones poses a threat to the phone technology on ground level, as it is based on the small local ground based receptions called cells. Cell phone networks are such that a cell phone user is served by just one cell, and when reaching the boundary of that cell, the signal gets 'handed over' to the next cell which the user is about to enter. The topology of the coverage is based on the assumption that the user is on or near ground, and it is a technical assumption on which the entire system is based that a user will be within 'sight' of just one cell, except when nearing a cell boundary. When in an aircraft, however, the user is within radio 'sight' of many cells, simply because of the very high altitude. An attempted call or reception from an aircraft would activate many, if not all cells, in the local area, which 'breaks' the technology. It causes many transmission problems, and the network system is disturbed [33].

2.5 Graphical Representation of Collected IPL Data

IPL data was collected on B737, B757, A319 and A320. Please refer to Appendix A: IPL Measurement Overview, for measurement methodology and other details. This section includes detailed plots of the collected IPL data on the four aircraft type. Each plot includes IPL data collected on a particular aircraft (i.e. B737, B757, A319 or A320), for a selected aircraft system of concern (i.e. GS, VHF, TCAS etc.). Multiple trials of IPL data was collected for every system on each aircraft type. For instance, IPL data for GS was collected on six different B737s. These different airplane numbers can be identified using the aircraft nose number (i.e. 1989, 1883, 1879, 1991, 1907, and 1994 for B737). These nose numbers are systematically assigned by the airline manufacturer and do not correspond to the year of manufacturing, or age of aircraft. Furthermore, these nose numbers vary from being 3 to 4 digits among the four aircraft types. In each of the plots below, the IPL data is represented in "pathloss" (dB). The unit of pathloss is inversely proportional to the amount of coupling. Therefore, in the regions on low pathloss, high coupling exists between the transmit antenna location (simulated PED) and the aircraft system of concern (GS, GPS etc). Thus, the study is concerned more with areas of low pathloss, or high coupling.

Raw IPL values for all systems on all four aircraft (B737, B757, A319 and A320) are included in Appendix D. The raw values need to be calibrated using the calibration

factors, also reported in Appendix D, by adding the total calibration factor (row 7 in the “Correction Factors” section) to each of the raw measurement for the corresponding column. The appendix includes measurements for both horizontal and vertical polarization for each system; however, only the dominant polarizations will be discussed in the following sections.

Figure 13 shows calibrated IPL data measured on B-737 for GS. GS is a horizontally polarized system; therefore, only the horizontal polarization is plotted. Recall that during IPL measurement, data was measured for both horizontal and vertical polarization for each system, however, it has been verified that the lowest regions of pathloss are found in the dominant polarization measurements for the particular system of concern [42]. In the plot, the x-axis represents the window locations inside the aircraft (from window 1 to window 33, in this case). The y-axis represents the pathloss value in dB. GS is located in the nose of B737. Interestingly, it can be noticed that the pathloss values in the front of the aircraft are lowest, and increase as the distance from the antenna increases. Also, it is important to note that there exists a pathloss deviation of about 7 dB among the 7 trials plotted. The similar sloping trend in the deviation among trials shows that although the IPL data is repeatable, there exist room for error in measurement due to change in equipment, aircraft nose number, or even change in testing personnel.

Figure 14 shows IPL patterns for the vertical polarization of TCAS on B737. TCAS is located on top of window 2 of the aircraft. Similar to GS, it can be observed that the pathloss is lower in the front of the aircraft (near window 2) and increases toward the rear of the aircraft. The IPL patterns in repeatable through various trials; however, a deviation of about 5 dB exists among the trials.

Figure 15 shows the IPL pattern for various trials on the VHF system for B737. VHF is a vertically polarized system. A noticeable trend of decreasing pathloss pattern exists near the location of antenna (window 16). The pathloss is the lowest near window 16 and increases as the distance from antenna location increases. However, there exists a very large deviation among the various trials (as large as 25 dB!). Due to the large deviation, the results for VHF may not be considered for modeling purposes.

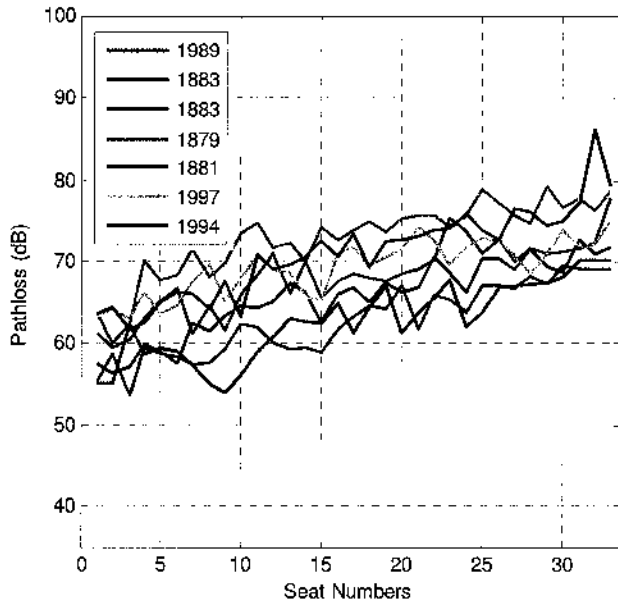


Figure 13. IPL Data for GS-L in Horizontal Polarization (B737).

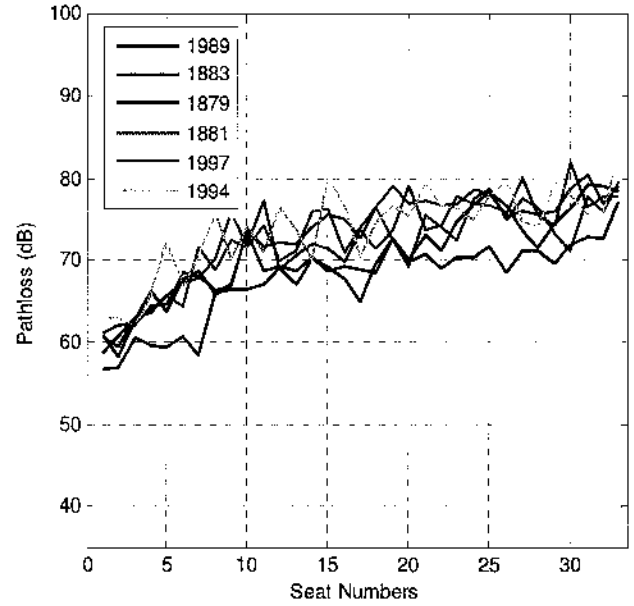


Figure 14. IPL Data for TCAS-U in Vertical Polarization (B737).

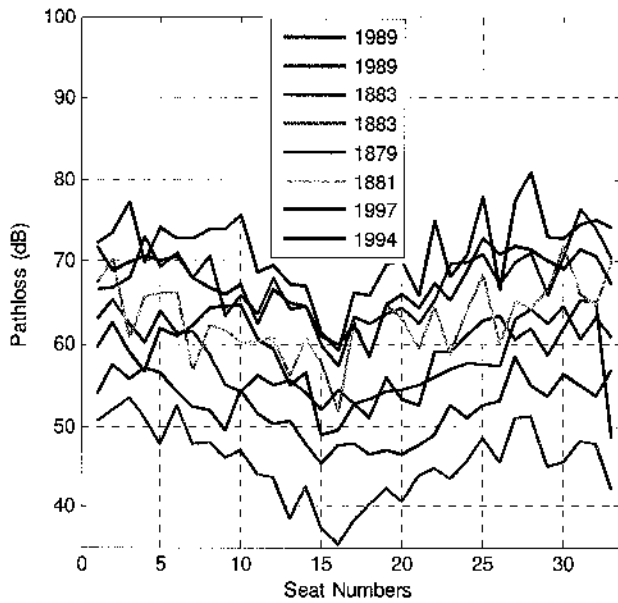


Figure 15. IPL Data for VHF-L in Vertical Polarization (B737).

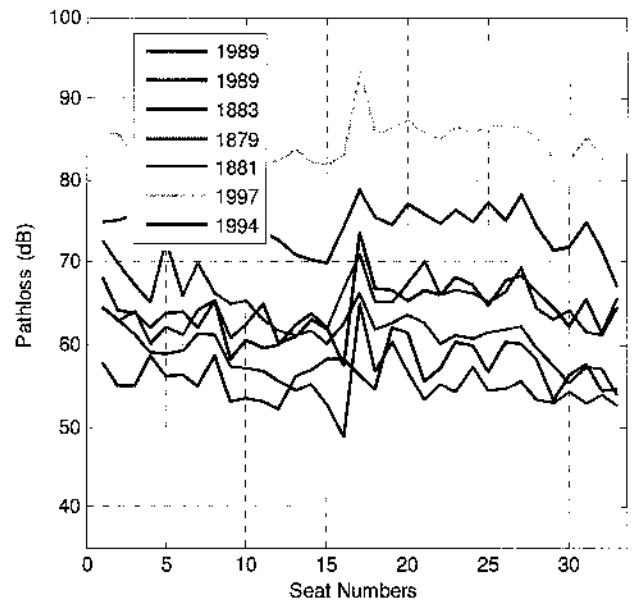


Figure 16. IPL Data for LOC-L in Horizontal Polarization (B737).

Figure 16 shows IPL patterns for LOC on B737. LOC is a horizontally polarized system as is mounted on the tail of B737. Unlike previous systems, where the lowest pathloss occurred closest to the location of the system antenna, the lowest pathloss for LOC actually exists near window 16, or the emergency exit of B737. This phenomenon can be explained by the fact that LOC is a horizontally polarized system, whereas, the

closest exit to LOC is located almost vertically from the tail; therefore, causing no coupling. Furthermore, it can be observed that the lowest pathloss in fact occurs to the closest, most leaky, entrance into the aircraft (in horizontal direction), which turns out to be the emergency exit (or window 16). As the distance from the antenna increases toward the front of the aircraft, the pathloss value also increases. Although a similar trend is observed among all trials, two trials (1997 and 1994) deviate significantly from the remaining trials. These two trials will not be considered in modeling due to their deviation.

Figure 17 shows IPL patterns for GS on B757. Compared to B737, B757 is a much longer aircraft. Therefore, it can be observed, that unlike the GS results for B737, B757's GS shows lesser deviation from front to rear of the aircraft. Although, similar to the IPL results from GS on B737, the results here again show the lowest pathloss values in the front of the aircraft, closest to the location of GS. Furthermore, it can be observed that there exists very minor deviation in the front IPL values, however, the deviation among the three trials increases to about 10 dB in the rear of the aircraft. This IPL plot also provides a good example to observe difference between a 3-digit and 4-digit nose numbers (6706 vs. 690 as an example). B757 #690 was a slightly smaller aircraft, with two lesser windows than B757 #6706 and B757 #6707. To account for this difference, the IPL value in the last window of B757 #690 has been duplicated thrice to attain equal number of windows. This method of duplication will be repeated for all aircraft of similar types, but different nose numbers in order to attain equal number of windows for each trial of every system.

IPL data for B757's LOC is plotted in Figure 18. Similar to the results in B737, there exist large deviation among the three trials of B757 data (about 12 dB). However, this deviation is not significant enough and therefore, this data will be considered for modeling purposes. Unlike B737, LOC for B757 is located in the nose of the aircraft, alongside GS. However, unlike the coupling patterns for B757's GS, the pathloss values for LOC are the lowest near the emergency exits of B757, located on windows 21 and 22. This shows that the emergency exits are more leaky than the main exits of B757.

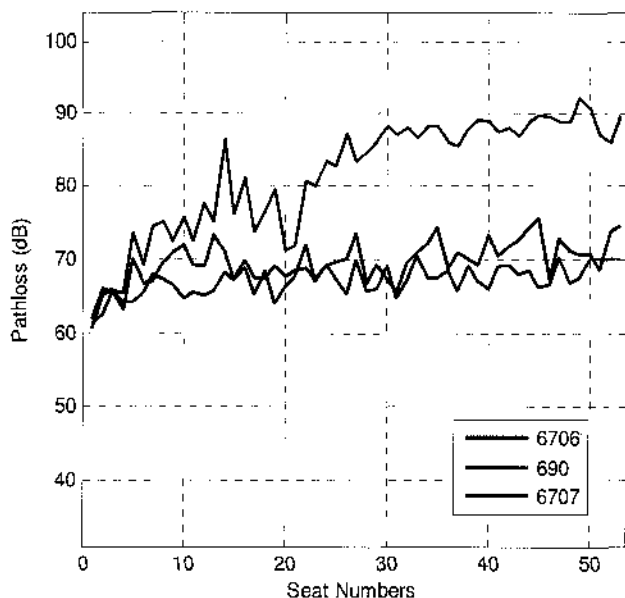


Figure 17. IPL Data for GS-L in Horizontal Polarization (B757).

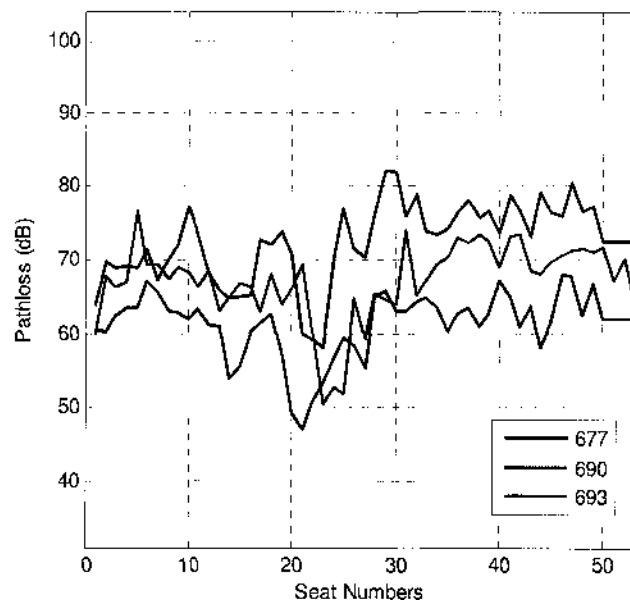


Figure 18. IPL Data for LOC-L in Horizontal Polarization (B757).

Figure 19 shows the results for B757's TCAS, located on top of window 2 of the aircraft. Similar to the TCAS results for B737, the two trials show the lowest pathloss near the front of the aircraft in vertical polarization, increasing as approaching the rear. Again, the increasing trend in B757 is not as prominent as the trend observed in B737, which has a shorter fuselage.

Figure 20 shows only one trial of the IPL data measured on the lower TCAS for B757. This second TCAS is located approximately below the 5th window of the aircraft and is also vertically polarized. The lowest pathloss exists near the front exit of the aircraft, increasing as approaching the rear windows. It is also observed that the pathloss decreases again when approaching the second exit (near window 15), increases again to follow the overall trend. This phenomenon again emphasizes the leakiness of the main aircraft exits.

Figure 21 and Figure 22 shows the IPL patterns for ATC-U and ATC-L systems, respectively, on B757. ATC-L is a vertically polarized system and is located approximated on top of the 8th window in B757. The lowest pathloss in the three trials indeed occurs closest to window 8 and increases elsewhere as the distance from the window to system increases. A large deviation is observed between the trials for B757 #690 and B757 #6707. The two measurements for B757 #690 correspond to the

individual IPL measurements taken at the port and starboard side of the aircraft. Similar to GPS, ATC-L is installed slightly off-centered from the centerline of the fuselage. To be exact, ATC-L is installed slightly on the port side of the centerline, while ATC-R is installed on the starboard side.

The IPL patterns for DME-L for B757 are included in Figure 23. DME-L is a vertically polarized system and is located under window 13 of the aircraft. The results from DME vary slightly between trials and show very little trend in pathloss value due to the location of the system. Figure 24 includes IPL patterns for MB on B757. MB is a horizontally polarized system and is located underneath window 14 of the aircraft. Unlike other systems, there is much variation in IPL values from window to window in MB. Also, there exists a trend of low pathloss values in the beginning of the aircraft (near the installed system), to increasing values in the aft of the aircraft. Due to the polarization effect, the increasing trend occurs more slowly in MB than observed in vertically polarized systems.

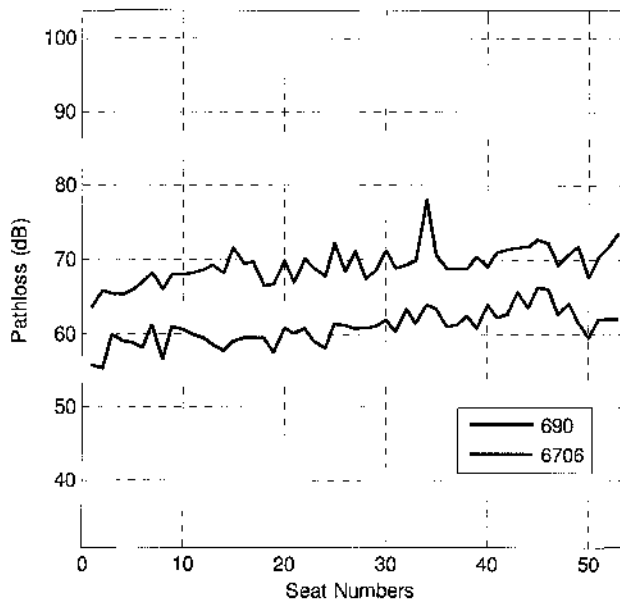


Figure 19. IPL Data for TCAS-U in Vertical Polarization (B757).

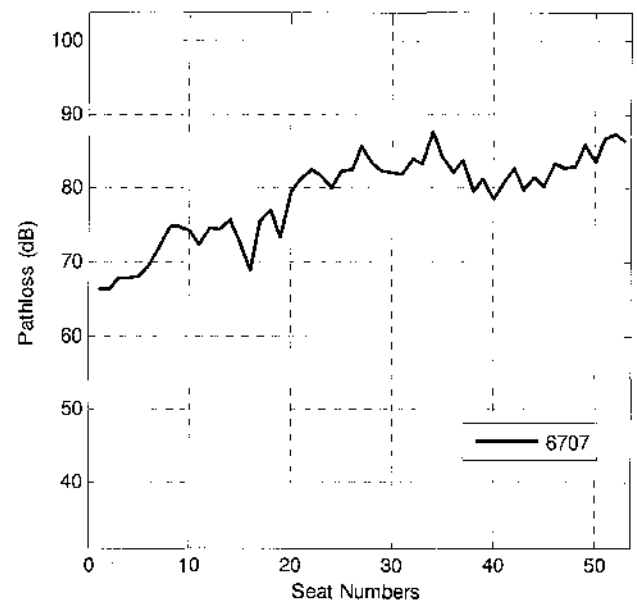


Figure 20. IPL Data for TCAS-L in Vertical Polarization (B757).

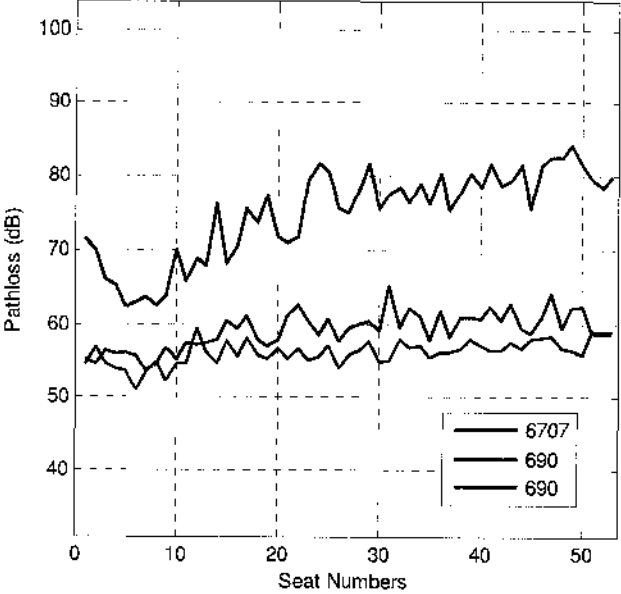


Figure 21. IPL Data for ATC-U in Vertical Polarization (B757).

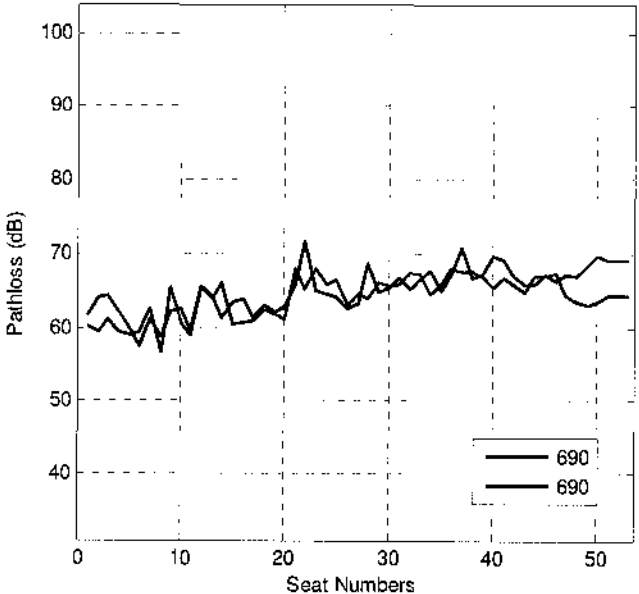


Figure 22. IPL Data for ATC-L in Vertical Polarization (B757).

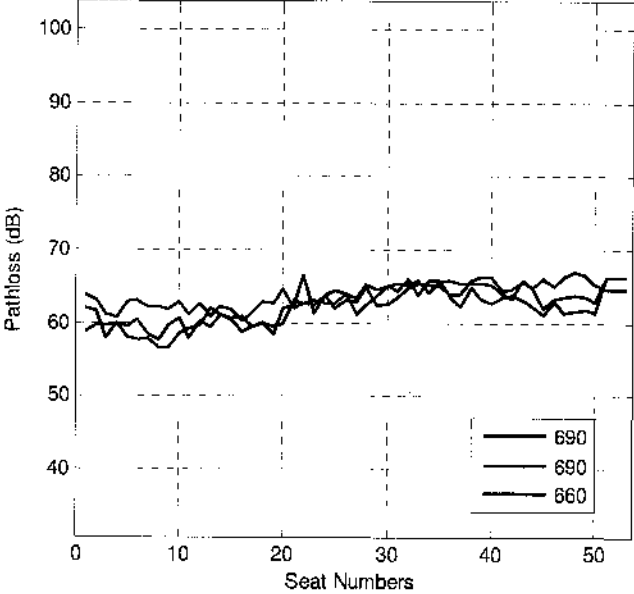


Figure 23. IPL Data for DME-L in Vertical Polarization (B757).

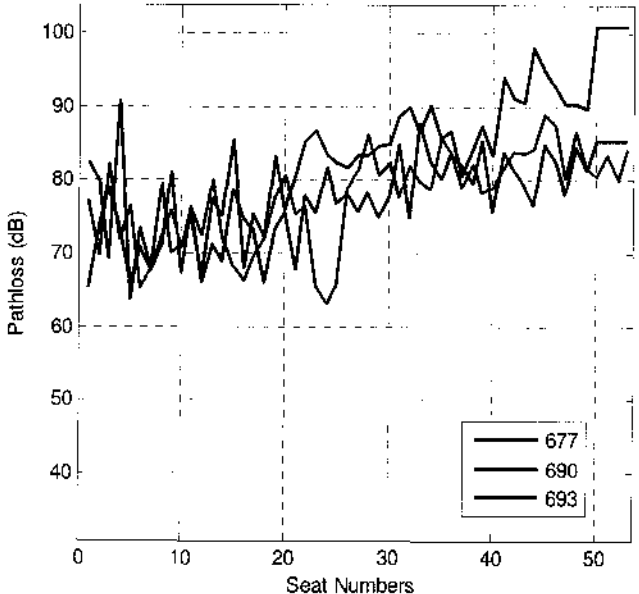


Figure 24. IPL Data for MB in Horizontal Polarization (B757).

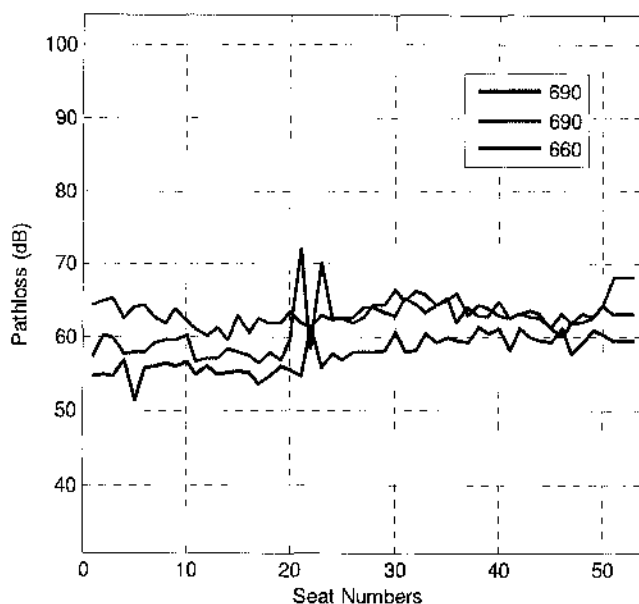


Figure 25. IPL Data for DME-R in Vertical Polarization (B757).

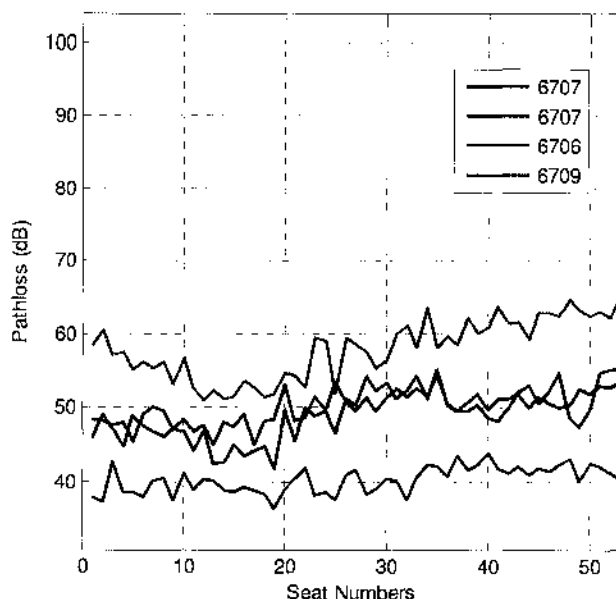


Figure 26. IPL Data for GPS-L in Vertical Polarization (B757).

Figure 25 shows the IPL patterns for DME-R on B757. DME-R is also a vertically polarized system and is approximately installed beneath window 15 of the aircraft. Similar to the results for DME-L on B757, there are no trends observed in the IPL pattern. Also, the deviation among the three trials is very insignificant.

The IPL patterns for GPS-L on B757 are presented in Figure 26 and Figure 27. Unlike all other systems, GPS is a circularly polarized system, increasing the likelihood of coupling with both horizontal and vertical emissions. Therefore, Figure 26 includes IPL pattern for measurements taken in the dual-ridge horn being in vertical position, while the dual-ridge horn is in horizontal polarization in the IPL pattern presented in Figure 27. GPS-L is located slightly on top of window 15 of the aircraft. Very little trend of low to high pathloss can be observed in vertical polarization plot, where the pathloss increases slightly as the distance from antenna increases. However, no such trend is observed in the graph for horizontally held dual-ridge horn. Furthermore, there exists must deviation, about 20 dB, in both vertical and horizontal representation of pathloss fo GPS-L. Due to these deviations, GPS will not be considered for modeling purposes.

Figure 28 shows the IPL patterns for VHF-R on B757, approximately located under window 16 of the aircraft. There exist slight trend in the IPL patterns for the three

trials. There also exists large deviation of about 10 dB after window 16 of the aircraft. Although VHF-R is located very close to exit 2 of the aircraft, unlike the VHF results in B737, very minor trend of decreased pathloss can be observed near the second exit (windows 14-16). These results can also suggest that the systems installed at the bottom of the fuselage do not couple as greatly as the systems installed on the top of the fuselage.

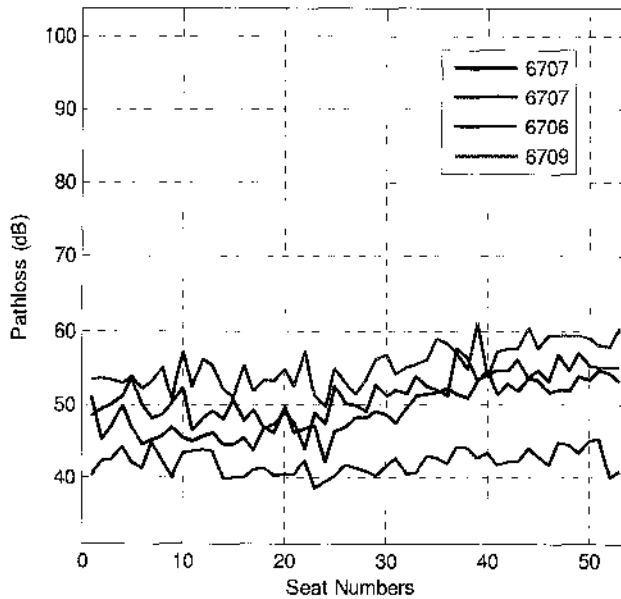


Figure 27. IPL Data for GPS-L in Horizontal Polarization (B757).

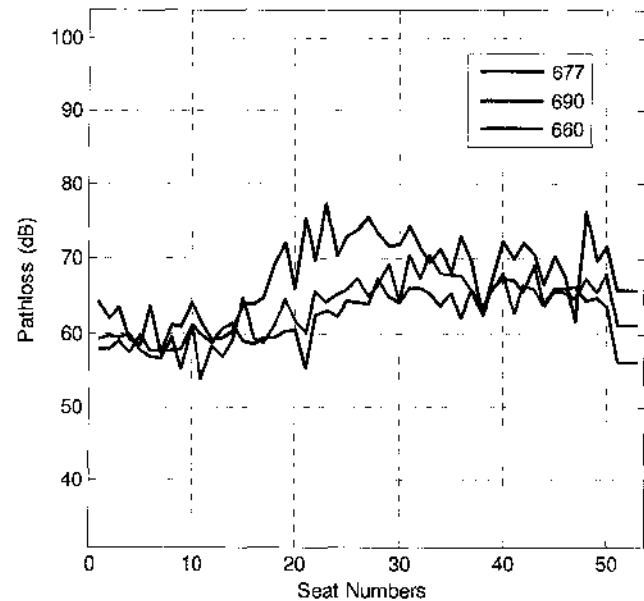


Figure 28. IPL Data for VHF-R in Vertical Polarization (B757).

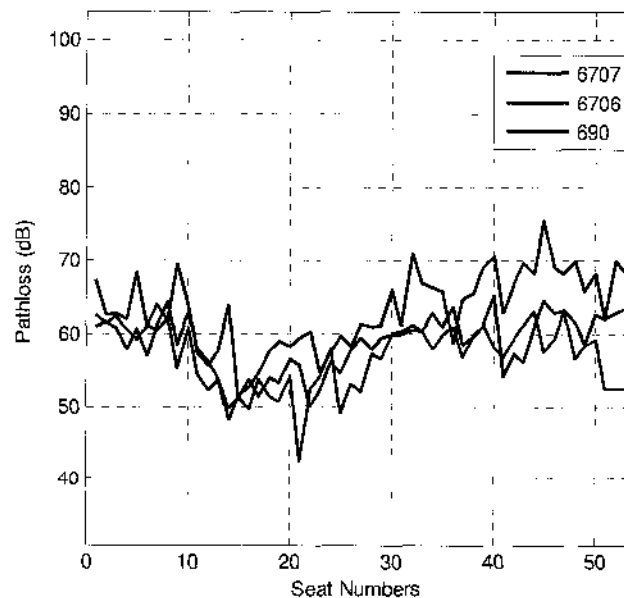


Figure 29. IPL Data for VHF-L in Vertical Polarization (B757).

The IPL patterns for VHF-L in B757 are summarized in Figure 29. VHF-L is located approximately on top of window 19 on the fuselage. Similar to the VHF pattern in B737, a decreased level of pathloss is observed near windows 18 through 22, while the levels of pathloss increase as the distance from antenna increases. There also exists insignificant deviation among the three trials reported.

Figure 30 includes IPL patterns for B757's VHF-C, which is approximately located beneath window 45 of the aircraft. Similar to other VHF systems, VHF-C is also vertically polarized. The lowest levels of coupling are observed near the rear exit of the aircraft. The trend of low to high pathloss occurs from the aft of the aircraft going forward. Minor deviation among the three trials exist in the aft measurements, however, these deviations increased to about 15 dB around the front few window measurements.

Similar to B737's LOC, B757's VOR is located on the tip of the tail. The IPL measurements from VOR are recorded in Figure 31. VOR is also a horizontally polarized system. The lowest pathloss values are not observed at the aft windows, but are instead recorded near the emergency exits of the aircraft. There is minor deviation in IPL measurements among the three trials.

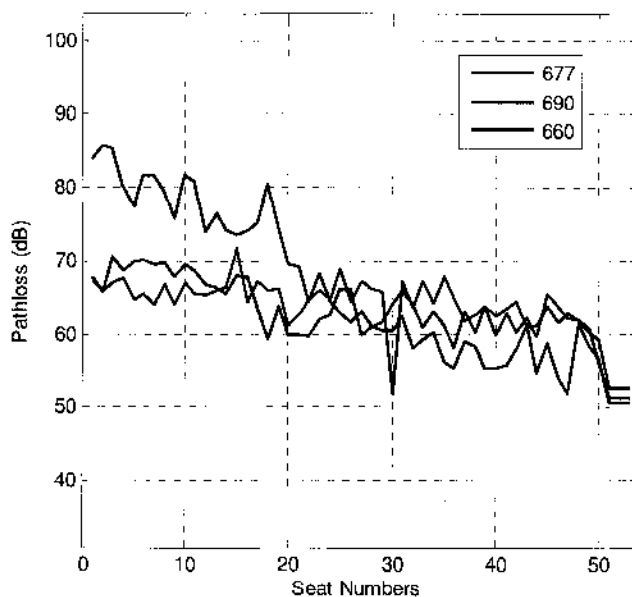


Figure 30. IPL Data for VHF-C in Vertical Polarization (B757).

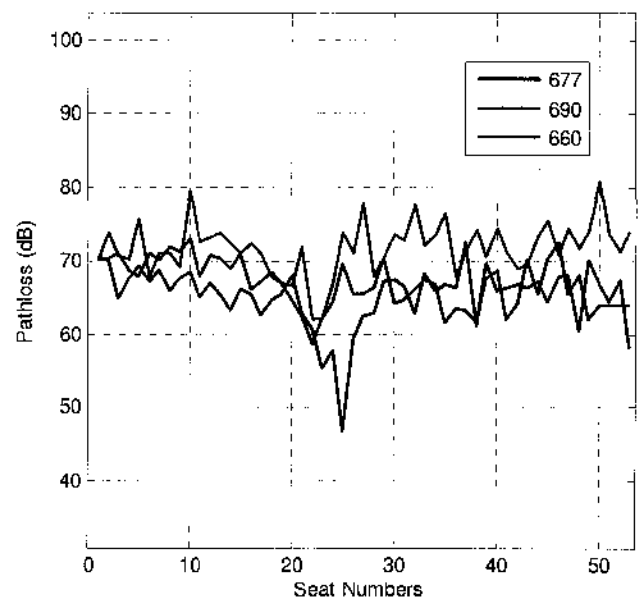


Figure 31. IPL Data for VOR-L in Horizontal Polarization (B757).

Figure 32 includes the IPL pattern for A319's GS-L. A319 is structurally very similar to B737; however, as observed, the patterns for GS-L for the two aircraft types are quite dissimilar. There exists a much lesser increasing pathloss trend from the front to aft of the aircraft. This may signify the fact that the exits on A319 are better shielded than the exits on B737; therefore, causing greater signal loss from transmission by simulated PED inside the aircraft to reception by aircraft antenna.

Figure 33 includes the IPL pattern for LOC-L on A319. As observed even the port and starboard repetitions vary by 5-10 dB; therefore decreasing the repeatability of these measurements. Furthermore, there is no significant trend observed as the IPL values deviate from one window to the next throughout the aircraft. Therefore, the IPL results from this system will not be considered in the modeling.

The IPL results for A319's DME-L are plotted in Figure 34. DME-L is located at the bottom centerline of the fuselage, approximately between the nose and the first exit of the aircraft. Although DME-L is a vertically polarized system, an increasing trend from low to high pathloss is observed from the first to the last window of A319. In previous systems, it was typical for vertically polarized systems to have a dominant effect of low pathloss close to the system, with a sharply increasing trend of higher pathloss as the distance increased. So although the trend of greater pathloss exists, as distance from antenna increase, the trend seems to increase much slower than observed in other systems. Perhaps, the position of the system at the bottom of the fuselage, instead of the top can account for the slowly increasing trend.

Figure 35 shows IPL pattern for VHF-L on A319. VHF-L is a vertically polarized system located on top of the first exit of the aircraft. Low pathloss is observed not only in the front, but also near the emergency exit (window 14) of the aircraft. Similar trend of low pathloss near emergency exit has been observed in B737 and B757 data for VHF systems.

The IPL patterns for A319's ATC-B are plotted in Figure 36. ATC-B is a vertically polarized system and is located at the bottom centerline of the fuselage, beneath window 2. Similar to A319's DME-L, ATC-L shows very slow increasing trend in pathloss from front to rear of the aircraft. Again, this smooth transition may be due to the antenna's placement at the bottom of the fuselage, instead of the top.

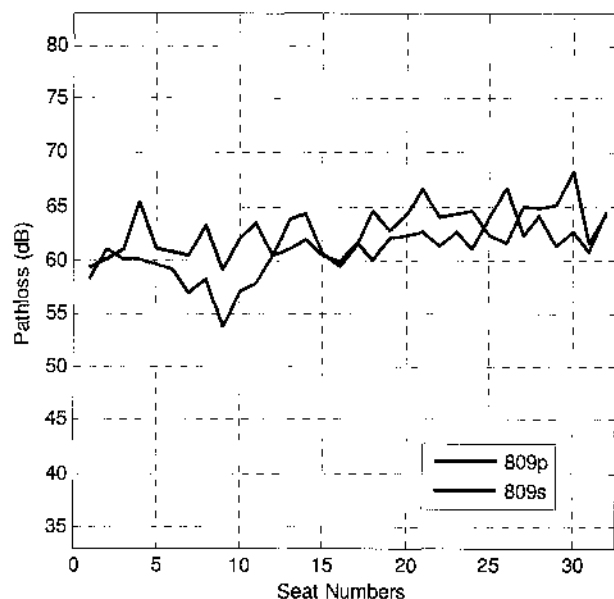


Figure 32. IPL Data for GS-L in Horizontal Polarization (A319).

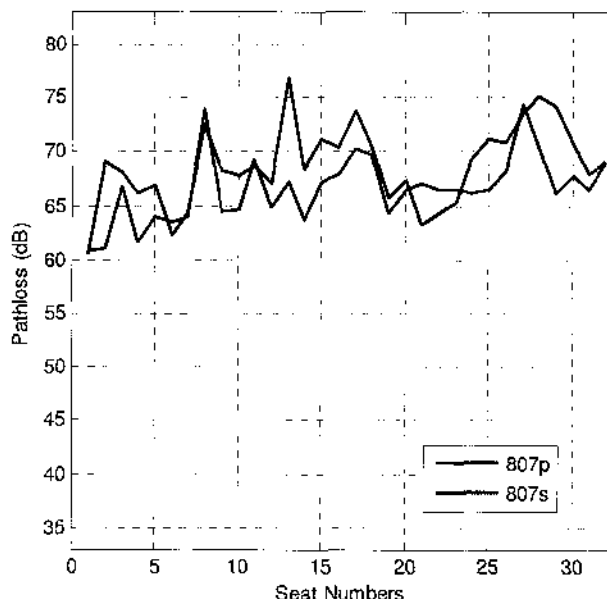


Figure 33. IPL Data for LOC-L in Horizontal Polarization (A319).

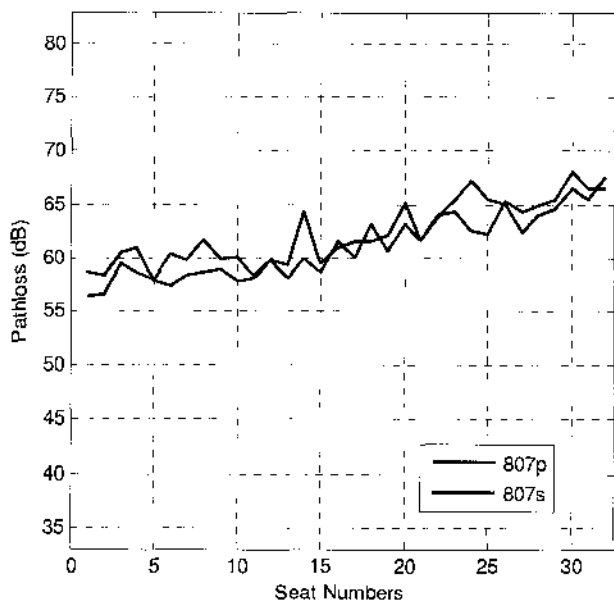


Figure 34. IPL Data for DME-L in Vertical Polarization (A319).

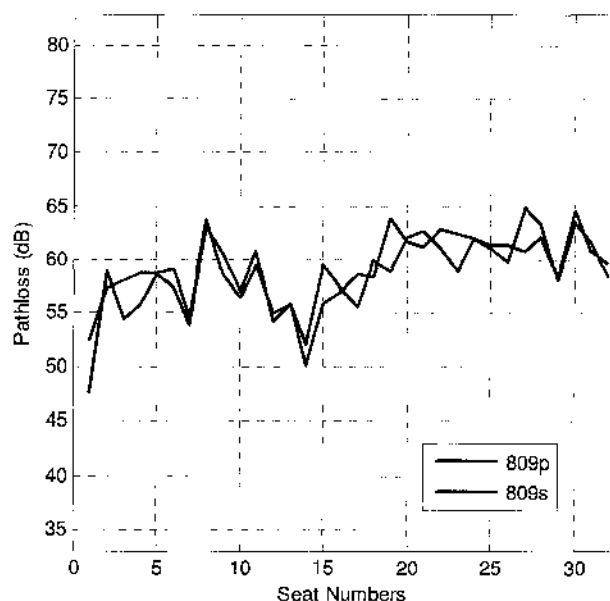


Figure 35. IPL Data for VHF-L in Vertical Polarization (A319).

The A319's ATC-T is located on top of the 3rd window of the aircraft. The IPL pattern for ATC-T is presented in Figure 37. There exists greater than 10 dB variation between measurements on the port versus starboard sides in the two trials. Furthermore, no trend of low to high pathloss can be observed. There is a slight increase in pathloss from the front to the rear of the aircraft in the IPL measurements taken on the starboard side.

Figure 38 includes IPL patterns for VHF-R on A319, located at the bottom centerline of the fuselage near window 21. As observed in the figure, the lowest pathloss indeed occurs near window 21, increasing as approaching the front of the aircraft. The trend also increases in pathloss values toward the rear of the aircraft; however, low pathloss is again encountered near the rear exit of the aircraft. The front exit of the aircraft also shows lower pathloss, or higher coupling values. There also exists very insignificant deviation among the two trials on VHF-R.

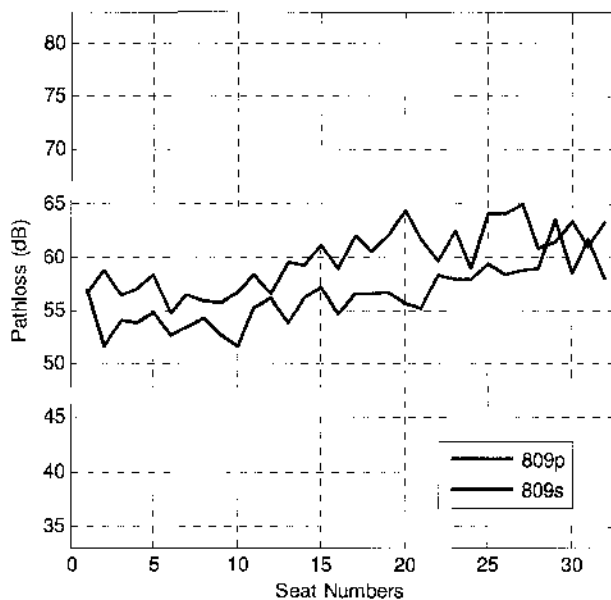


Figure 36. IPL Data for ATC-B in Vertical Polarization (A319).

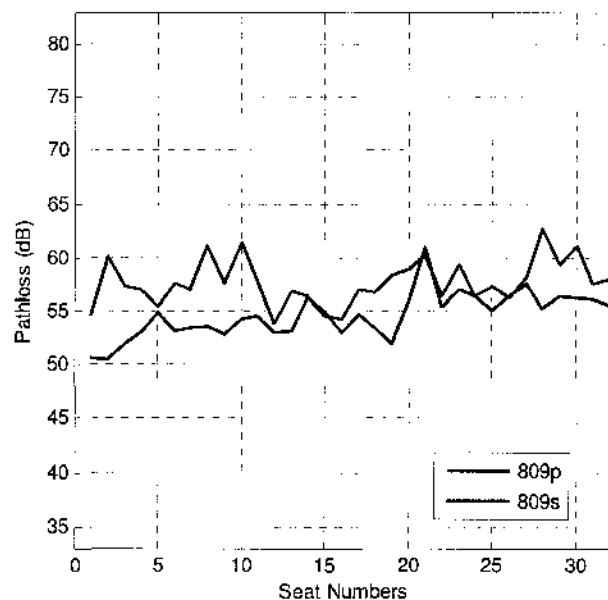


Figure 37. IPL Data for ATC-T in Vertical Polarization (A319).

Figure 39 includes IPL patterns for A319's VHF-C, located on top of the fuselage near window 24. Similar to VHF-R, low pathloss values are observed near window 24 and the trend of pathloss increases as the distance from the antenna increases. However, unlike VHF-R, there is a significant drop in pathloss observed near the emergency exit of the aircraft (window 14). This difference may be due to the existence of VHF-R at the bottom of the fuselage, while VHF-C exists at the top of the fuselage.

A320 is a larger aircraft than A319 with two emergency exits. Figure 40 shows the IPL pattern measured for GS-L on A320. Similar to B757, low pathloss values are observed near the front windows of the aircraft. Again, a trend of increasing pathloss values exists until the rear of the aircraft. Also, there is very minor deviation between the port and starboard measurements, proving the repeatability of the data.

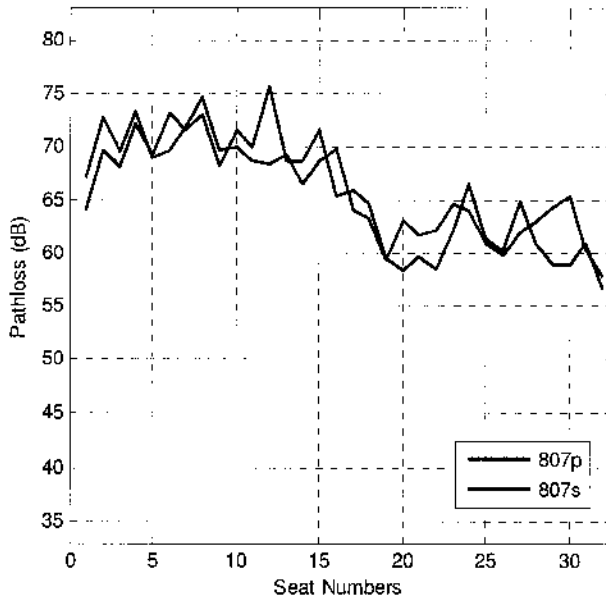


Figure 38. IPL Data for VHF-R in Vertical Polarization (A319).

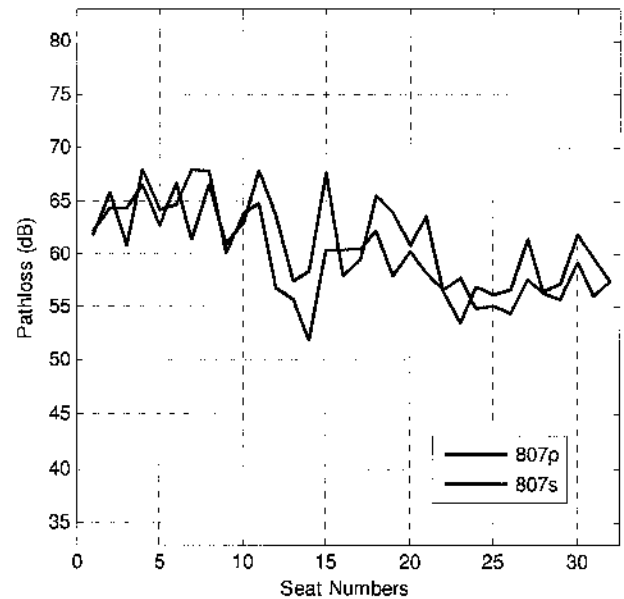


Figure 39. IPL Data for VHF-C in Vertical Polarization (A319).

The IPL pattern for A320's LOC is presented in Figure 41. Similar to GS, LOC is also installed in the nose of the aircraft and is horizontally polarized. As observed in A319's LOC pattern, there exists a slowly increasing pathloss pattern from the front to rear of the aircraft. Also, there is a drop in pathloss value near the emergency exit of the aircraft (windows 17 and 18). There is also a significant deviation of about 10 dB between the two trials near the emergency exits; however, this data will still be considered for the modeling due to very small deviation between the two trials throughout the remaining aircraft.

The IPL results for A320's DME-L are plotted in Figure 42. Similar to A319, A320's DME-L is located at the bottom centerline of the fuselage, approximately between the nose and the first exit of the aircraft. An increasing trend from low to high pathloss is observed from the first to the last window of A320. There is also very small deviation in pathloss data between the two trials.

A320's VHF-L is located on top of the first exit of the aircraft. Figure 43 shows the IPL pattern for VHF-L in A320. Similar to previous systems, VHF-L, due to being vertically polarized, shows lowest pathloss values near the first exit, and the trend of low to high pathloss appears as the distance from the antenna increases. Furthermore, there

exists a drop in pathloss near windows 16 through 19, which shows existence of greater coupling near the emergency exits.

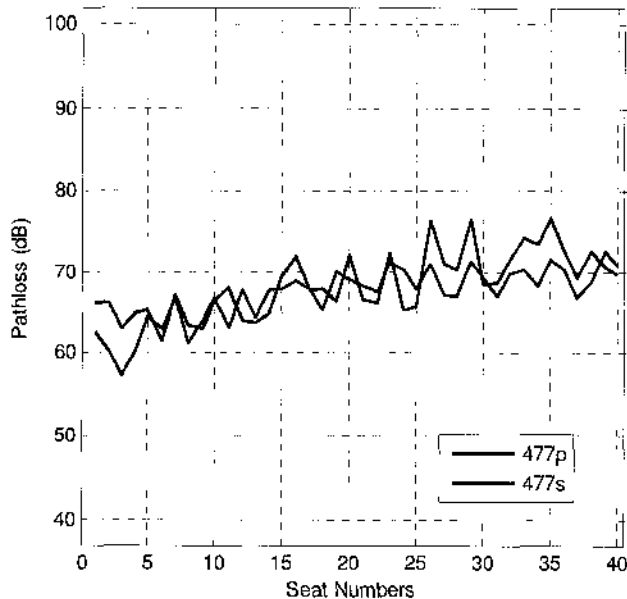


Figure 40. IPL Data for GS-L in Horizontal Polarization (A320).

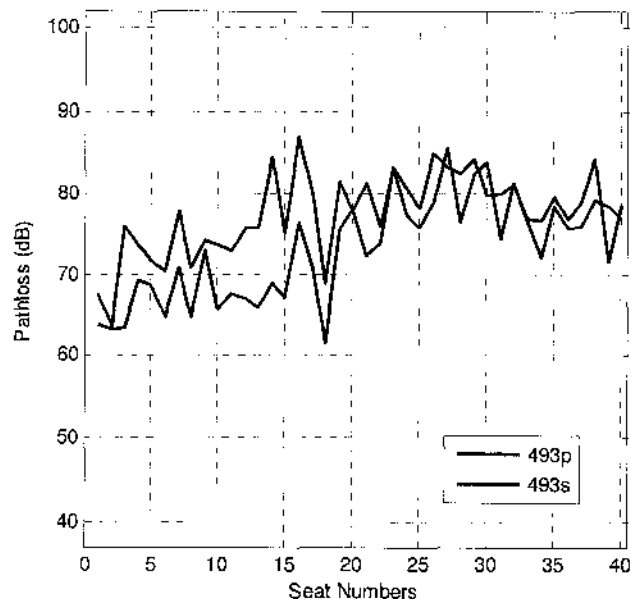


Figure 41. IPL Data for LOC-L in Horizontal Polarization (A320).

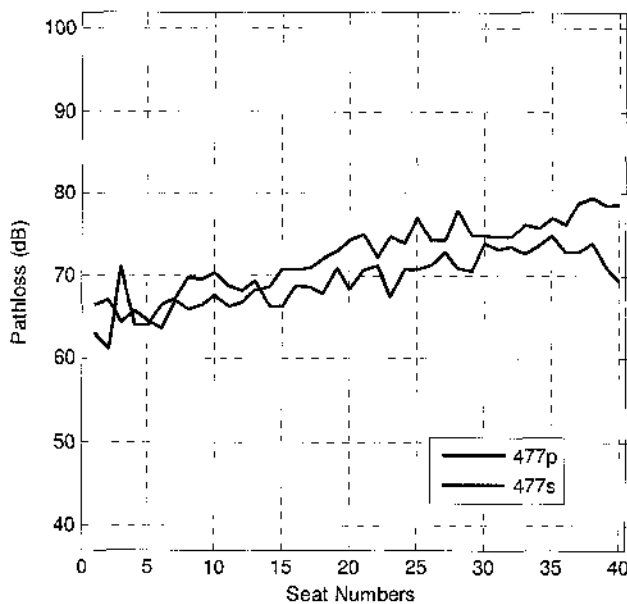


Figure 42. IPL Data for DME-L in Vertical Polarization (A320).

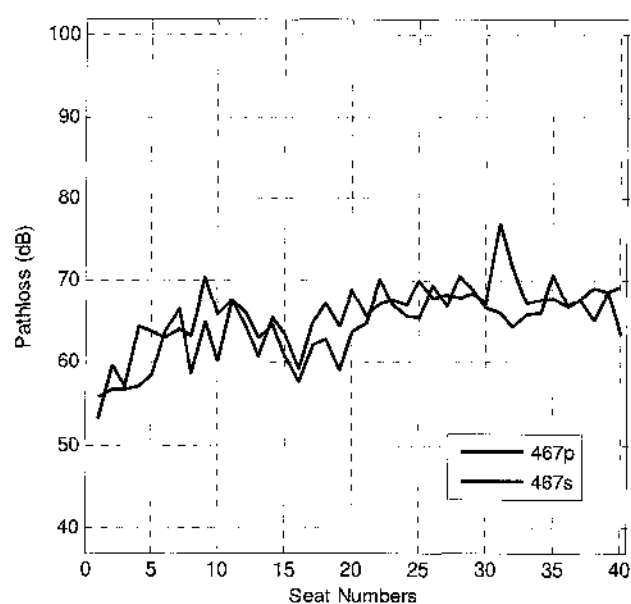


Figure 43. IPL Data for VHF-L in Vertical Polarization (A320).

Figure 44 shows the IPL pattern for ATC-T on A320. Similar to A319, the ATC-T on A320 is located approximately on top of the second window of the aircraft. A trend of low to high pathloss is again observed in the IPL pattern from the front of the aircraft

to the rear. However, there exists unwanted deviation (more than 10 dB) between the measurements from the port and starboard sides.

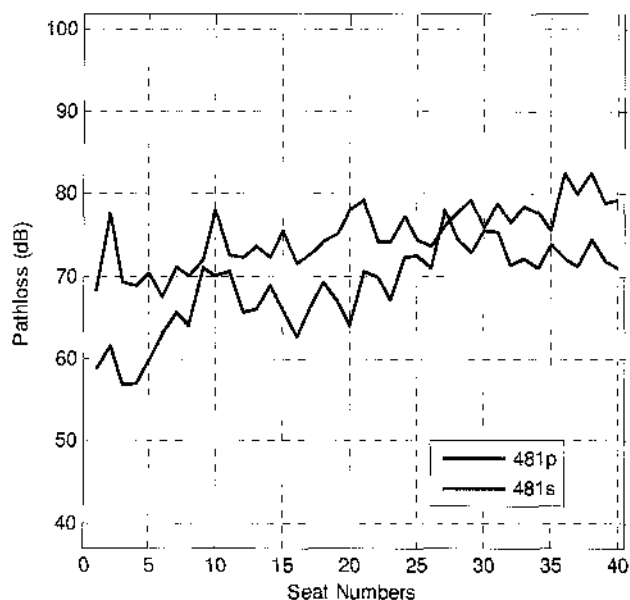


Figure 44. IPL Data for ATC-T in Vertical Polarization (A320).

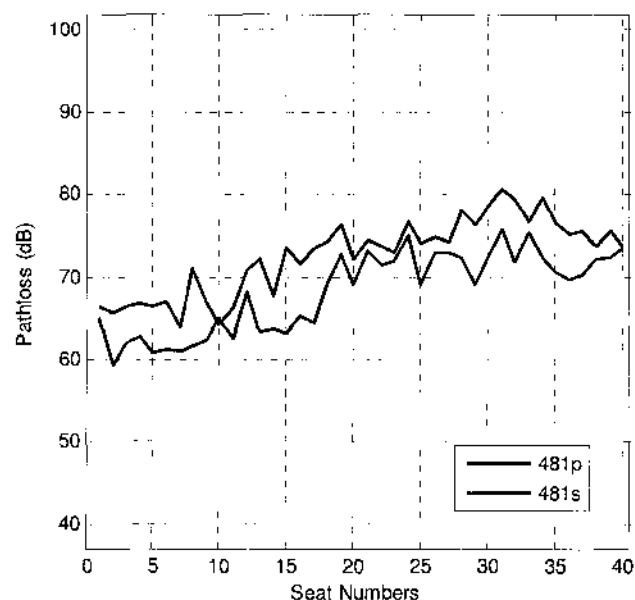


Figure 45. IPL Data for ATC-B in Vertical Polarization (A320).

The IPL patterns for A320's ATC-B are presented in Figure 45. ATC-B is located at the bottom centerline of the fuselage beneath window 1. Similar to ATC-T, an increasing trend of pathloss values is observed from the front to the rear of the aircraft. There is no significant drop in pathloss observed at the emergency exits of A320.

Figure 46 shows the IPL pattern for A320's GPS-L in vertical polarization. Recall that GPS is actually a circularly polarized system. In A320, GPS-L is installed approximately before the first exit, on top of the fuselage. In the IPL pattern for vertical polarization, there exists an increasing trend from low to high pathloss values from the first to the last window. Figure 47 shows the IPL pattern for A320's GPS-L in horizontal polarization. A similar increasing trend can also be observed in the plot with horizontal polarization. Although the increasing trends agree with our previous graphical analysis on the relationship of IPL patterns based on the location of exits and antenna location, GPS-L will not be considered for modeling due to its circularly polarized characteristics.

The VHF-C system is located near window 30 on top of A320's fuselage. Figure 48 shows the IPL patterns obtained for VHF-C on A320. Similar to previous VHF-C patterns, there exist low pathloss at windows closest to the location of the antenna. The

pathloss increases as the distance from transmitting source to aircraft antenna increases. Furthermore, low pathloss values are again observed near the emergency exits and rear exit of the aircraft.

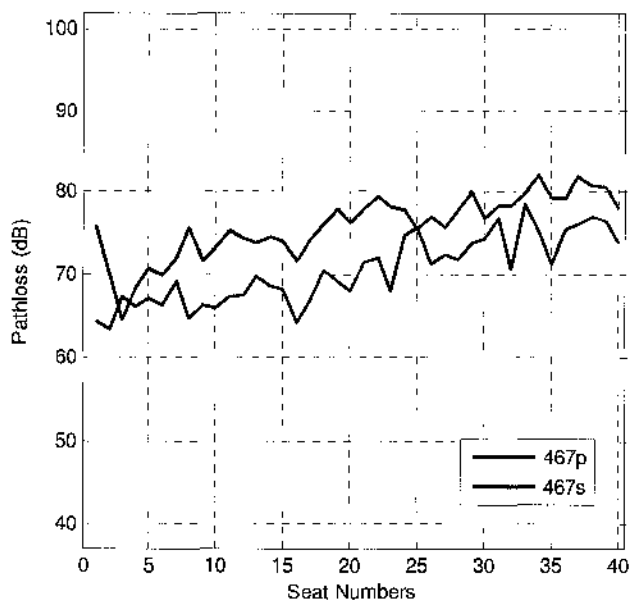


Figure 46. IPL Data for GPS-L in Vertical Polarization (A320).

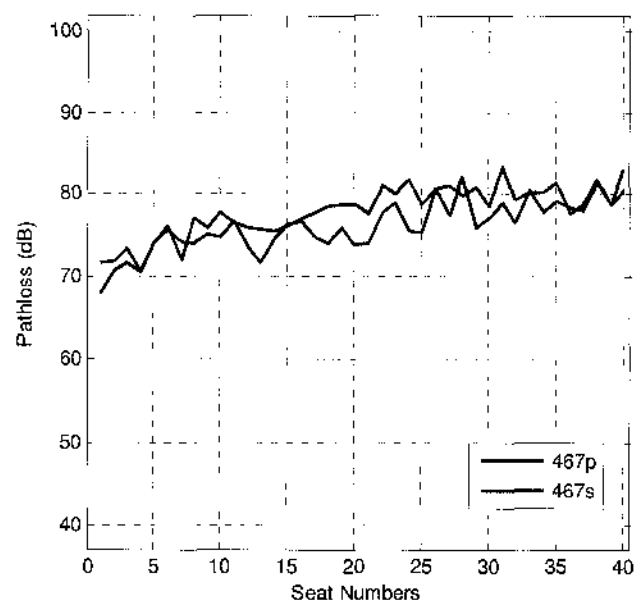


Figure 47. IPL Data for GPS-L in Horizontal Polarization (A320).

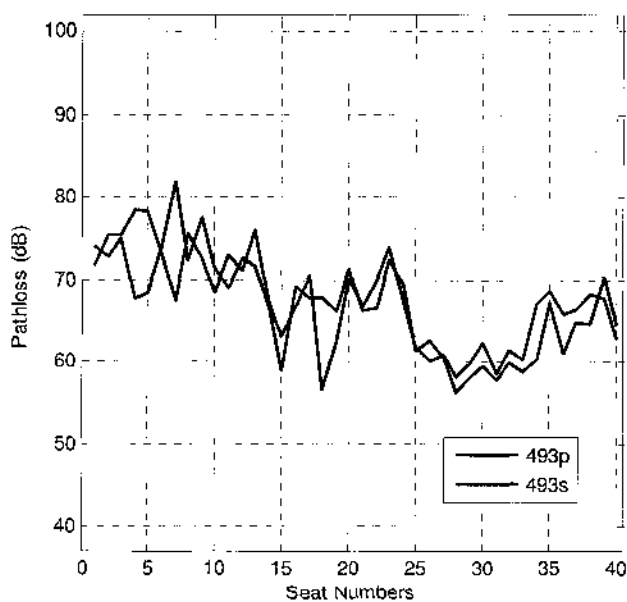


Figure 48. IPL Data for VHF-C in Vertical Polarization (A320).

Figures 49, 50, 51 and 52 show a summary of all IPL patterns for all systems measured for B737, B757, A319 and A320 respectively. Only mean IPL values for the repeated trials are shown. The purpose of these plots is to comprehend the range of

pathloss values for each aircraft. The pathloss values for almost all systems reside between 50 dB to 80 dB in all four aircraft types.

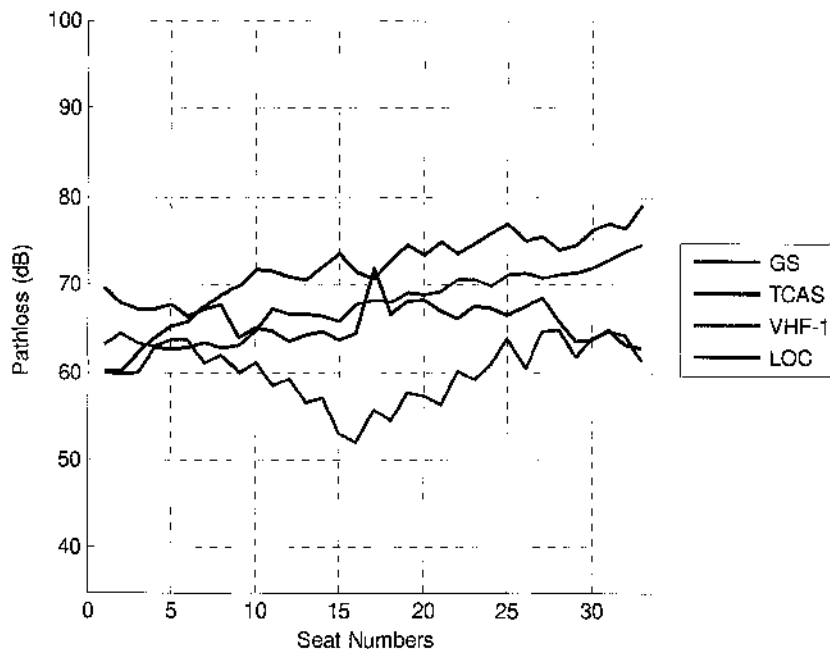


Figure 49. Mean IPL Data for All Systems in B737.

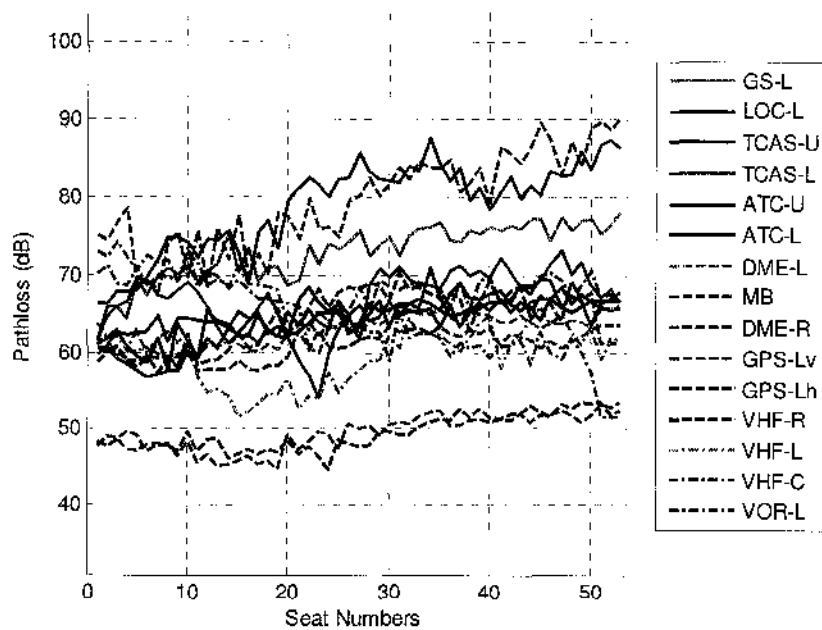


Figure 50. Mean IPL Data for All Systems in B757.

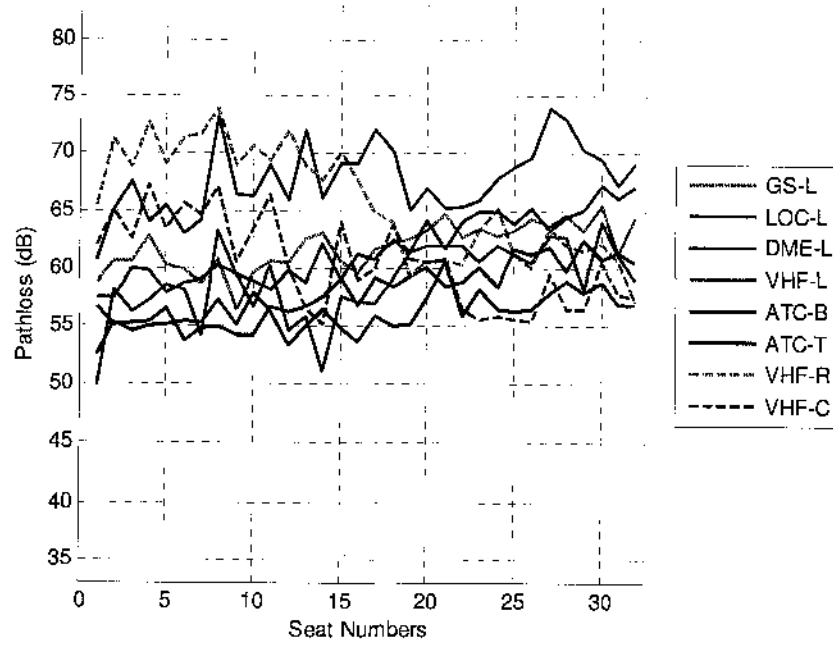


Figure 51. Mean IPL Data for All Systems in A319.

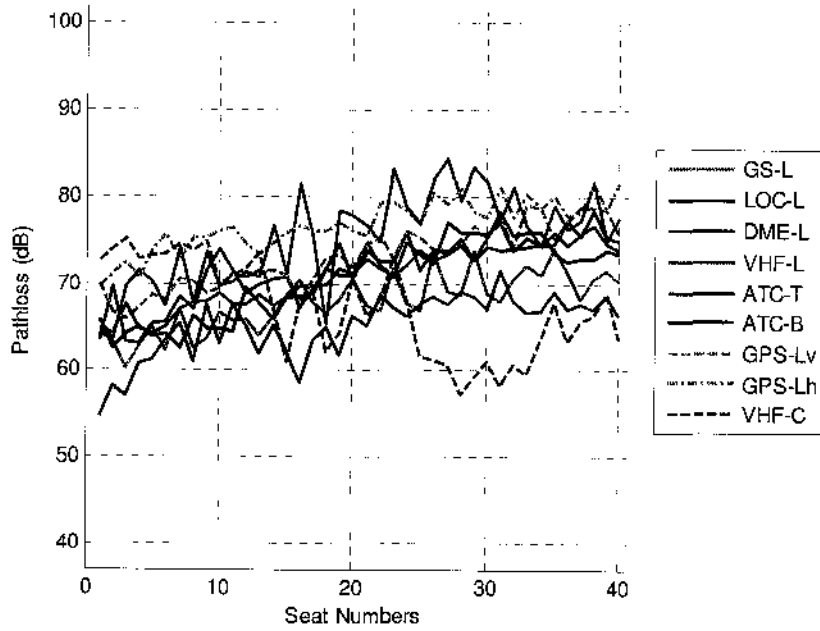


Figure 52. Mean IPL Data for All Systems in A320.

CHAPTER 3

METHODOLOGY

One of the major objectives of this dissertation was to effectively model the IPL patterns for all systems on various aircraft types. As mentioned in the introduction, modeling can be performed using either analytical, numerical or expert system techniques. Analytical techniques make simplifying assumptions about the geometry of a problem in order to apply a closed-form (or look-up table) solution. Numerical techniques attempt to solve fundamental field equations directly, subject to the boundary constraints posed by the geometry. Expert systems do not calculate the fields directly, but instead estimate values for the parameters of interest based on a rules database.

To date, there exists no model which effectively predicts IPL values at every window location of various aircraft for each antenna system. Limited success has been achieved by some investigators [46-48]. Georgakopoulos *et al.* use FDTD to model IPL levels at a selected window. They compare their results to a scaled-model of B757 (rectangular structure with slits for windows). Although they did not compute an overall IPL pattern on all windows, the coupling values on a selected window compared well with actual measurements on the mock-up aircraft between 2.5 to 3 GHz frequency ranges. Devereux, *et al.*, first attempt to use MoM to simulate IPL on windows of a mock-up aircraft for VHF; however, due to limited computational resources, they perform the same task using FDTD. The results are comparable to the IPL patterns recorded for VHF antenna and are promised to be accurate for frequency ranges less than 300 MHz. Unlike other methods, Vahala, *et al.*, use a high speed multiple scattering approach by solving the Maxwell's equations in the parabolic form. The results of their simulation are comparable to the real IPL data in high frequencies (greater than 1 GHz).

Due to the novelty of this problem, analytical, numerical as well as expert-system based approaches are discussed in this section to finalize which technique will produce the "best" model for the IPL predictions. As mentioned in Appendix A: IPL Measurement Overview, measurement of the IPL values at each window in both horizontal and vertical polarization is a very time consuming and expensive task. Therefore, the "best" model for IPL prediction shall eliminate the need for data

collection. The model shall be the most efficient in terms of predictability speed, as well as cost effective. Intuitively, the predicted IPL patterns by the model shall resemble the actual IPL data. Finally, the initial set-up and analysis of output shall be user-friendly to produce fastest and most accurate IPL results. The next few sub-sections discuss the possible numerical techniques which are applicable to this research and have been used previously. Finally, the reasoning behind and the methodology of the final IPL prediction design using expert systems is discussed.

3.1 Overview of Techniques used for EMI prediction inside Commercial Aircraft

Numerical and analytical methods can be useful for understanding the phenomenon displayed in the plotted IPL data in chapter 2. Both the normative behavior and the seeming irregularities can be supported. The actual modeling can be broken into several parts, specifically [50]:

1. Characterizing the energy fields inside aircraft compartments containing a source
2. Characterizing the real or effective source at windows or other apertures
3. Determining the fields, currents and path loss at or near the aircraft's external surface on the path from apertures to antenna locations
4. Determining the field levels in the avionics compartments from sources in other internal compartments as well as outside but nearby the aircraft

The code and models must be validated to ensure that the results are in the correct order of magnitude (± 6 to 10 dB) [50]. The basic objective is to simulate the effects of an electromagnetic source within the aircraft cabin, determine the amount of leakage through the windows of the cabin, and the amount of interference received by external aircraft antennas or internal avionics. This is a very complex problem to model since the frequencies of interest cover the range of below 100 MHz to often above 3 GHz. The aircraft cabin are often multiple wavelengths and resonance effects must be included in the simulation [50].

Analytical techniques are useful for small-structure modeling. Therefore, these techniques can not be used for the case of large passenger aircraft such as B737, B757, A319 or A320. Assuming a frequency of 3 GHz, a sample radius of these aircraft type is about 4 meters, leading to a commercial aircraft to be approximately 40 wavelengths in

diameter and greater than 300 wavelengths in length (assuming a minimum length of about 30 meters). Therefore analytical techniques are not applicable for an application of this scale.

A table that includes a list of available codes and a short summary of their features can be found in [50]. The following few sections summarize a few numerical techniques and how they can or cannot be applied to this application.

3.1.1 Far Field Techniques

Far-field techniques, such as ray tracing and geometric theory of diffraction are used extensively for radar cross section and antenna pattern determination [51-54]. These techniques all require the distance to be many wavelengths from the source, and assume plane-wave fields. Larger aircraft structures qualify for these techniques in the high frequencies (3 GHz). However, when considering smaller frequencies, i.e. 100 MHz, the diameter of the aircraft can be as small as $\frac{3}{4}$ of a wavelength in diameter or 10 wavelengths in length. Furthermore, the window apertures (sources of leakage) are even smaller in the above calculated wavelengths. Therefore, far-field techniques are not appropriate for smaller frequencies of this application.

Vahala *et al.* extend ray tracing to a quasi-ray tracing algorithm by using a multi-scattering approach. Instead of a direct solution to Maxwell's equations, they utilize the multiscattering formalism that solves a stochastic parabolic wave equation. The solution of the stochastic parabolic equation for complex problems dramatically reduces the computational time by many orders of magnitude. The algorithm takes into account only forward scattering and is therefore not compromised by the usual divergences that arise from ray crossings in the traditional ray tracing approach. In the algorithm, backscatter effects are deemed negligible and the axial propagation direction of the wave down the fuselage becomes the time coordinate in the resulting parabolic wave equation [46, 55, 56]. The results from this multi-scattering approach match well with actual measured IPL data and are attained computationally fast; however, the algorithm is limited to high frequencies (greater than 1 GHz) and involves modeling the complex interior of the aircraft, including the dielectric properties of interior apertures (i.e. seats).

3.1.2 Method of Moments

The MoM is a commonly used full-wave frequency domain approach whereby the RF currents are found everywhere on a metal structure due to a specified source. Figure 53 shows an example of current calculation along a selected direction on a simulated sphere [57]. Notice that the currents converge to almost 0 near the pole of the sphere. Assuming that the E-field is coming out of the converging pole of the sphere, there is no component normal to the surface: i.e., there exists no charge along this meridian. Therefore, there would be zero current running tangentially along the zero charge meridian, having time invariant vanishing electric field.



Figure 53. Schematic of Current Calculation Using Method of Moments.

The purpose of this example is to show that MoM is very useful for applications with long wires or appreciable distances to the observation point; however, MoM is not appropriate for problems involving leakage through apertures, since the currents are assumed to be constant closer to sharply curved surfaces [58]. Therefore, in the case of indoor to outdoor propagation, the MoM technique will not be able to transition smoothly from inside to outside through window apertures. However, MoM can be an excellent technique to be used for outdoor coupling on a smooth metal fuselage.

Devereux, *et al.*, used an example of a reduced size aircraft model (shown in Figure 54) to determine the RF pathloss between windows in the passenger compartment and the various VHF and UHF receive antennas on the outside of an aircraft. In their design, the windows were considered to be the source of the RF energy, so the model's domain was only on the outside of the aircraft [47].

A MoM model of the aircraft cylinder was created using a wire mesh frame (depicted in Figure 56) containing over 4000 wire segments. The MoM simulations were performed on both a personal computer (PC) and a Silicon Graphics Inc. (SGI) Onyx Workstation [47]. Due to limited memory of the PC; however, only a 2000 segment, 1/3 section of the cylinder with windows, shown in Figure 56, was used to compare results to the full model operating on the Onyx. Devereuxm, *et al.*, reported low similarity between the full versus sectional modeled results from PC and Onyx. Furthermore, the full MoM model simulated using Onyx took an excessive time to run; therefore, causing the designers to look toward using FDTD for more promising results.

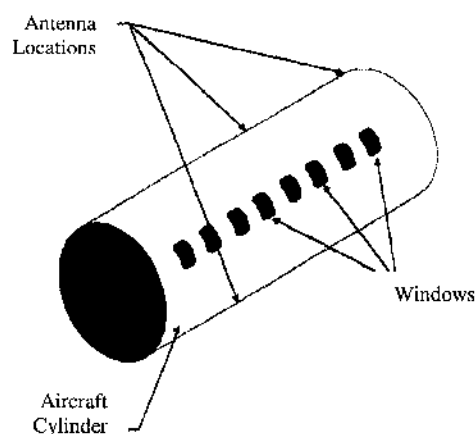


Figure 54. Reduced Aircraft Model.

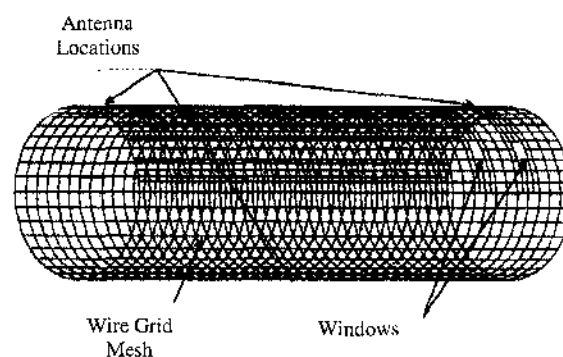


Figure 55. Wire Mesh Representation for Method of Moments.

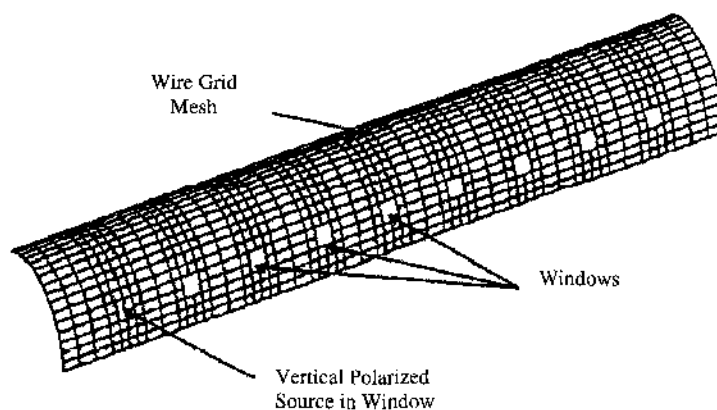


Figure 56. Reduced Wire Mesh Representation for Method of Moments.

3.1.3 The Finite-Difference Time Domain Method

The FDTD approach has become very popular over the last few years for EMI and EMC applications. FDTD is a full-wave, volume-based approach where the volume

of space containing the problem is partitioned into small cubes, and the Maxwell's equations are solved directly using a central difference scheme. The electric and magnetic fields are solved directly using a leap frog approach, where the field components are offset in time and space to ensure greater accuracy in approximating their derivatives. FDTD is a time domain method, so by using a fast Fourier transform on the FDTD results, a wide range of frequencies can be solved with one FDTD simulation [48, 50, 59, 60].

Devereux *et al.* used the FDTD model to predict normalized coupling values on the aircraft's modeled cylinder previously presented in Figure 54. The FDTD computational domain was broken into 10 cm cubed cells, providing accurate results at frequencies up to 300 MHz. Figure 57 shows the results for VHF in vertical polarization (with the antenna placed on top of window #7). Figure 58 shows the results for VHF in horizontal polarization. The several trials in both figures refer to the various frequencies in the frequency band of VHF (116 – 138 MHz) [50].

The model predicts the greatest coupling directly beneath the mounted antenna in vertical polarization, while the coupling is lowest in horizontal polarization underneath the installed system. The advantage of this technique is the obvious ability to effectively predict the pathloss values in a scaled aircraft; however, the disadvantage is the limitation of the model to low frequencies. If the modeled frequencies are increased to be greater than 300 MHz, this would increase the computational time extensively. Furthermore, an extension of the cylindrical fuselage to include nose and tail of the aircraft, to analyze nose-mounted and tail-mounted systems, will further increase the computational time perhaps even reducing the ability to effectively compute coupling values for frequencies up to 300 MHz.

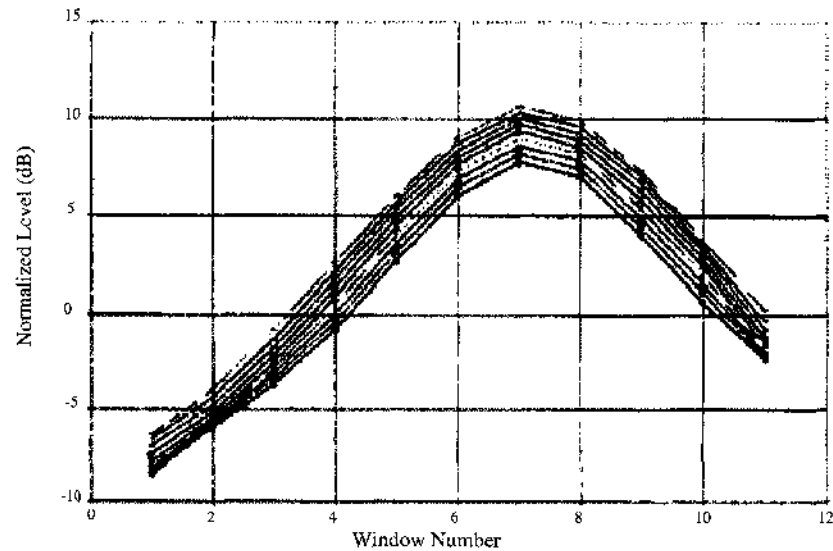


Figure 57. VHF Prediction in Vertical Polarization using FDTD [53].

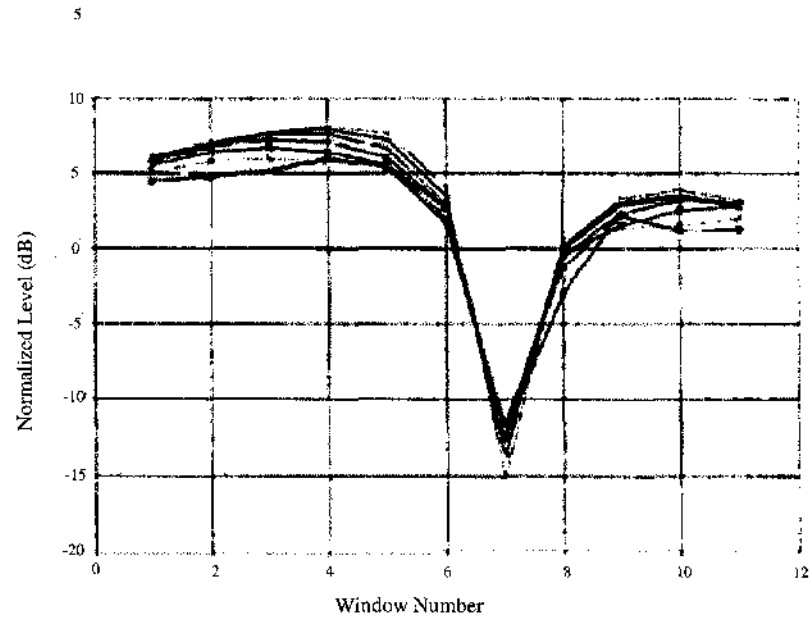


Figure 58. VHF Prediction in Horizontal Polarization using FDTD [53].

Georgakopoulos *et al.* extended the applicability of using FDTD on higher frequencies by creating cell sizes of 2.5 mm in a rectangular mock-up model of the aircraft, shown in Figure 59. With the selected cell size, they expected the FDTD simulations to provide accurate results up to 9 GHz. This simulation, however, yields a very large computational domain of 620 x 80 x 96 cells and required 114 MB just for electric and magnetic field computations [48]. Therefore, simulating this problem requires a very large amount of computational resources, memory as well as time.

Especially the memory issue is more restrictive since if the required memory is not available, then the simulation can not be performed.

The results of the FDTD model matched measured results closely for up to 5 GHz. Georgakopoulos *et al.* further extended their model to a hybrid FDTD model, where they used different grid sizes in selected parts of the simulated fuselage [48]. The new results were similar in accuracy as the original FDTD model; however, the hybrid technique utilized lesser computational memory (48 MB instead of 114 MB in the original model). It is important to note that in order to attain the full IPL pattern throughout the entire simulated aircraft, the FDTD simulations need to be performed at each window location. Therefore, the computational time is to be multiplied by the number of windows.

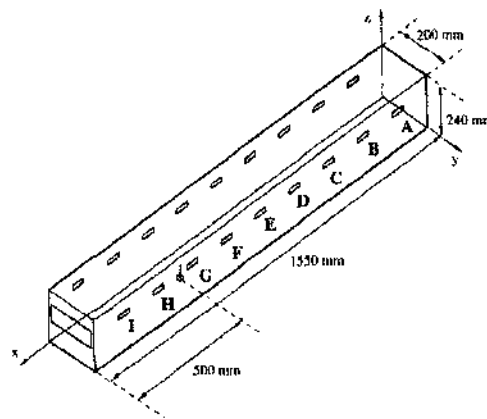


Figure 59. Rectangular Aircraft Model.

Modeling results by Georgakopoulos *et al.* and Devereux *et al.* show successful IPL predictions on a down-scaled version of an aircraft. Although the predictions are accurate, the computation time and resources requirement for the simulations is extensive. Therefore, FDTD will not be considered for modeling purposes in this dissertation.

3.1.4 Fuzzy Logic

Modeling of IPL patterns onboard B737 using fuzzy logic has been accomplished in the Master's thesis [23]. The idea of fuzzy logic was applicable for this application due to the presence of patterns in the pathloss data due to the location of the antenna, aircraft doors and emergency exits. These patterns are summarized for each system in

Chapter 2. Three rules were created using these patterns: in particular, coupling values were expected to increase

- a. as the distance from antenna decreases,
- b. as the distance from aircraft's main exit and emergency exit decreases,
- c. as the distance from the windows decreases [This is because the IPL pattern is predicted for the entire aircraft, instead of just window locations] [43].

The modeling results seemed very comparable to the actual measured results as depicted in Figure 60 (top and bottom, respectively).

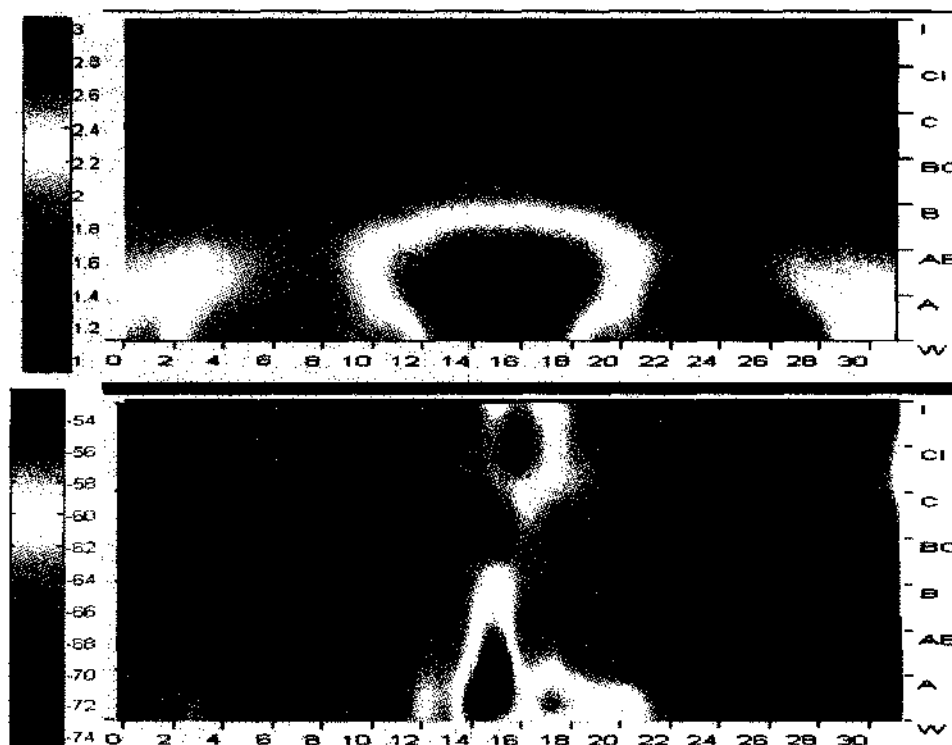


Figure 60. IPL Pattern Prediction (top) for VHF-L using Fuzzy Logic.

Compared to numerical techniques, fuzzy logic was computationally very efficient, providing results within seconds after inputting the location of aircraft doors, windows and antenna. The results were also very comparable to actual data after defuzzification (not shown in the figure) in both low to high frequencies (VHF to TCAS). However, the model assumed a rectangular fuselage, similar to the work by Georgakopoulos *et al.* [48]; therefore eliminating the capability of modeling systems mounted on the nose or tail of the aircraft. Fuzzy logic will be extended in this work to include rules for systems mounted on the nose and tail of all aircraft.

3.1.5 Neural Networks

Recent work by Jafri *et al.* include IPL predictions on B757, A319 and A320 using feed forward neural networks [27, 28]. Figure 61 shows a sample predicted output for A320's VHF-L. The green lines represent the training data patterns using by neural networks for training. The solid red lines represent the actual IPL data to be predicted by the NN, while the dashed red line represents the IPL patterns predicted by NN. In the case for VHF-L, the predicted IPL pattern followed actual data accurately; however, the prediction was not as comparable for other systems (i.e. DME, LOC etc.).

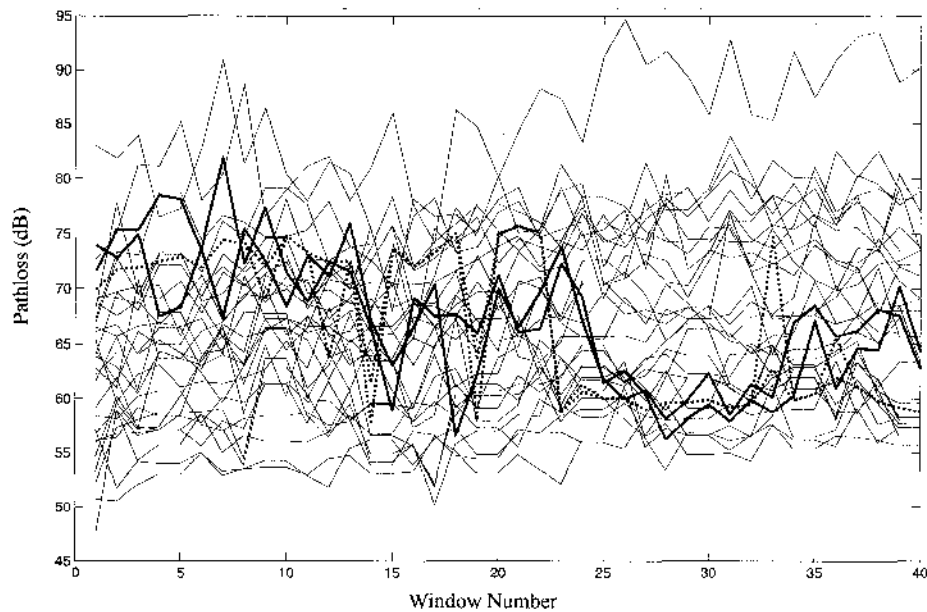


Figure 61. IPL Pattern Prediction for VHF-L using Neural Networks.

NNs are another faster alternative to other numerical techniques such as MoM and FDTD. While they take longer time to simulate (due to training) than fuzzy logic, a typical training and prediction session takes around 5 minutes to complete on a standard PC. Similar to fuzzy logic, NNs have been able to model aircraft systems in all frequencies (from low to high), instead of being limited to some frequency range. For the particular application of IPL prediction, modeling results were obtained relative to actual IPL values in dB for the first time, compared to the normalized values obtained in previously mentioned techniques. Due to all these advantages, NNs will be studied again in this work; however, further enhancements to the NN structure will be considered to improve the modeling on other systems.

3.2 Selected Model's Design Detail

Due to the success of previous modeling using fuzzy logic and neural networks, these approaches will be enhanced and used together for a more effective modeling of IPL data on aircraft. Previous results from fuzzy logic validated well with measured data; however, the overall pattern lacked the non-linear effects found in the overall IPL patterns. Similarly, the results from neural networks also validated well with actual IPL data, in terms of an overall mean and standard deviation; but, the neural networks incorporated the non-linear relationships more than the simple linear ones for the locations of doors and antenna. Both models are computationally efficient; therefore, a modulated architecture was utilized to incorporate linear and expert knowledge in the model using the fuzzy logic module, while incorporate the non-linear, unobservable knowledge in the model using feed forward neural networks. The model should satisfy the following objectives:

1. Model should be efficient, user-friendly, and require minimal inputs.
2. Model should utilize expert knowledge gained from analysis of IPL patterns.
3. The output IPL pattern predictions should match well with the measured IPL data in both low and high frequencies.
4. The output IPL pattern predictions should be scaled appropriately (in dB), and not normalized.
5. Model should be computationally efficient.

The following sections go over the proposed architecture and details of the new Neuro-Fuzzy model (NFM).

3.2.1 Input Data Selection

An important step in modeling is to select appropriate inputs. As desired by the first objective of this model, minimal input should be used to produce an effective IPL pattern for the selected aircraft system of concern. Therefore, only the data most readily available for most aircraft was selected as the inputs of the model. These inputs included:

1. Aircraft's Length: The length, width and height of the aircraft are obtainable through most manufacturer websites. Figure 62, Figure 63, Figure 64, and Figure 65 include the basic schematics for B737, B757, A319 and A320 respectively. Using these schematics, the length was measured in centimeters for accuracy

purposes and used as the first input to the NFM. Width and height of the aircraft were not considered in the model due to the similarity of these values among the four aircraft of concern. These characteristics may be added in future work to increase prediction effectiveness on smaller or larger aircraft types. Also, unlike previous models, the length characteristics of the aircraft were acquired using a 1:1 scale.

2. Number of windows: Inputting the proper number of windows was needed for final IPL predictions. The number of windows varied among all four aircraft; therefore, this characteristic was needed for proper IPL pattern alignment on the x-axis of IPL plots. The number of windows were also used for indexing purposes for reading in actual IPL data for training purposes.
3. Number of Major exits: As observed in the plotted IPL patterns, the number and locations of doors had significant effect on the coupling levels. This number of major exits only referred to exits on the port side of the aircraft, and did not take into account the exits located on the starboard side. Among the four aircraft of concern in this application, only B757 had 3 major exits, while B737, A319 and A320 had 2 exits each on the port sides.
4. Location of Exit 1: Using the CAD schematics provided in Figure 62, Figure 63, Figure 64 and Figure 65, the locations of the first exit were determined using careful approximations. The actual values of the exits may also be obtained from the manufacturers; however, they are not specified in the CAD drawings available for public use. The first exit corresponded to the exit closest to the nose or cockpit of the aircraft.
5. Location of Exit 2: Similar to the previous input, the location of the second exit is also specified by making careful measurement approximations.
6. Location of Exit 3: B757 has three main exits, while B737, A319 and A320 all have only two exits on the port sides. Therefore, based on the value of input number 3, the last exit was carefully approximated if a third major exit was present in the aircraft of concern. The last exit corresponded to the exit closest to the tail of the aircraft. For the aircraft with no third exit, the value of the second

exit was duplicated in this entry to have consistent number of inputs for the fuzzy logic.

7. Number of Emergency Exits: The IPL values were not only getting influenced by the location of the main exits, but from the emergency exits as well. Therefore, this entry determined the number of emergency exits in the aircraft of concern. For example, B737 and A319 have one emergency exit, while B757 and A320 have two emergency exits each on the port sides.
8. Location of Emergency Exit 1: The location of emergency exit 1 was determined through approximation from the schematics in Figure 62, Figure 63, Figure 64 and Figure 65 again.
9. Location of Emergency Exit 2: If a second exit existed (for the cases of B757 and A320), this value was calculated using the CAD schematics. However, for systems with one emergency exit, the value of the first emergency exit was duplicated for this entry for input consistency purposes.
10. Location of Antenna System (x-direction): The location of the antenna played a very significant role in determining the trends in the IPL patterns. Although the locations of antenna are not specified in the CAD schematics, this information was acquired during real-time testing. For example, for B737, it was determined that VHF-L was located on top of window 16 etc. Therefore, for this entry, the locations of the antenna systems were determined by approximating the distance on the closest relative window to the antenna (either below or above the antenna). For nose and tail mounted systems, the distances were approximated through the CAD schematics. This particular entry included measurement of the antenna system with respect to the nose of the aircraft in the x-direction (i.e. horizontal distance from nose toward tail).
11. Location of Antenna System (y-direction): Some antennas are mounted on top of the fuselage, while others are mounted on the bottom. Therefore, this entry determined the location of the antenna systems in the y-axis, or vertical direction. The centerline ($y=0$) was determined to be the centerline of the fuselage. Therefore, if the radius of an aircraft was 200 cm, then systems along the fuselage may be mounted on +200 cm, or -200 cm, for top or bottom mounts, respectively.

For nose and tail mounted system, these values were calculated to be different than just the radius of the aircraft.

12. Start Frequency of Antenna System: In the IPL plots, it was observed that systems with high operating frequencies (such as TCAS, DME, ATC) did not vary much in pathloss values from the front to the rear of the aircraft, while systems like VHF appeared to show much more dependence on their mounting location. Although clear conclusions could not be made due to the high variation in some datasets, the operating frequencies were considered to be important inputs for determining pathloss. Therefore, this entry included the start frequency used to perform the IPL measurements. This entry was not solely the operating frequency (as some systems operate on a single frequency, such as TCAS (1090 MHz)), but instead, it was the start frequency of the sweep performed during testing. For example, the frequency sweep for TCAS was 1080 to 1100 MHz; therefore, making this entry 1080 MHz as the start frequency for TCAS.
13. Stop Frequency of Antenna System: The stop frequency for all systems was assigned to this entry.
14. Dominant Polarization of Antenna System: Antenna polarization has a large effect on the pathloss pattern. Therefore, polarization was depicted in this entry using Boolean logic. For example, this entry was 0 for systems with horizontal polarizations, and 1 for systems with vertical polarizations. Since GPS was not considered in this modeling, circular polarization assignment was not of concern, although another value (such as 0.5) can easily represent circular polarization type.

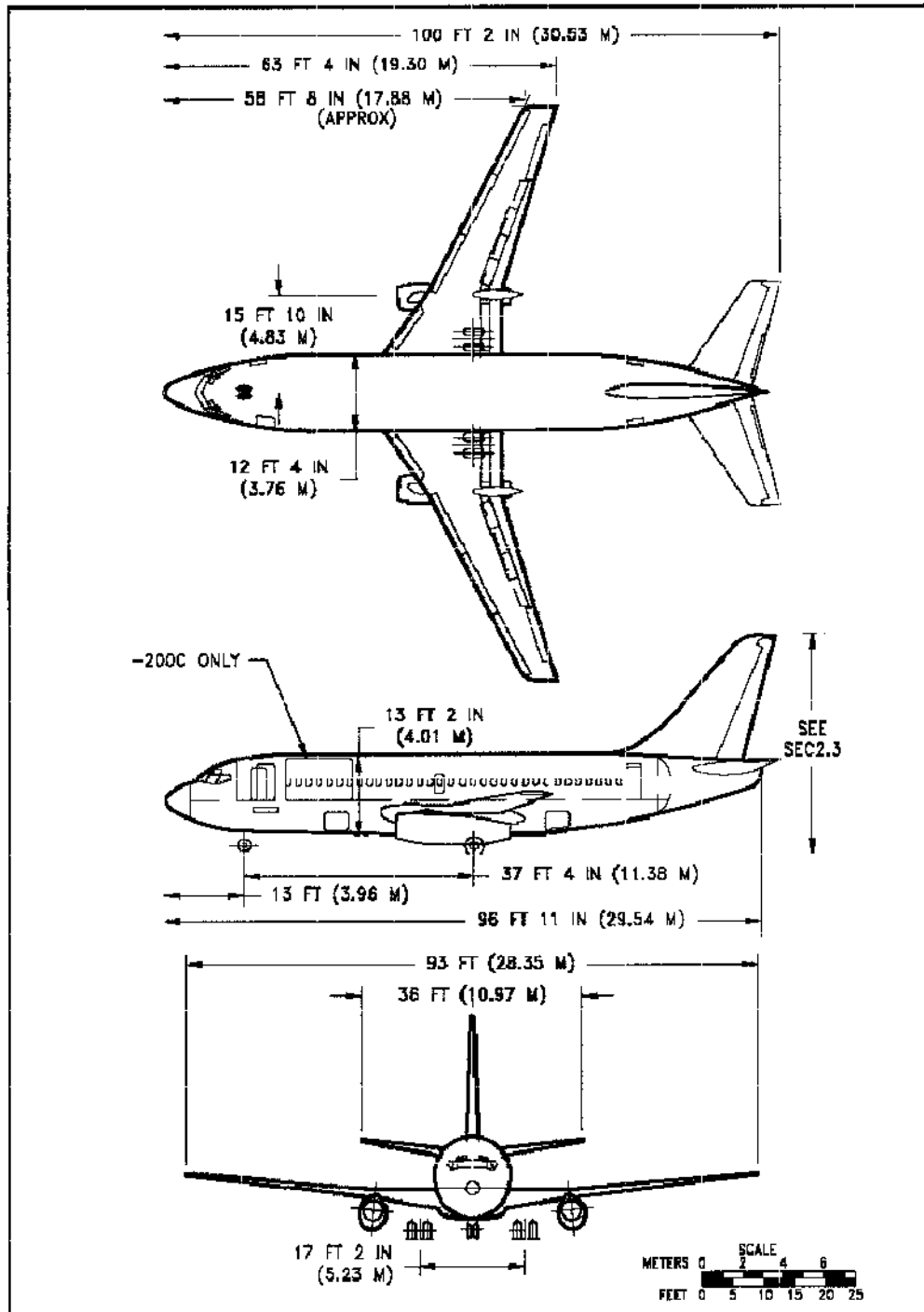


Figure 62. Auto-CAD Drawings of B737 [61].

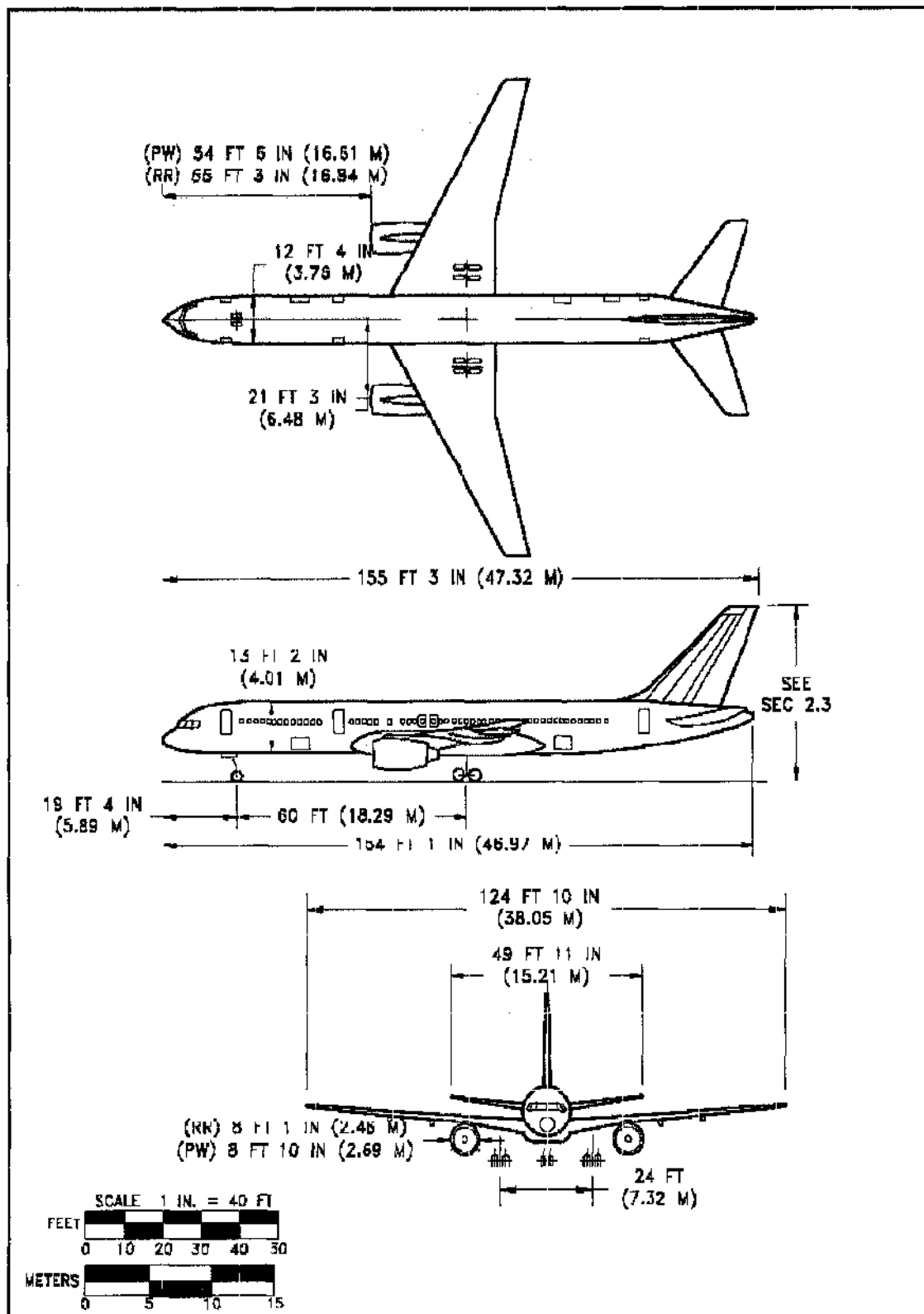


Figure 63. Auto-CAD Drawings of B757 [62].

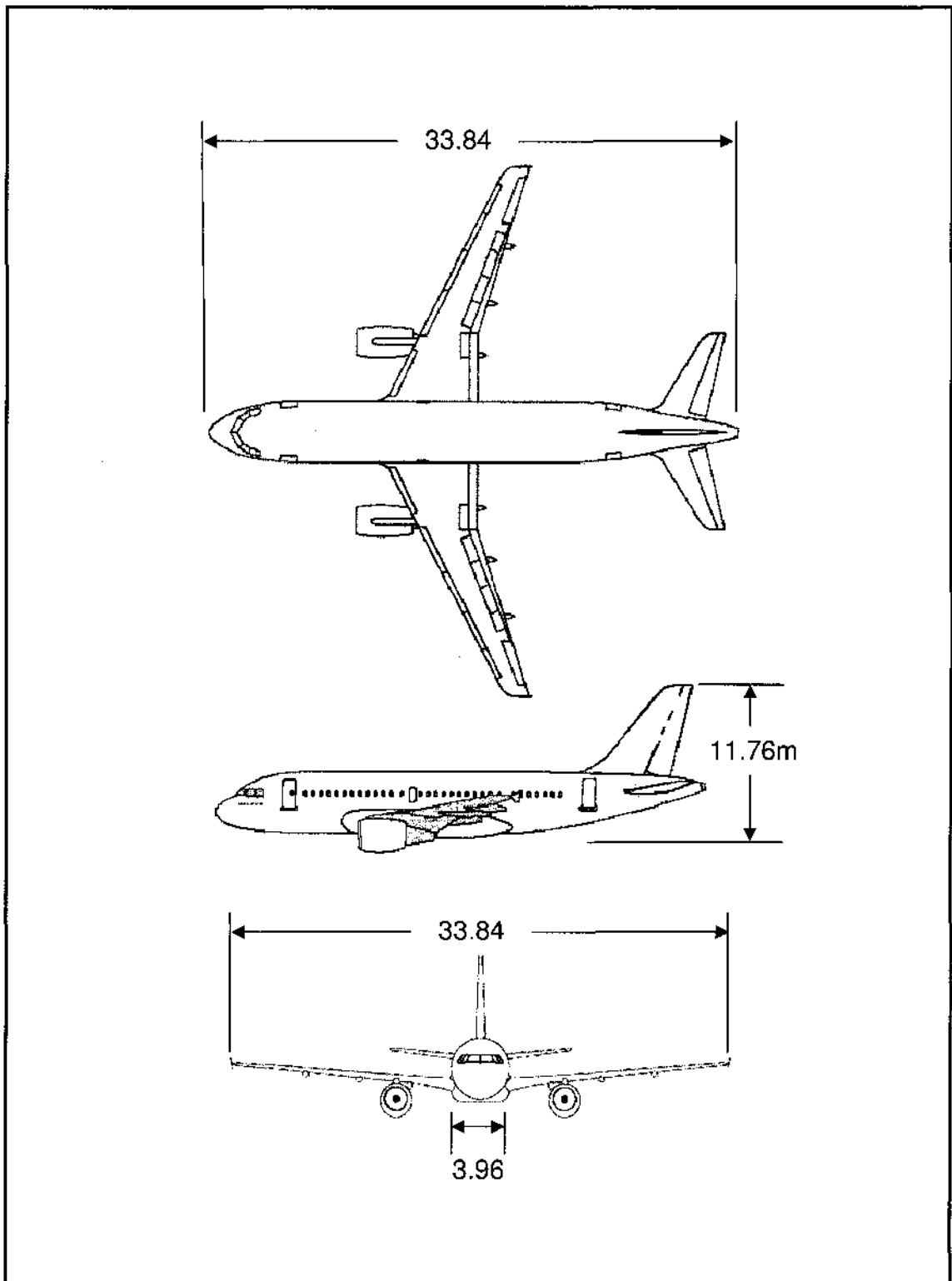


Figure 64. Auto-CAD Drawings of A319 [63]

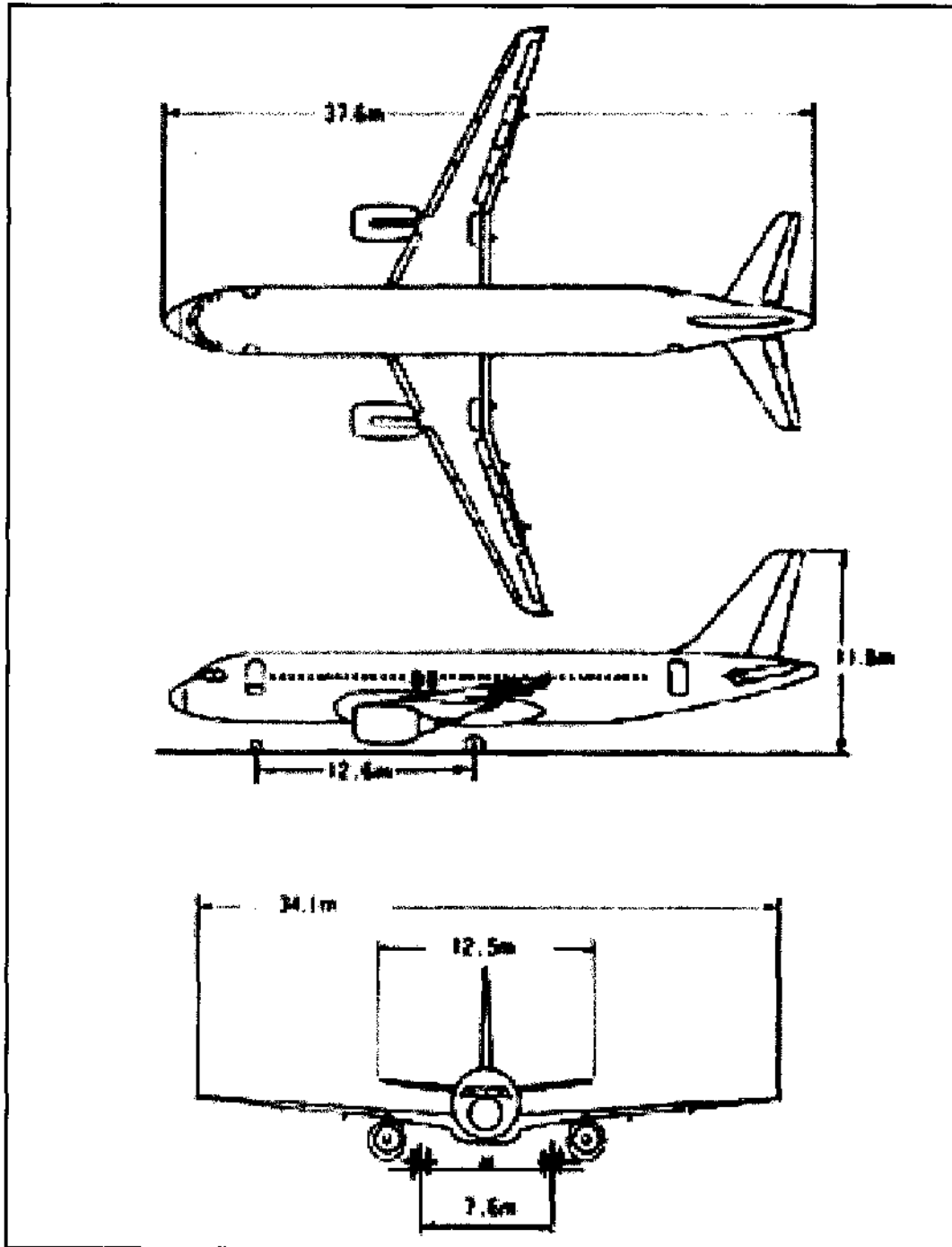


Figure 65. Auto-CAD Drawings of A320 [64].

3.2.2 Neuro Fuzzy Model: System Architecture

Neural networks and fuzzy logic have been applied individually to predict IPL data in previous work [23, 27, 28, 43]. Although the results were promising, the two stand-alone models had weaknesses. In the fuzzy model, although the linear relationships such as pathloss influence from the locations of doors and antenna locations were incorporated - the non-linear relationships, such as random noise and unknown structural influences, were not included. Although the final predicted IPL patterns showed the increasing trends, and the peaks and valleys in the pathloss values nevertheless they did not match the real-world IPL data closely when more noise and other unknown external factors were included. Similarly, the neural networks as a stand alone model predicted the IPL pattern well for many systems; however, for the outputs that were inaccurate, there was very little user-control to make the model better.

The overall system architecture for the newly proposed Neuro-Fuzzy Model (NFM) is depicted in Figure 66. Neural Networks and Fuzzy logic were combined to input expert, or linear, knowledge as well as un-known, or non-linear, characteristics into the IPL pattern prediction. The expert knowledge was incorporated into the first module of the model using fuzzy logic and smaller neural networks. The second module incorporated the unknown non-linear patterns into the IPL pattern using the outputs from the linear model as well as training from real IPL data using neural networks. The following sections include details of the two modules.

3.2.3 Neuro-Fuzzy Models' Linear IPL Predictions

Incorporation of linear characteristics in IPL patterns was performed using expert knowledge in fuzzy logic. Briefly, a set of rules were created to relate the effect of the antenna and exit locations on IPL patterns on various systems of concern. Then the aircraft and system characteristics, described in section 3.2.1, were input and applied to the set of rules. The output from the rules were then combined and then passed onto the defuzzification module, which used a small artificial neural network to first determine the minimum and maximum IPL value for the system of concern, then defuzzified the fuzzy IPL values into crisp values using the predicted minimum and maximum values. The crisp IPL values for the aircraft and system of concern were then reduced to be sent over to the Neural networks for non-linear characteristics' incorporation. The flowchart in Figure 67

outlines this algorithm while the following subsections go into the detail of each process in the flowchart.

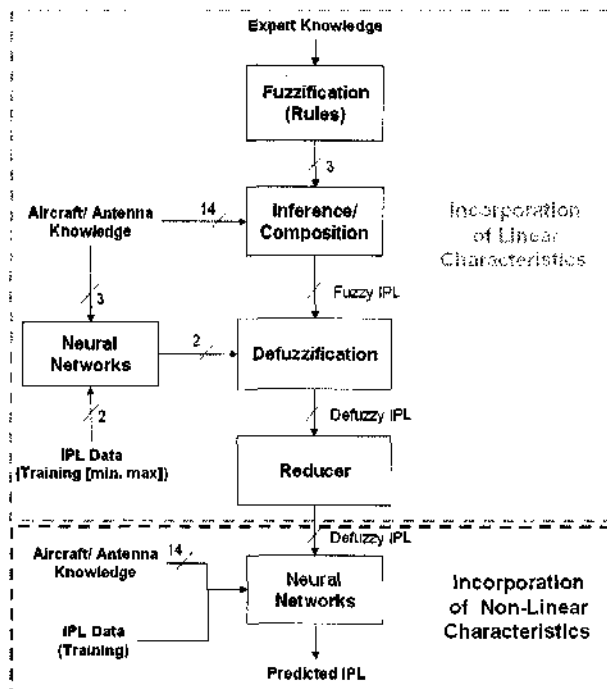


Figure 66. Detailed System Architecture for Neuro Fuzzy Model.

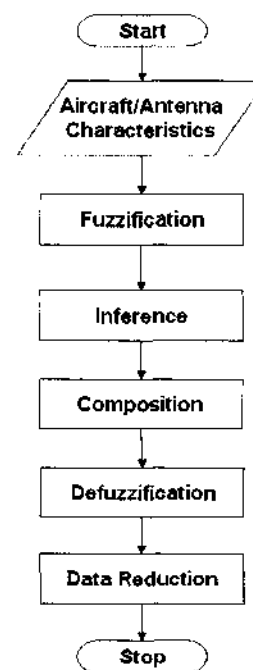


Figure 67. Flowchart for Linear Module of NFM.

3.2.3.1 Distance Calculations for Fuzzification

As mentioned earlier, IPL patterns are heavily dependent on the location of the doors, windows and aircraft antennas. Therefore, before initiating the modeling process, the distance and angle calculations were performed to locate the doors, windows and aircraft antenna systems relative to each other. In this module, aircraft characteristics (summarized in Table 4) were used as inputs to calculate distances and angles of each aircraft window to doors and antenna locations. The calculations that needed to be performed included: distances from each window to all exits (main and emergency exits), distances from all windows to antenna system of concern, angle from all windows to the antenna system of concern.

Table 4. Aircraft Characteristics for B737, B757, A319 and A320.

Features	B737	B757	A319	A320
Aircraft Length (cm)	2954	4697	3383	3750
Number of Windows	33	53	32	40
Number of Exits	2	3	2	2
Exit 1 location	491	580	767	780
Exit 2 location	2333	1400	2810	3050
Exit 3 location	2333	4127	2810	3050
Number of E. Exits	1	2	1	2
Emergency Exit 1 loc.	1250	2036	1604	1002
Emergency Exit 2 loc.	1250	2080	1604	1709
Aircraft system loc. (x)	200 → 2900	200 → 4600	200 → 3383	200 → 3750
Aircraft system loc. (y)	0 → 812.5	-200.5 → 931.5	-206.8 → +206.8	-206.8 → +206.8
Op. freq. (start, MHz)	108 → 1080	108 → 1565	108 → 1565	108 → 1565
Op. freq. (stop, MHz)	118 → 1100	118 → 1585	118 → 1585	118 → 1585
System's dominant pol.	H (0) or V (1)	H (0) or V (1)	H (0) or V (1)	H (0) or V (1)

The four aircraft of concern vary in length and, therefore, in the number of windows. For computational feasibility and speed, it was convenient to make uniform or identical. Instead of discarding data from larger aircraft to equate number of windows to smaller aircraft, data padding was utilized. B757 had the most number of windows (53). Therefore, all other aircraft were padded to equate to 53 windows each. Padding was performed by concatenation of the IPL value at the last window, $53-n$ times, where n equals the number of windows for the aircraft of concern. For example, A320 has 40 windows, so the IPL value at window number 40 was concatenated 13 times ($53-40$) for imaginary window numbers 41 to 53.

Before proceeding with any calculations, the location of each window needed to be determined in centimeters (cm). The locations of windows were determined by fitting the "number of windows" between the first and last exit locations for the aircraft of concern. In B737, for example, 33 windows needed to fit between exit 1 and exit 2, which were at 491 cm and 2333 cm, respectively.

$$win_gap = \frac{dist_exit_3 - dist_exit_1}{num_win + 1} \quad (1)$$

$$dist_win(i_{i=1:num_win}) = dist_exit_1 + i_{i=1:num_win} \times win_gap \quad (2)$$

In equation (1), win_gap represented the gap between the windows, $dist_exit_n$ is the distance from the measurement position to exit n and num_win is the total number of windows in the aircraft of concern. In equation (2), $dist_win$ is the distance in centimeter for each window relative to the front of the aircraft, i represents the window number and loops from window number 1 to the total number of windows, num_win .

The window gaps for the “imaginary” padded windows were determined by using the last window location of B757 and the last exit on the aircraft of concern. The calculation of distance from windows to exit locations required a linear subtraction between the locations of each window and exit of interest. For example, the distance from the m^{th} window to the n^{th} exit ($dist_win2exit_{m,n}$) could be calculated as follows:

$$dist_win2exit_{m,n} = |dist_win_m - dist_exit_n| \quad (3)$$

Next, distance from windows to antenna locations needed to be calculated. Previous modeling techniques [48, 50] have used rectangular fuselage shapes for easier computations; however a more precise circular fuselage was used in this modeling scheme. Electromagnetic waves creep along the surface of a metallic fuselage, therefore, following a circular/elliptical path toward the antenna system of concern [65]. The most computationally effective method to calculate the distance for the wave to creep from the window to the antenna of interest was to use the perimeter of an ellipse. A cylindrical fuselage, when traced at an angle, forms a cylinder. A better description is included in Figure 68.

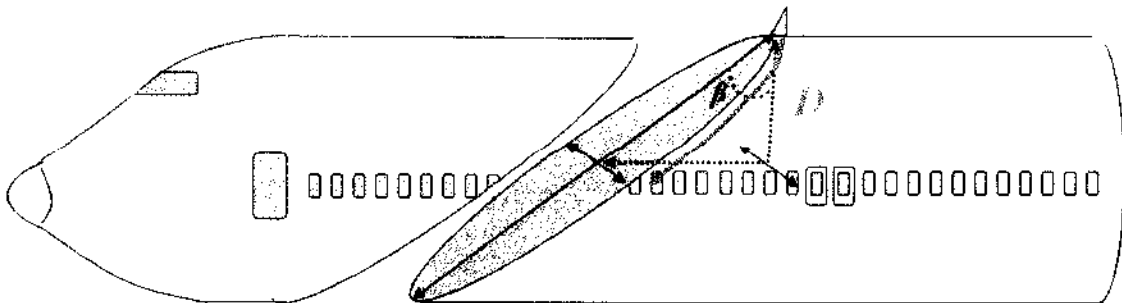


Figure 68. Distance Calculations from Window to Antenna, Fuselage Mounted.

To calculate the distance from a window to an antenna on top or bottom of the fuselage, the perimeter of the ellipse (magenta) needs to be calculated for a quarter path (green arrow). The minor axis (shown to be shorter, going into the page) represents the radius of the aircraft and cuts through the window at which the distance needs to be calculated, while the major axis (shown to be longer, from the center of the cabin to the antenna) increases or decreases based on the angle between the window and antenna. A quarter of the perimeter (in green) was calculated using the Ramanujan I perimeter formula of an ellipse [66]:

$$D = \frac{1}{4} \pi \left[3(a+b) - \sqrt{(3a+b)(a+3b)} \right] \quad (4)$$

Here D represents the calculated distance from the aircraft antenna to test window; while a and b are major and minor axis (respectively) of the ellipse. The angle, β in Figure 68 will be discussed later. For the systems installed on the top or bottom of the cylindrical fuselage (i.e. not in nose or tail), the minor axis, b , is simply the radius of the aircraft. The major axis, a , on the other hand needs to be calculated at every window location. Looking at Figure 68 again, the major axis, a , is approximately the hypotenuse of aircraft's radius and the distance between the test window and the window underneath the antenna location. Therefore, a can be calculated as follows, where win_{test} is the location of test window with respect to the x-axis, in cm, and $win_{antenna}$ is the location of the window underneath the location of the antenna.

$$a = \sqrt{r^2 + (win_{test} - win_{antenna})^2} \quad (5)$$

The calculation of distance between window and antenna is relatively easier and more accurate for systems mounted on the cylindrical fuselage; however, for systems mounted on nose or tail of the aircraft, more approximate methods need to be used. Figure 69 shows calculation of distance from a window location to antenna mounted in the nose. Again, the distance, D , will be calculated using a quarter of the perimeter of the ellipse. Due to a limited 2-dimensional drawing, it is more difficult to visualize an elliptical fitting on the aircraft for a nose-mounted system. Although the ellipse is shown to be slightly at a positive angle, in reality, it should be parallel to the horizon. Due to cargo bays at the bottom of the fuselage, the windows in the aircraft are not exactly in the center of the fuselage; however, the details of exact window locations relative to the y-

axis were not known in time. If the windows were modeled to be slightly higher than the center of the fuselage, then the slight positive tilt in the ellipse would be accurate.

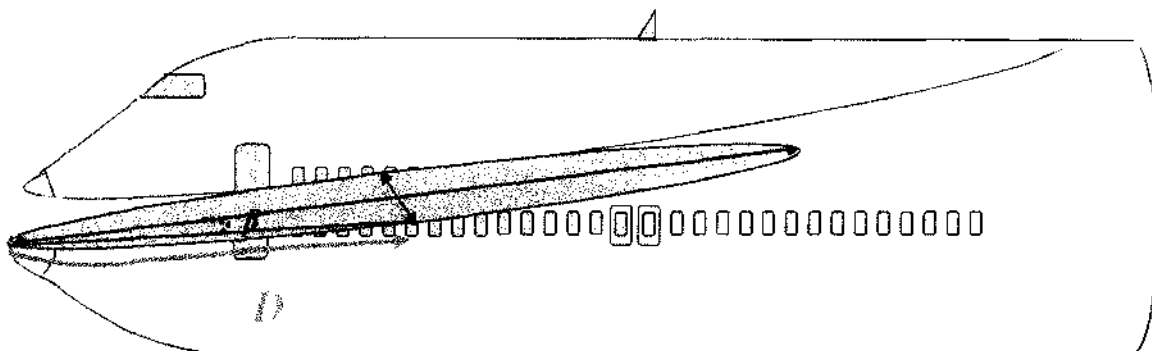


Figure 69. Distance Calculations from Window to Antenna, Nose Mounted.

In the simple assumption of windows being in the center of the fuselage, the minor axis, b , of the ellipse will again be the radius of the aircraft. The major axis, a , will be the distance from the nose of the aircraft to the tested window:

$$a = |win_{test} - win_{antenna}| \quad (6)$$

The calculation of distance using an ellipse for nose-mounted systems will produce approximately accurate results for windows closer to the nose of the aircraft; however, for the windows in the rear, the major axis of the ellipse will need to be elongated while the minor axis (radius of the aircraft) will remain the same. The elongated ellipse will not trace the nose of the aircraft as well as a wider ellipse and will therefore, introduce errors. These errors for the rear windows are not of a concern for this application since the pathloss patterns for nose mounted systems only affect the windows closest to the first exit of the aircraft, and not those near the rear.

Lastly, Figure 70 shows the needed calculations to attain distance from a window to an aircraft system mounted on the tail of the aircraft. In the CAD drawings of B737, B757, A319 and A320, it can be observed that the last exit door of the aircraft is almost always under the beginning of the tail slope (as depicted in Figure 62). Therefore, the distance from a test window to the tip of the tail is the summation of D_1 and D_2 . D_1 is calculated using the same methodology of how distance from test window to antennas mounted on the top or bottom of the fuselage is attained. This time; however, a

“temporary” antenna is placed on top of the last exit of the aircraft. Therefore, b is still the radius of the aircraft while, the major axis, a , is now:

$$a = \sqrt{r^2 + (win_{test} - win_{exit_3})^2} \quad (7)$$

Therefore, D_1 is:

$$D_1 = \frac{1}{4} \pi \left[3(a+b) - \sqrt{(3a+b)(a+3b)} \right] \quad (8)$$

D_2 is the hypotenuse of the tail, calculated by taking the square root of the sum of tail's height and the distance between the antenna location and the last exit. Recall that system's height, or the y-axis measurements, reported in Table 4 assume that the axis ($y=0$) is at the centerline of the fuselage. Therefore, the height reported for systems mounted on the tail not only includes actual height of the tail, but also includes radius of the aircraft (centerline, $y=0$, to top of the fuselage). So D_2 can be calculated as follows:

$$D_2 = \sqrt{(antenna_x - win_{exit_3})^2 + (r - antenna_y)^2} \quad (9)$$

In equation 9, $antenna_x$ is the location of the antenna along of the fuselage in the x direction (in cm), while $antenna_y$ is the location of the antenna in the y-axis (in cm) relative to the nose of the aircraft. Finally, the distance from test window to the antenna is the summation of D_1 and D_2 .

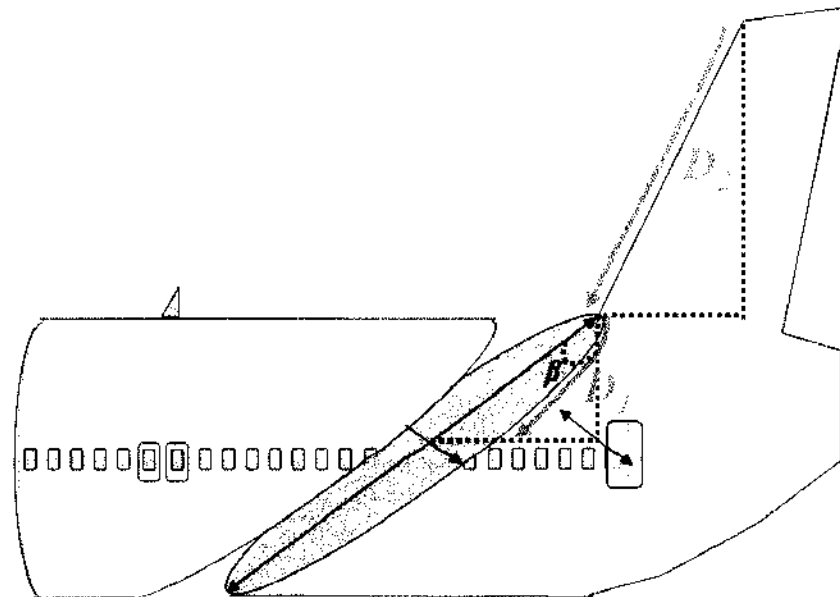


Figure 70. Distance Calculations from Window to Antenna, Tail Mounted.

After calculating the distances, the last calculations of concern are the angles between the aircraft systems and the test window. These angles will be used to make predictions on the effect of polarization on pathloss values. For example, pathloss is lowest for vertically polarized systems immediately below the installed system (small angle); while systems with horizontal polarizations couple better at larger distances. Please observe the β 's pointed out in Figure 68, Figure 69 and Figure 70. The β in Figure 68 and Figure 70 are calculated using same technique; therefore, only two β 's, instead of three, will be calculated: one for systems mounted on the nose, while the other for systems mounted on either the fuselage, or the tail of the aircraft.

For systems mounted on the fuselage or tail of the system, β can be calculated as follows using simple trigonometry:

$$\beta = \tan^{-1} \left(\frac{|win_{test} - win_{antenna}|}{r} \right) \quad (10)$$

For systems mounted on the nose of the aircraft, β can be calculated as follows:

$$\beta = \tan^{-1} \left(\frac{r}{|win_{test} - win_{antenna}|} \right) \quad (11)$$

Using the distances and angles calculated for all windows, relative to all systems, the next step is to create and then apply the fuzzy rules.

3.2.3.2 Fuzzification: Generation of Rules

After observing the pathloss patterns presented in chapter 2, three main rules could be devised for Fuzzification. The first rule relates pathloss patterns from windows relative to the distance of the test window to the aircraft exits. The second rule applies expert knowledge from observing patterns due to the location of the aircraft antenna relative to the test window. The final rule takes into account the polarization of the tested system and how it affects the pathloss patterns. Before going over the rules, it is important to understand the difference between “pathloss” and “coupling” and how these two wordings are related. Coupling is simply the inverse of pathloss; it is obtained by a simple negation of pathloss values. For example, if a pathloss value is 65 dB, the relative coupling value will be -65 dB. A low pathloss value means that the loss of power between transmitting and receiving station was low (i.e. amount of power radiated was close to the amount of power received). A high pathloss on the other hand, implies high

loss of power between radiating and receiving stations (i.e. amount of power radiated was much more than the power actually received). The concept of coupling is simply the inverse, where a low coupling means more power loss, while a high coupling means less power loss between the transmitting and receiving stations.

The fuzzy rules were created using coupling values, instead of pathloss, because during composition, only the use of coupling values show the needed additive effect. For example, if we were to use pathloss, instead of coupling, a system located close to the first exit of the aircraft would show low (0) pathloss near the front of the aircraft, and high (1) pathloss near the end. This same system would show low (0) pathloss near the antenna location (closest to first exit), and high (1) pathloss as the distance increases. Just using these two rules, composition, or linear addition, of them will produce low (0+0) pathloss for the front of the aircraft and a high (1+1) pathloss for the rear of the aircraft. The value of 0 is not as descriptive, in fact, it does not even ensure that pathloss was low in that region due to two rules, instead of one. Therefore, fuzzy rules were made using the concept of coupling. For the same example, coupling would be high (1) in the front of the aircraft (due to the distance from exit and antenna), and low (0) in the rear of the aircraft. The summation of rules for composition will now yield very high (1+1) coupling for the front of the aircraft and low (0) coupling for the rear.

The first rule encapsulated the effect on coupling based on the location of aircraft exits relative to the test window. As observed in the pathloss patterns in chapter 2, both the emergency exits, and the major aircraft exits played an important role in pattern prediction. Two separate rules were generated for main exits and emergency exits. Main aircraft exits were found to be leaking (high coupling) and the trend would taper off slowly. Emergency exits were found to be leaky at precisely their locations, with a sharp decreasing trend in coupling as the distance from the emergency exit was increased. Figure 71 and Figure 72 show the rules for main and emergency exits, respectively. X-axis shows the distance in cm, while the y-axis shows fuzzified coupling values from 0 to 1, where 1 is high coupling and 0 is low coupling. The distances were determined by first calculating the gaps between the windows, and then applying the fact that for main doors, the highest coupling was found around 2 window locations near the exit, and the coupling tapered down to zero as the distance increased to 5 windows. For emergency

exits, high coupling values were noticed at the emergency exit and around the first surrounding windows (left and right direction). These coupling levels dropped to zero after about 3 windows.

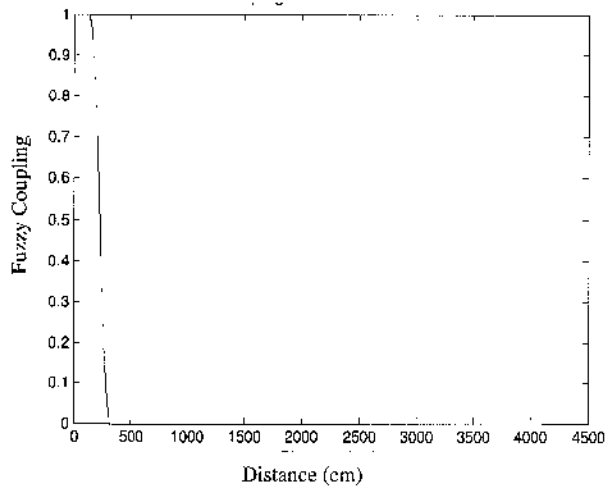


Figure 71. Fuzzy Rule 1a: Coupling with respect to location of Main Exits.

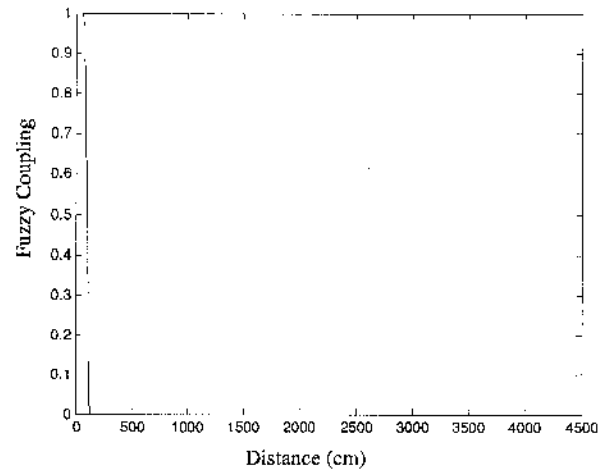


Figure 72. Fuzzy Rule 1b: Coupling with respect to location of Emergency Exits.

These rules were generated using MATLAB's Z-shaped built-in membership function (zmf), with the following properties:

$$\left\{ \begin{array}{ll} 1, & x \leq a \\ 1 - 2 \left(\frac{x-a}{b-a} \right)^2, & a \leq x \leq \frac{a+b}{2} \\ 2 \left(b - \frac{x}{b-a} \right)^2, & \frac{a+b}{2} \leq x \leq b \\ 0, & x \geq b \end{array} \right. \quad (12)$$

Here, a and b are distance values mentioned in reference to the number of windows.

The second rule takes into account the effect of coupling based on the location of the antenna system of concern. This rule needed to be split into three sub-rules for systems mounted on the nose, fuselage, and tail, respectively. Figure 73 shows the fuzzy rule created for systems mounted on the nose of the aircraft using MATLAB's ZMF. The coupling levels are high (1) near the first two windows of the aircraft, and the levels decrease to zero after four windows. The distance from the nose to the first exit of the aircraft is appended to the window locations and is thus taken into consideration. Figure 74 shows the coupling levels relative to antenna systems mounted on the main cylindrical fuselage of the system. For fuselage mounted systems, coupling patterns were observed

to be high near the first window of the mounting location. The coupling levels are observed to taper off to zero after three windows. Rule 2b is also created using MATLAB's ZMF. Finally, Figure 75 shows the coupling levels relative to antennas mounted on the tail of the aircraft. The tail mounted systems (all horizontally polarized) were interesting because they showed no coupling near the tail of the aircraft, but showed more coupling effects near the emergency exits, or the wings of the aircraft. So as seen in the rule, low coupling is observed near the location of the antenna, then coupling increases from zero at the first window to maximum (1) near 7th to 12th windows, and then tapers back down to zero coupling after 16th window. Rule 2c was implemented using MATLAB's Pi-shaped built-in membership function (PIMF), instead of ZMF.

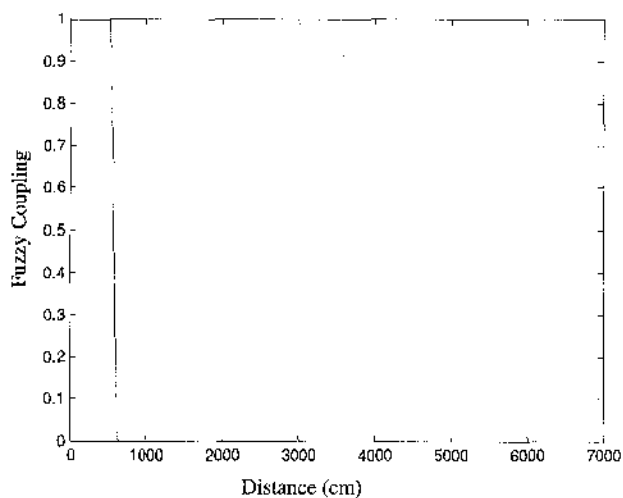


Figure 73. Fuzzy Rule 2a: Coupling with respect to location of Antenna, nose mounted.

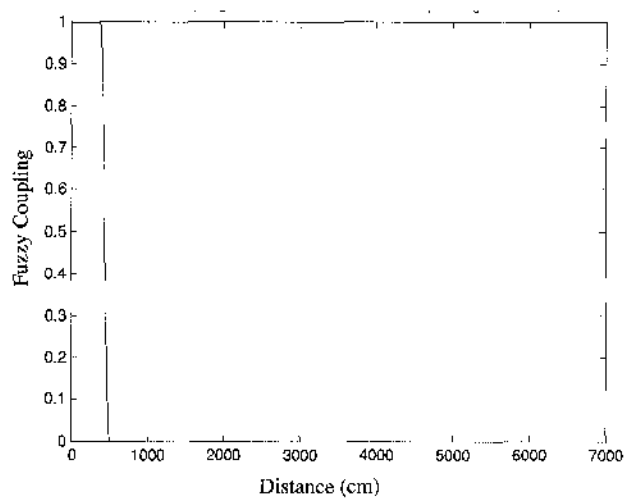


Figure 74. Fuzzy Rule 2b: Coupling with respect to location of Antenna, fuselage mounted.

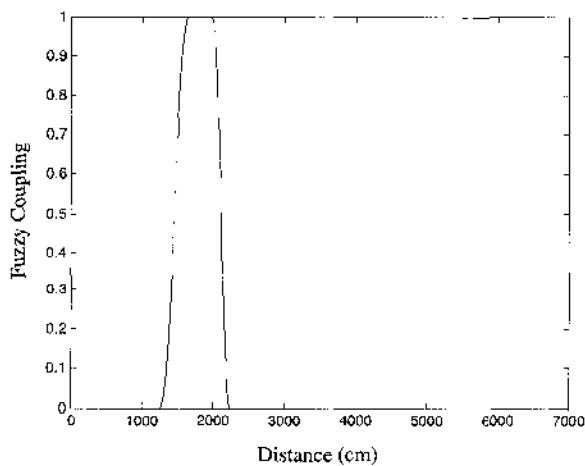


Figure 75. Fuzzy Rule 2c: Coupling with respect to location of Antenna, tail mounted.

The last fuzzy rule was made with respect to the polarization of the system of interest. It was observed that vertical polarized systems tapered off in coupling levels quickly, while horizontally polarized systems decreased in coupling more slowly. Figure 68, Figure 69 and Figure 70 refer to the original schematics where the angle, β , was not previously discussed. For the systems mounted on the nose of the system, with vertical polarization (non-existent case), there would be zero coupling throughout the aircraft. For the systems mounted on the nose of the aircraft with horizontal polarization (see Figure 69), the coupling would be high when the angle, β , will be maximum, and will decrease, when the angle decreases for the rear windows (i.e. major axis of the ellipse increases). Therefore, in the rule for nose-mounted horizontally polarized systems (see Figure 76), coupling is predicted to be maximum at the angle of 0 radians, and tapers off to 0 after $\pi/4$ radians. The angles were multiplied by a constant value of 100 due to MATLAB limitations; therefore, the x-axis in the rule is between 0 and ~160, instead of 0 to $\pi/2$ or 1.57.

For systems mounted on the fuselage or tail of the aircraft with dominant vertical polarization, the coupling was maximal at angle, β of 0, and decreased to zero coupling after an angle of $\pi/4$ radians (see Figure 77). Finally, for the systems mounted on the fuselage or tail of the aircraft with dominant horizontal polarization, coupling was observed to be the least when then angle, β , was close to 0. However, the coupling increased as β increased from $\pi/4$ to $\pi/2$ (see Figure 78). For a tail mounted system, this rule may predict that the coupling is highest at the front of the aircraft (based on highest β), however, the second rule relative to the distance from antenna, will assist in tapering the coupling down to zero as the distance from the antenna increased.

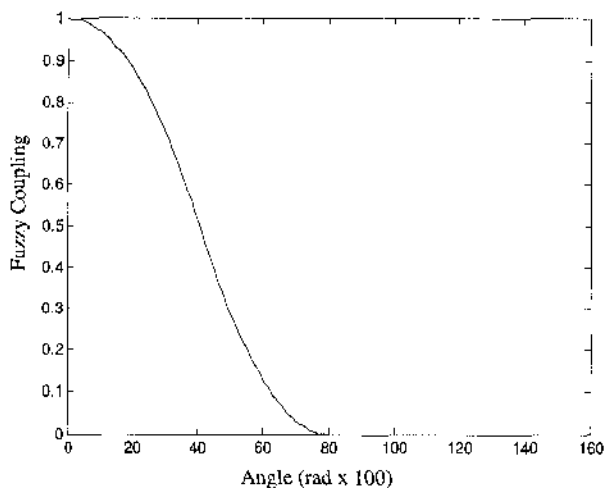


Figure 76. Fuzzy Rule 3a: Coupling with respect to Antenna Polarization, nose mounted, horizontal.

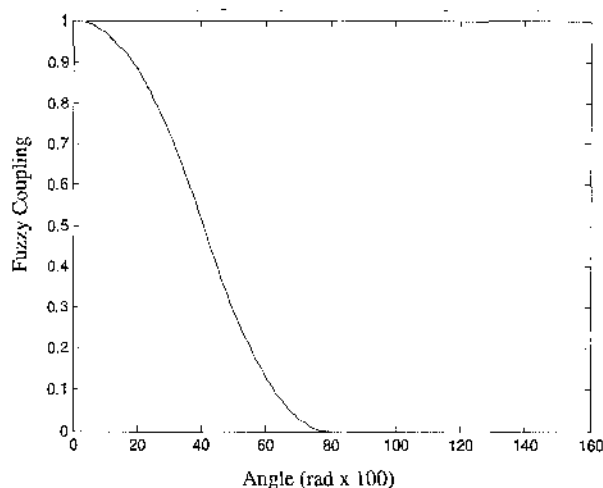


Figure 77. Fuzzy Rule 3b: Coupling with respect to Antenna Polarization, tail/fuselage mounted, vertical.

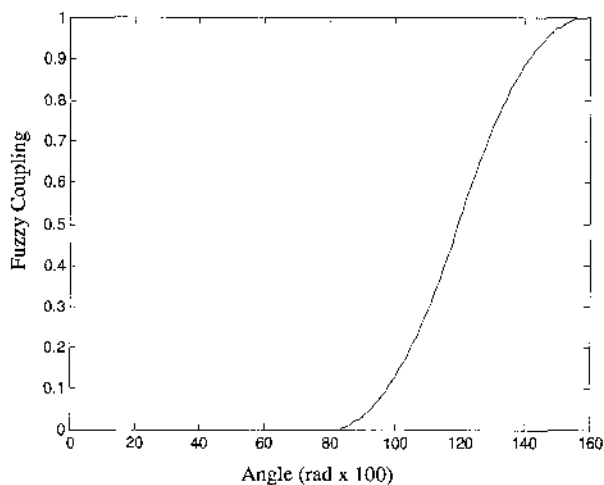


Figure 78. Fuzzy Rule 3c: Coupling with respect to Antenna Polarization, tail/fuselage mounted, horizontal.

3.2.3.3 Inference: Application of Rules on Calculations

The fuzzy rules, created in the previous section, need to be developed only once. Then the process of inference is used to send the calculated distances (from section 3.2.3.1) into the fuzzy rules. Fuzzified IPL values are assigned based on the distance or angle of the input. For example, Figure 79 shows how inference takes place on fuzzy rule 3, which predicts coupling values based on the angle of the antenna, mounted on the fuselage or tail in horizontal polarization). If the angle is 1.2 radians (or 120, when multiplied by a factor of 100), then the coupling value is determined to be 0.5. If the

angle is 1.4 radians, then the coupling value is about 0.87 etc. Using this technique, the fuzzified coupling values are determined for all distances and angles calculated in the previous sections.

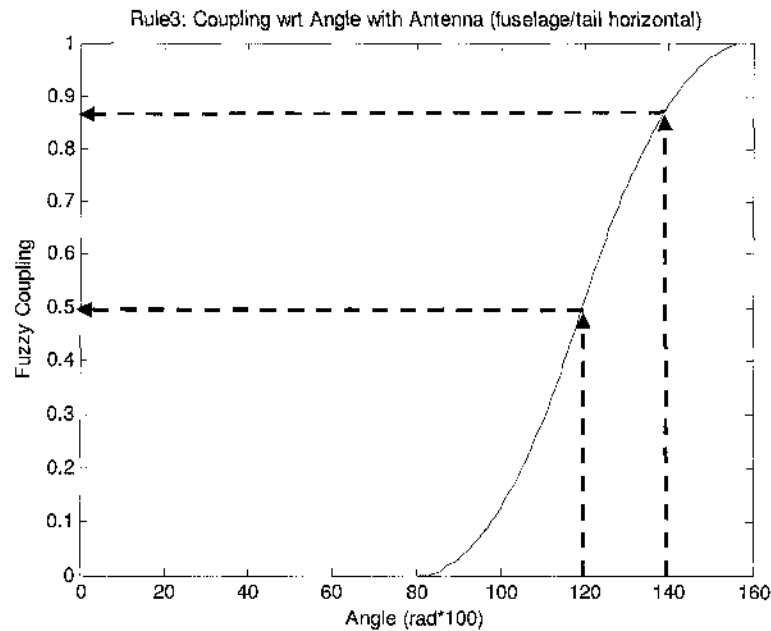


Figure 79. Demonstration of Fuzzy Inference.

3.2.3.4 Composition: Summation of Fuzzified Outputs

Composition is a simple step in fuzzy logic in which the fuzzified outputs from inference for each rule are added linearly. This linear addition incorporates the effects of all rules into a final fuzzy coupling pattern. In this step, the fuzzified coupling levels are then inverted for pathloss representation (for easier comparison with the measured IPL data presented in Chapter 2). Pathloss representation will be used in the remaining procedure for pathloss prediction.

3.2.3.5 Defuzzification: Conversion from Fuzzified to Crisp Outputs

During defuzzification, the fuzzified IPL values (ranging between 0 and 4) are traced to actual (crisp) IPL values (ranging between 45 dB to 90 dB). In previous work [23], defuzzification was performed using linear mapping of the same minimum and maximum values for all systems. This caused a limitation of the model because as observed in the real data, every system has a particular range of minimum and maximum IPL value and cannot be mapped to any static minimum and maximum values.

Therefore, in the newly proposed NFM, a small neural network was utilized to learn the minimum and maximum IPL values from training data to be used for defuzzification.

MATLAB's Neural Network library was utilized to implement the neural network structure [67]. A three node input layer, a five node hidden layer and a two node output layer was created using the feed forward algorithm (see Appendix C for more technical details on Neural networks). Figure 80 shows the basic neural network structure used to predict the minimum and maximum IPL values for the system of interest. Log-sigmoid transfer functions were used in both hidden and output layer to capture the non-linear characteristics of the IPL data. Tan-sigmoid was not used because the input data (aircraft length, start and stop frequencies) being sent through the neural networks is always positive. The output minimum and maximum pathloss values are also positive.

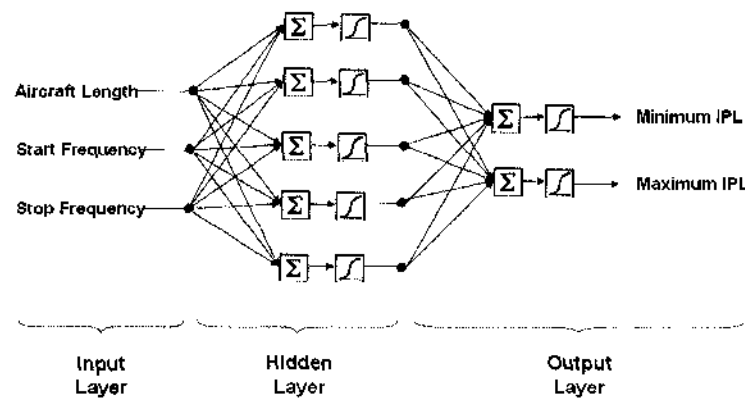


Figure 80. NN for prediction of Minimum and Maximum IPL values.

In the beginning of the simulation, measured IPL data was divided into training and test data. In real world simulation, there will only be training data, and no test data to compare predictions with. For each aircraft's particular system, three characteristics of the training data were sent through the input layer. Without any previous training or knowledge of the data, neural network predicted random minimum and maximum IPL values. These predicted IPL values were then compared to actual minimum and maximum IPL values in the training data and back propagation was used to update the weight matrix in each layer of the neural network. Then the remaining sets of training data was sent through the neural networks, with the weights being updated at every iteration of learning.

After all training data was passed through; the aircraft characteristics for the system to be tested were passed through. Using the trained weights, the neural networks

predicted the minimum and maximum IPL values for the test system. The predicted IPL values were used to determine the slope and intercept values for a linear transfer equation. This transfer function was used to defuzzy the fuzzy IPL values from section 3.2.3.3 into crisp IPL values in dB.

3.2.3.6 Data Reduction

One major objective of this new modeling algorithm was to obtain a computationally efficient design. The output of the defuzzification module yielded in arrays of 53 IPL values for every system of all four aircraft. Although all 53 values could be sent to the next module, neural networks, for incorporation of non-linear patterns, however, for efficiency purposes, only every 5th value was sent to the next module. The number 5 was selected because most exits fell around this number, i.e. emergency exit at window 16 for B737 etc. (please see results in next chapter for more detail). Therefore, every 5th window of all aircraft contained some useful information of the IPL pattern.

3.2.4 Neuro-Fuzzy Model's Non-linear IPL predictions

Defuzzified data from every 5th window, along with the original 14 aircraft and antenna characteristics were available to determine the non-linear patterns in IPL prediction. Every 5th window in a 53 window airplane (padded) yielded 11 IPL measurements. So in total, 11 and 14, or 25 inputs were available to determine the IPL pattern on a needed aircraft's selected system. A neural network with 25 nodes in the input layer, 30 nodes in the hidden layer and 26 nodes in the output layer was proposed. Tan-sigmoid transfer functions were used between the hidden and output layer to incorporate the non-linear characteristics in the data. Unlike log-sigmoid function, tan-sigmoid function takes both positive and negative values into consideration when learning. The 25 inputs from all training data were first passed through the neural networks to update the weights. Then the 25 inputs for the test data were sent in and the predicted IPL pattern was acquired.

CHAPTER 4

RESULTS AND EVALUATION OF NFIS EMI MODEL

The modulated NFM was successfully implemented using MATLAB [67]. The collected IPL data was first tabulated in EXCEL and calibrated using the measured correction factors. Aircraft systems to be modeled were selected as testing data, while other data was used as training data. The selected data was sent through the linear and non-linear sections of NFM. The mean of predicted outputs for the selected systems deviated from true output by 1 dB and 3 dB, respectively. Although further improvements are suggested, the model was successful in achieving the most accurate IPL predictions relative to real-world data in a timely efficient manner. Detailed results are included in the following sections.

4.1 IPL Data Collection

Extensive IPL data was collected onboard B737, B757, A319 and A320 in 2002, 2004, 2005 and 2005, respectively. This data was measured under cooperative agreement between NASA Langley Research Center, Eagles Wings Inc., Delta Airlines and United Airlines. All measurements were obtained on in-service aircraft, made available for a few hours due to minor maintenance reasons. Data was successfully collected on GS, TCAS, VHF and LOC-L for B737; GS, LOC, TCAS-U, TCAS-L, ATC-U, ATC-L, DME-L, MB, DME-R, GPS-L, VHF-R, VHF-L, VHF-C and VOR for B757; GS, LOC, DME-L, VHF-L, ATC-B, ATC-T, VHF-R and VHF-C for A319; and GS, LOC, DME-L, VHF-L, ATC-T, ATC-B, GPS and VHF-C for A320. This data is available for further studies in Appendix D. To perform an IPL measurement, the team measured the RF power loss between the calibrated signal source and a spectrum analyzer, via the entire length of test cables plus the aircraft cable, plus the free space loss between the reference antenna and the aircraft antenna. To obtain a calibrated IPL measurement, test cable losses were measured separately by connecting the two ends of the test cables to the input and output of the spectrum analyzer, and subtracting this loss, in dB, from the raw measurement. These calibration factors are also included in the Appendix and must be used with the tabulated raw data for final IPL measurements.

4.2 Training Data Selection

Although all collected IPL data was used to train the NFM, only two systems from an aircraft were selected as test sets to be modeled. Previous work [50, 56] showed limitations in modeling systems from both low and high frequencies. Therefore, a system was selected from the low and high end of the frequency spectrum to prove NFM's ability to predict pathloss for a full frequency spectrum of concern. Table 5 shows the availability of measured data for each system on the four aircraft along with their operating frequencies. The data available on each aircraft is marked with (⊗).

Table 5. Available IPL Data.

Aircraft System	Operating Frequency (MHz)	B737	B757	A319	A320
MB	75		⊗		
LOC-L	108.1 – 111.95	⊗	⊗	⊗	⊗
VOR	108 – 117.95		⊗		
VHF-L	118 – 137	⊗	⊗	⊗	⊗
VHF-R	118 – 137		⊗	⊗	
VHF-C	118 – 137		⊗	⊗	⊗
GS	328.6 – 335.4	⊗	⊗	⊗	⊗
DME-L	962 – 1213		⊗	⊗	⊗
DME-R	962 – 1213		⊗		
ATC-T/U	1030		⊗	⊗	⊗
ATC-B/L	1030		⊗	⊗	⊗
TCAS-U	1090	⊗	⊗		
TCAS-L	1090		⊗		
GPS	1575±2		⊗		⊗

It was desired to model the system with the greatest amount of pathloss data available on all aircraft. Only LOC-L, VHF-L and GS were measured on all four aircraft types. All three of these systems operate at low frequency. Out of the three, VHF-L was selected as the test system for comparability purposes with other models. No data was available on all four aircraft for systems operating at high frequency. The possible system options, where the data was at least collected on three out of four aircraft, were DME-L and ATC-T/U or ATC-B/L. DME-L was selected instead of ATC because its stop frequency is slightly higher than ATC's operating frequency. Also, the location of DME in B757 is different than that in A319 and A320 (mounted near the nose, vs. on the fuselage); therefore, it was interesting to observe the impact of location on pathloss prediction.

After selecting the system, the system's aircraft needed to be selected. The objective of this modeling was to predict coupling on a system without knowing the coupling patterns on *any* other system on the same aircraft. This objective shows the real-world application of this research, where it will be desired to model a particular system on a brand new aircraft type, without needing to take time-consuming measurements on it for *any* other system. Therefore, B757 was not a good aircraft to be used for testing purposes, because that would require that *none* of the measurements from B757 systems be included in training of the NFM causing too much loss of useful data. Between A319 and A320, A320 was selected due to its uniqueness in structure from B737, B757 as well as A319. A319 is very similar in structure to the B737, while the B757 and A320 are different and unique. In conclusion, the systems selected to be modeled were A320's VHF-L in the low frequency and A320's DME-L in the high frequency and none of A320 systems were used during training.

4.3 NFIS Model Results and Evaluation

Before training the model for prediction, the training data needs to be made uniform with each other. For example, data from all aircraft needed to be padded to fit the data length of the longest aircraft (B757, 53 windows). Then the locations of all windows relative to the length of the aircraft needed to be determined in cm. Figure 81 shows the padding and distance results relative to window locations for B737 data. The lower x-axis represents the number of windows in the data. Originally, B737 has 33 windows and is 2954 cm in length; however, as required, data padding was performed on each system of B737 to achieve a total length of 53 windows, or 4697 cm. The upper x-axis represents the locations of the windows in centimeters. For example, window number 20 is located at 2000 cm. The y-axis represents the pathloss values in dB. Figure 82, Figure 83 and Figure 84 show the padding and distance calculations for B757, A319 and A320, respectively. In real-world simulation, on an aircraft with unknown pathloss values, similar padding and distance calculations would be performed based on the number of windows and the length and exit location characteristics of the test aircraft.

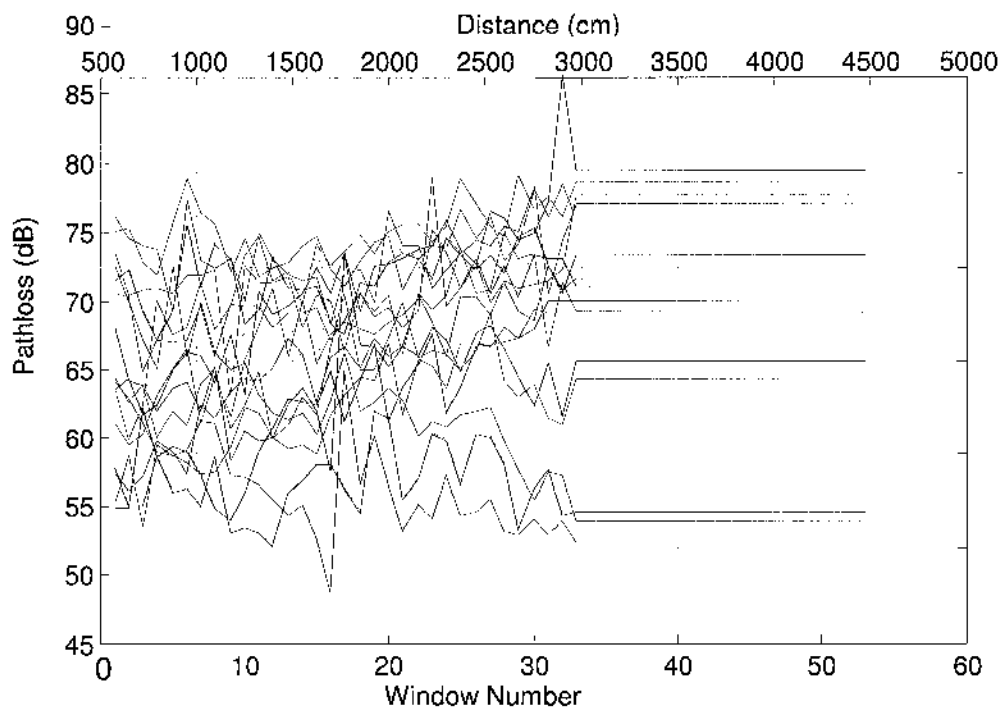


Figure 81. Padding and Mapping of Windows to Distance (cm) (B737).

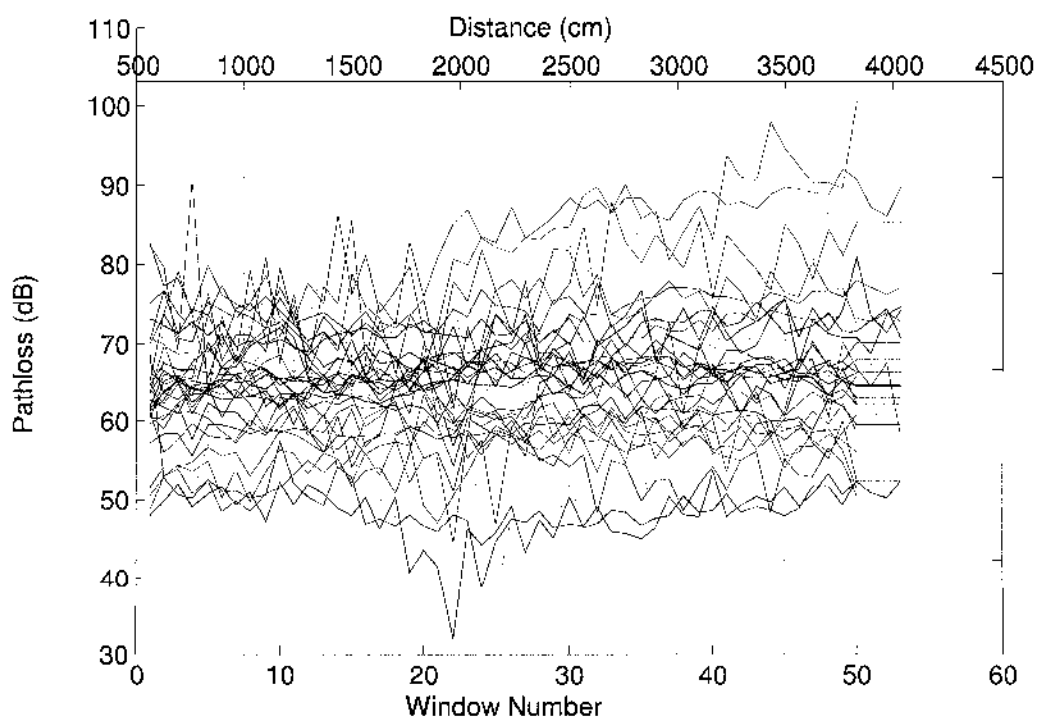


Figure 82. Padding and Mapping of Windows to Distance (cm) (B757).

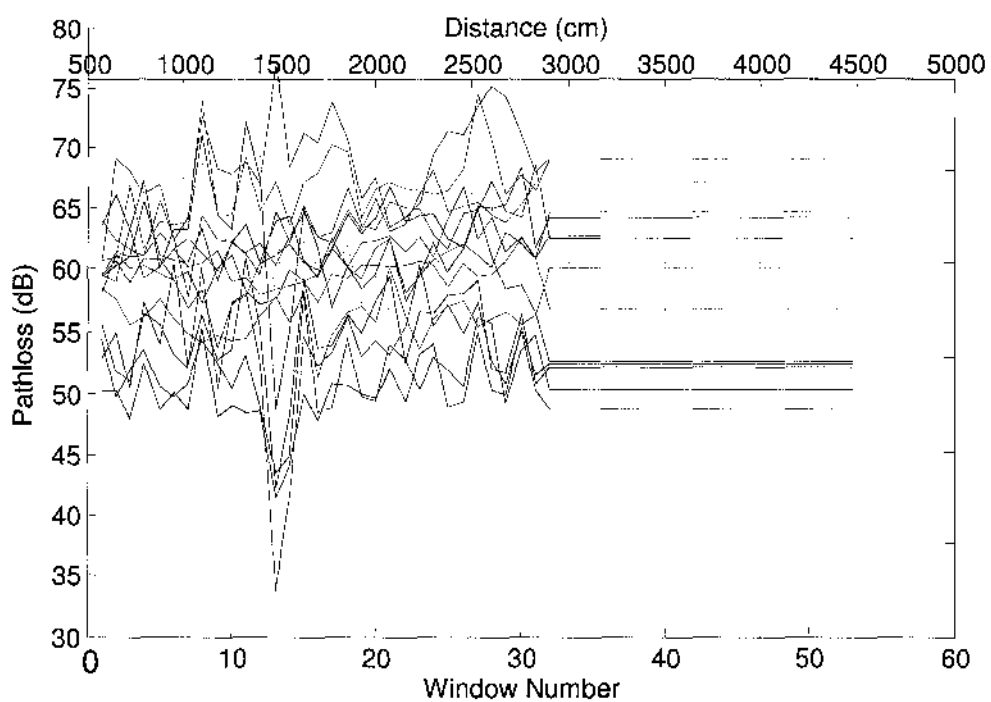


Figure 83. Padding and Mapping of Windows to Distance (cm) (A319).

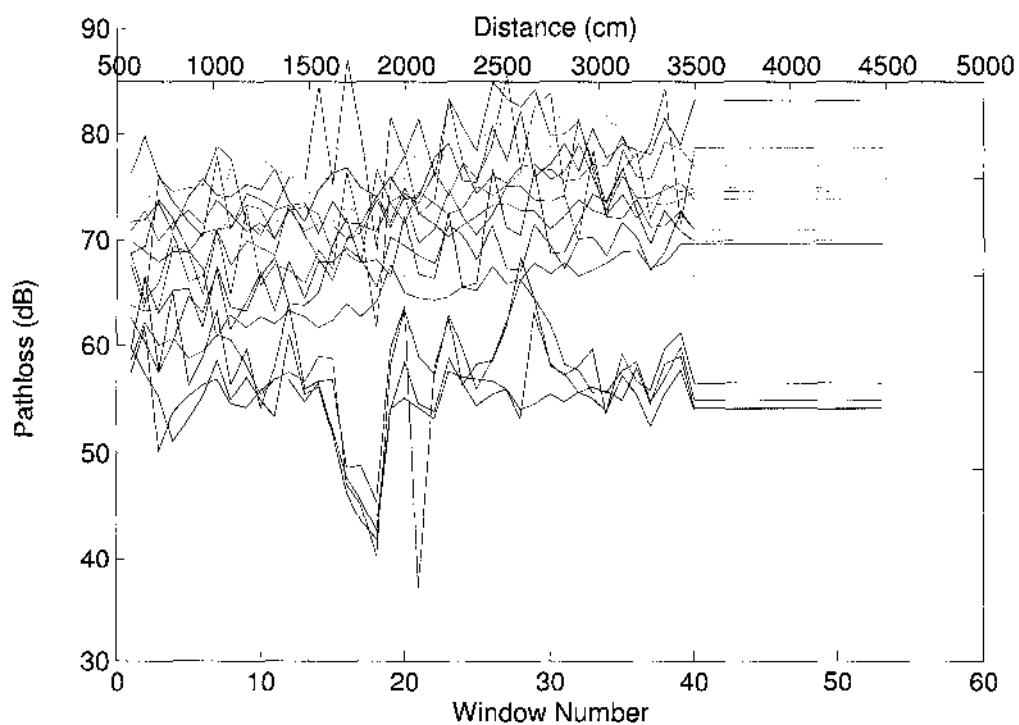


Figure 84. Padding and Mapping of Windows to Distance (cm) (A320).

Determining the locations of all windows relative to the front of the aircraft enabled proper calculations for distance and angle measurements, needed for fuzzy logic. The following two sections go over the step by step results for A320's VHF-L and DME-L.

4.3.1 IPL Prediction: A320 VHF-L

The 14 aircraft and antenna characteristics for A320, VHF-L were used to calculate the needed distances from the main exits, emergency exits, system's antenna as well as the angles from the system's antenna. In A320, VHF-L is located on top of the first main exit of the aircraft, between GPS and ATC-T. It is a vertically polarized system. Figure 85 shows the fuzzified pathloss pattern for VHF-L. Again, the x-axis represents the window locations, while the y-axis represents fuzzified pathloss value (not in dB). The model was able to successfully encapsulate the effect on pathloss due to main and emergency exits as well as show the increasing pathloss trend from front to aft of the aircraft, which was observed in real IPL data. This figure is obtained after the process of fuzzification, inference as well as composition.

Next, the process of defuzzification was applied to adjust the y-axis of Figure 85 from fuzzy IPL values to crisp IPL values which depict the real pathloss values more closely (in dB). For defuzzification, the three inputs (aircraft length, systems start and stop frequencies) were sent as inputs to neural networks for training. Only inputs from B737, B757 and A319 were used for training. Then the three characteristics for A320's VHF-L were sent as inputs to determine the minimum and maximum predicted IPL values for the system. Figure 86 shows the minimum and maximum pathloss values for actual and predicted IPL patterns. The results are remarkably similar and only vary by 1 and 2 dB between actual and predicted values.

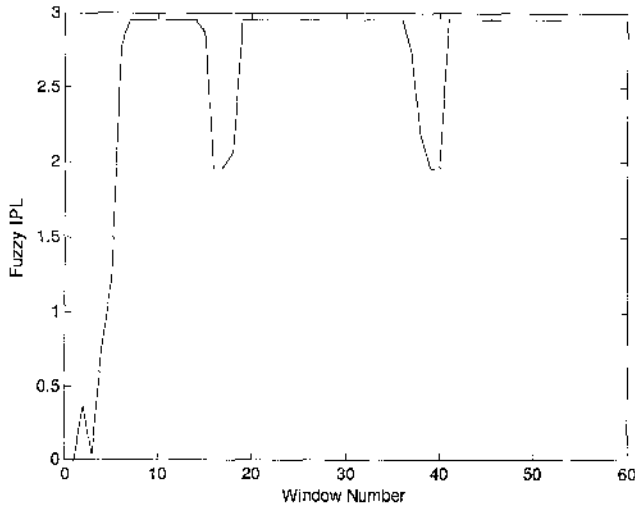


Figure 85. Fuzzified IPL Pattern for VHF-L (A320).

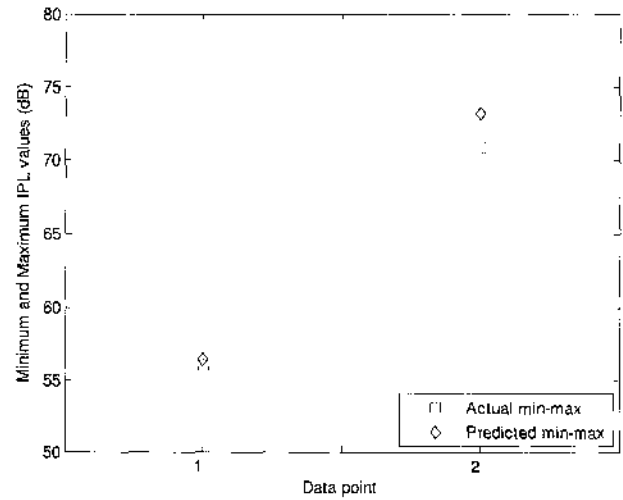


Figure 86. Minimum and Maximum IPL Prediction for VHF-L (A320).

Figure 87 shows the linear interpolation of the fuzzified IPL pattern into crisp values using the predicted minimum and maximum values. The actual IPL data is also plotted on the same graph. Although the overall pattern is not comparable, the fuzzy module is capable of successfully incorporating the effect of the first exit and the emergency exits (near windows 17 and 18) into the overall pattern. The effect of antenna location is also incorporated due to the most decreased predicted pathloss in the front of the aircraft, where VHF-L is mounted.

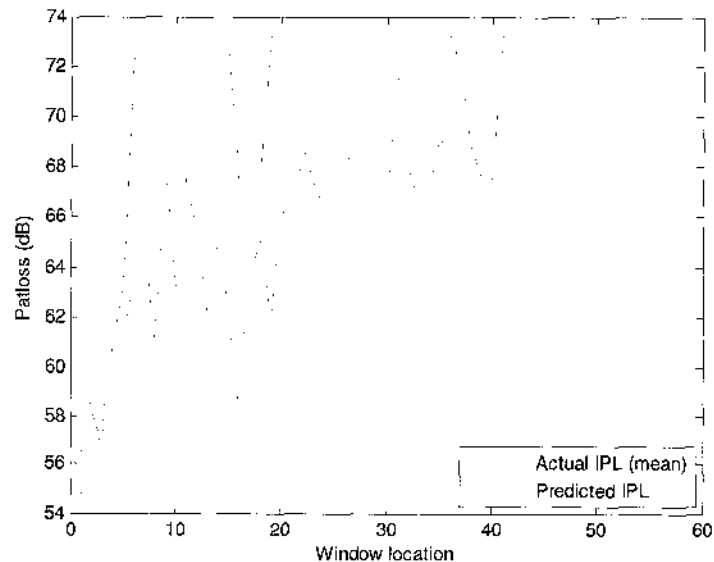


Figure 87. Defuzzified and Real IPL Pattern for VHF-L (A320).

The defuzzified pattern was then reduced (only recorded at every 5th window) and sent to the non-linear module of NFM. The original 14 characteristics of all aircraft systems were also sent to the non-linear module. Figure 88 shows the pathloss predictions for A320 VHF-L. IPL data from two actual trials of VHF-L calculations is reported in red, while the predicted IPL pattern for VHF-L is reported in blue. Although the overall IPL pattern until window 33 follows the correct increasing pathloss trend (with low pathlosses near the exits), the rear of the fuselage is very poorly predicted. Also, there is much variance in the overall data.

Figure 89 shows the actual versus predicted IPL data on a larger scale by including all training data used by NN before prediction. The training data is represented in green, the actual two trials for VHF-L are represented with dashed red lines, while the predicted IPL pattern for VHF-L is represented in a solid red line. The mean, variance, standard deviation and minimum pathloss values are also reported below the figure for both the mean of the real data as well as the predicted data. Although much variation existed in the previous figure, the overall means of real versus predicted data only vary by about 0.1 dB. The minimum IPL value predicted by neural networks is about 2.4 dB higher than the actual minimum value.

Finally, Figure 90 shows the actual VHF-L patterns (mean) for all four aircraft. As observed, although VHF-L measurements were present for B737 and B757, the system was installed in the middle of the fuselage, instead of the front, like A320 and A319. Therefore, the pathloss patterns from B737 and B757 was not as helpful for training purposes and the A320 predictions were probably made using the IPL pattern from A319 data for VHF-L. There is as much as dB difference in IPL values between A319 and A320 data in some locations. Therefore, overall, the neural networks did a very acceptable job in predicting the IPL pattern for VHF-L in A320, after learning the IPL patterns from systems installed on other aircraft types.

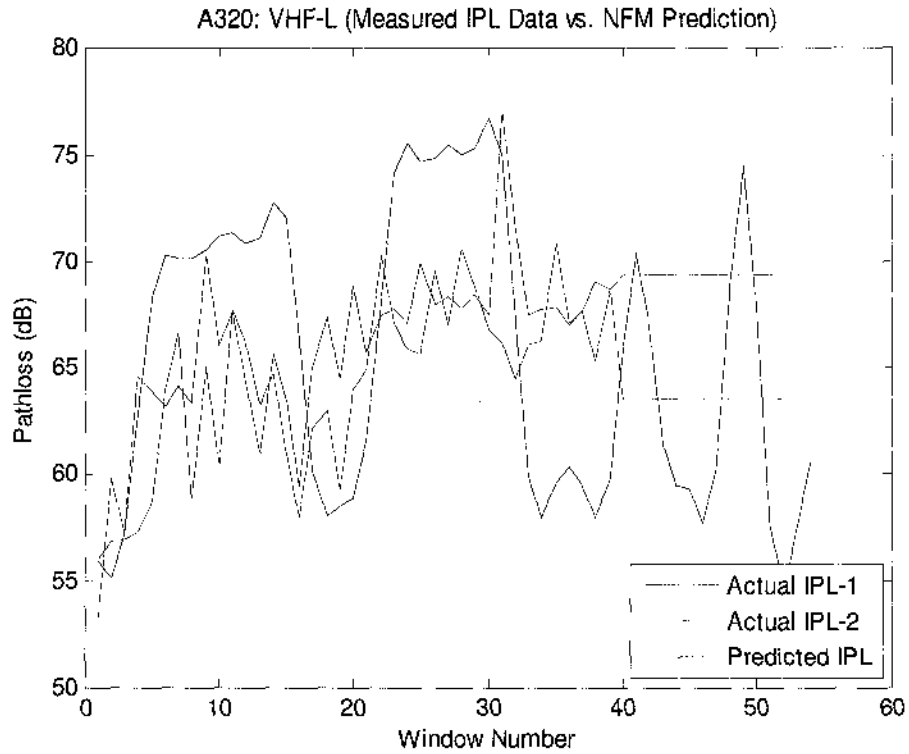


Figure 88. Actual vs. Predicted IPL Pattern for VHF-L (A320).

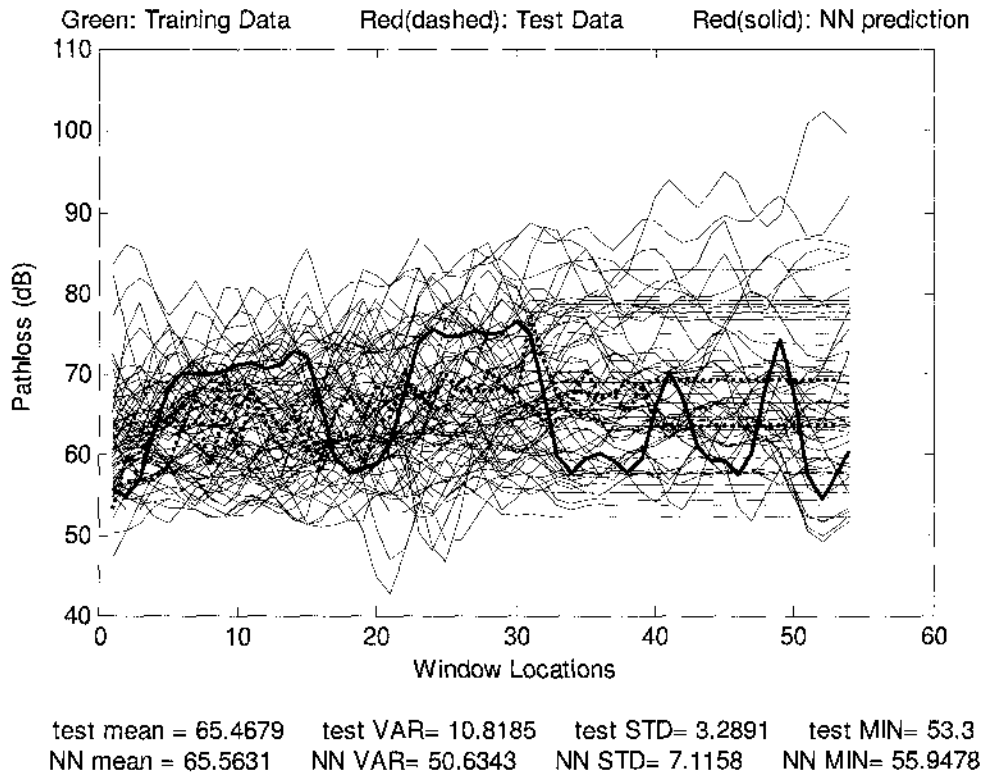


Figure 89. Actual, Predicted and Training Data for VHF-L (A320).

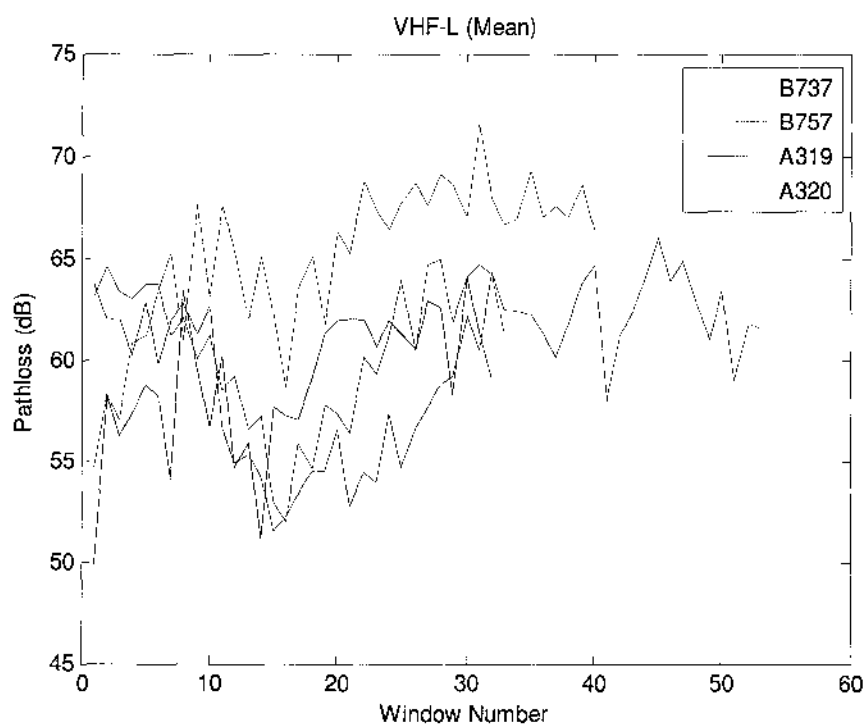


Figure 90. Mean IPL Patterns for VHF-L from all Aircraft (B737, B757, A319, A320).

4.3.2 IPL Prediction: A320 DME-L

In A320, DME-L is located on the bottom of the fuselage between the nose and the first main exit of the aircraft, between GS and ATC-B. It is a vertically polarized system. Figure 91 shows the fuzzified pathloss pattern for DME-L. The model was able to successfully encapsulate the effect on pathloss due to main and emergency exits as well as due to the location of the antenna.

Next, the process of defuzzification was applied to adjust the y-axis of Figure 91 from fuzzy IPL values to crisp IPL values which depict the real pathloss values more closely (in dB). Figure 92 shows the minimum and maximum pathloss values for actual and predicted IPL patterns attained through neural networks. The results only vary by 2 and 4 dB between actual and predicted values. Figure 93 shows the linear interpolation of the fuzzified IPL pattern into crisp values using the predicted minimum and maximum values. The actual IPL data is also plotted on the same graph.

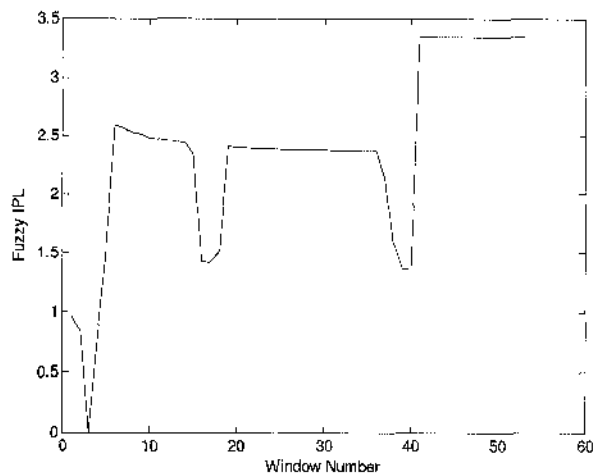


Figure 91. Fuzzified IPL Pattern for DME-L (A320).

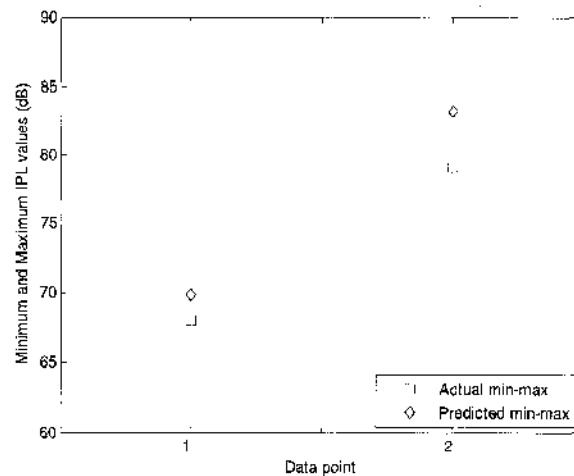


Figure 92. Minimum and Maximum IPL Prediction for DME-L (A320).

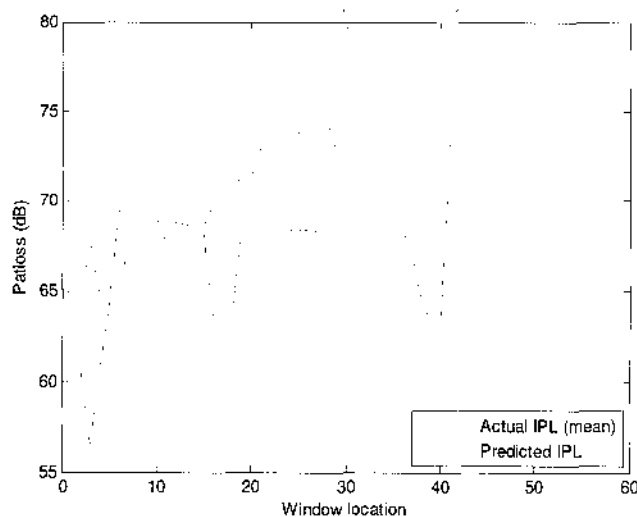


Figure 93. Defuzzified and Real IPL Pattern for DME-L (A320).

The defuzzified pattern was then reduced (only recorded at every 5th window) and sent to the non-linear module of NFM. The original 14 characteristics of all aircraft systems were also sent to the non-linear module. Figure 94 shows the pathloss predictions for A320 DME-L. IPL data from two actual trials of DME-L calculations is reported in red, while the predicted IPL pattern for DME-L is reported in blue. Unlike results for VHF-L, the predicted IPL path, in terms of accuracy and trend matched the real DME-L very closely. There are two sharp drops near the emergency exits of the aircraft.

Figure 95 shows the actual versus predicted IPL data on a larger scale by including all training data used by NN before prediction. The training data is represented in green, the actual two trials for DME-L are represented with dashed red lines, while the predicted IPL pattern for DME-L is represented in a solid red line. The mean, variance, standard deviation and minimum pathloss values are also reported below the figure for both the mean of real data as well as predicted data. Although not much variation exists for DME-L, unlike VHF-L, the overall means of real versus predicted data for DME-L vary by about 2 dB. The minimum IPL value predicted by neural networks is about 1.5 dB higher than actual minimum value.

Finally, Figure 96 shows the actual DME-L patterns (mean) for all three aircraft. As observed, the DME-L measurements for B757 and A319 were about 5 to 7 dB lesser than the pathloss values for A320. Perhaps the sharp decreases in the predicted IPL pattern for VHF-L may be due to forcing similarity in pattern from other systems. Therefore, overall, the neural networks again did a very acceptable job in predicting the IPL pattern for VHF-L in A320, after learning the IPL patterns from systems installed on other aircraft types.

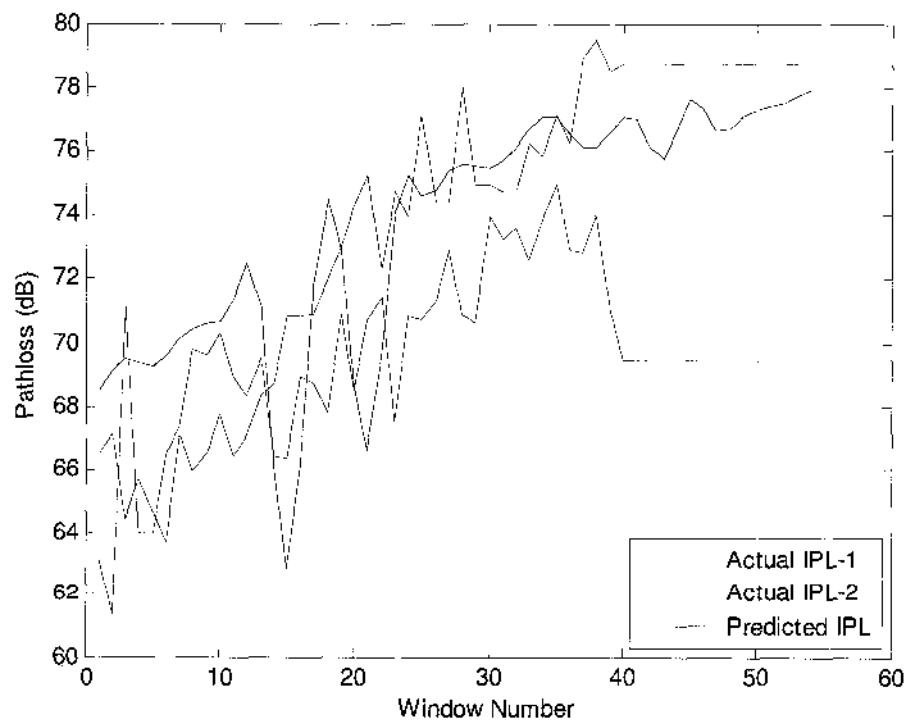


Figure 94. Actual vs. Predicted IPL for DME-L (A320).

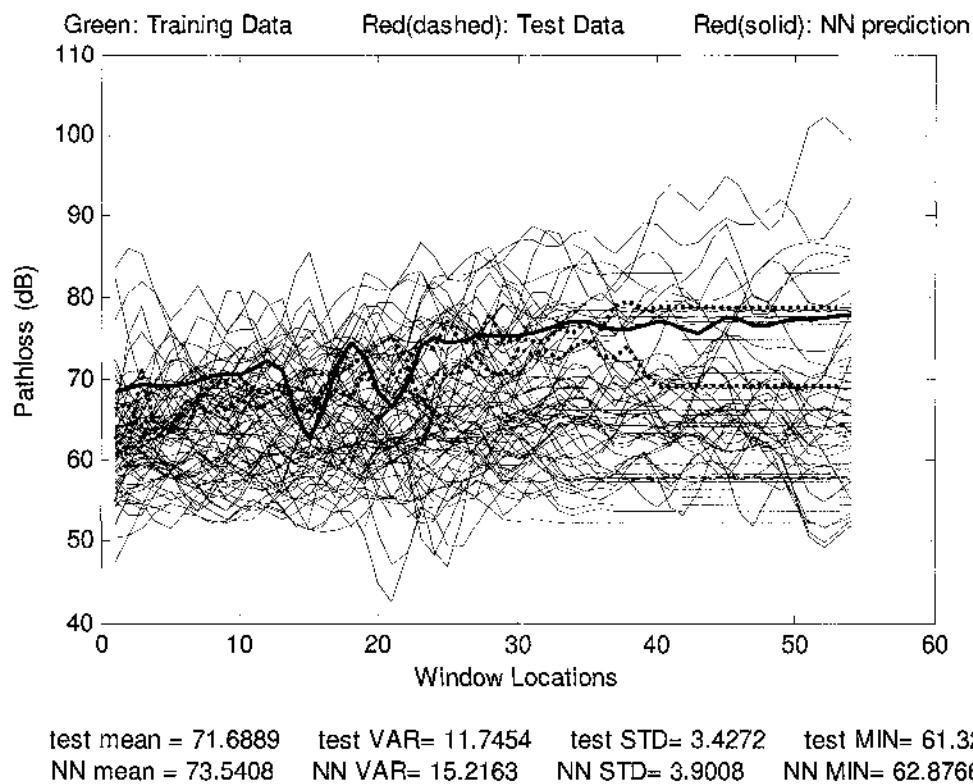


Figure 95. Actual, Predicted and Training Data for DME-L (A320).

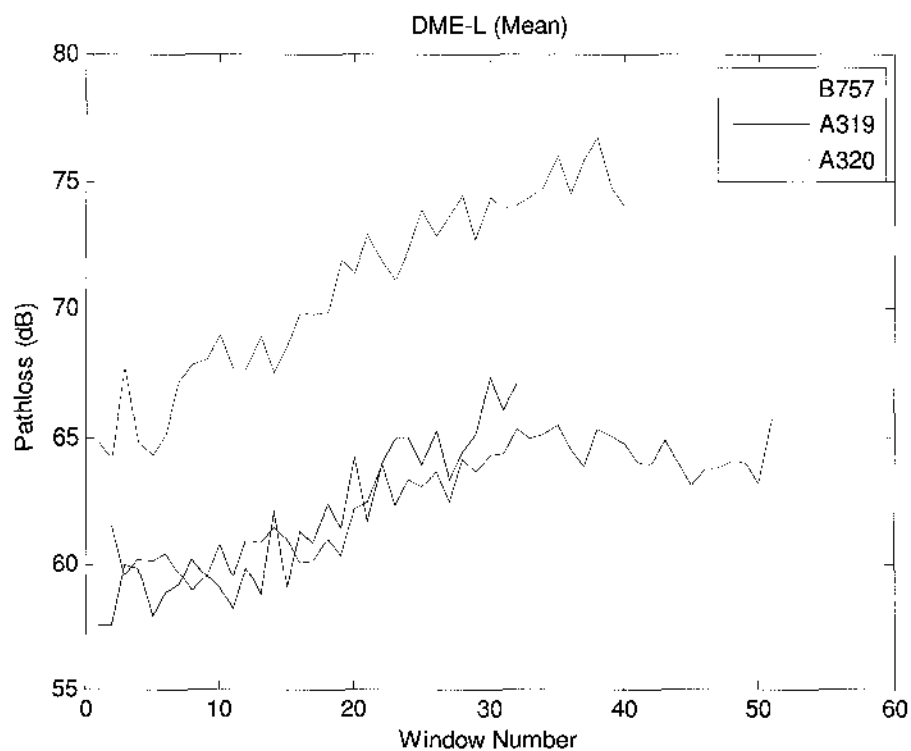


Figure 96. Mean IPL Patterns for DME-L from all Aircraft (B757, A319 and A320).

4.4 Comparison and Conclusion on EMI Modeling Techniques

In general, the NFM model produced very acceptable results. The model was created using MATLAB and was simulated on a personal laptop (Dell XPS M1210) with Intel Duo Centrino Processor (1.86 GHz) and 2 GB of RAM. One round of simulation (approximation of IPL values on all windows for a particular system of interest) took about 15 minutes to run and predict the needed IPL pattern. The overall results for DME-L matched the actual data comparably; however, the results for VHF-L were not as favorable. The general mean, minimum and maximum pathloss values were successfully predicted for both systems.

Devereus *et al* used FDTD to simulate a similar problem on a scaled cylindrical fuselage. They were able to achieve accurate results for systems with operating frequencies less than 300 MHz. The reported weakness of their approach was the time it took to perform one simulation along with the frequency range due to limited computational ability. The exact time or processing speed used for the model were not reported in their publications [50].

Georgakopoulos *et al* also used FDTD to find out the pathloss value of one window at a time. Due to the need for a single computation (one window), they were able to incorporate all frequency ranges in their modeling (from 100 MHz to 6 GHz). Unfortunately, they also reported excessive computation time as the weakness of their model. For IPL pattern prediction problem for the entire length of fuselage, their model would have to be simulated individually for each window location, with minimum pathloss recorded every time. Georgakopoulos *et al* compared their predicted pathloss values with the measured values on a scaled model of a rectangular fuselage [48].

Vahala *et al* used a unique approach of multiscattering where they solved the traditional Maxwell's equations in the parabolic form. Instead of pathloss values on windows only, they performed calculations on the entire interior of the fuselage, including windows. They reported fast computation speed; however, with prediction limits for systems with frequency bands of greater than 1 GHz. The results by Vahala *et al* are from the study that compare predicted IPL values to actual measurements from real aircraft, instead of modeled or scaled aircraft [55].

Although the results from the other three above mentioned techniques were comparable to real pathloss data, the models were limited either due to computation speed, or frequency range. The NFM successfully overcame these limitations and predicted pathloss patterns accurately and efficiently without a big computational demand. Although NFM did provide variation in the predicted IPL pattern for VHF-L, the overall results provide a promising future for this model in electromagnetic propagation prediction needs.

CHAPTER 5

CONTRIBUTIONS AND FURTHER RECOMMENDATIONS

This chapter briefly outlines the final conclusions and contributions of this study. The first section lists the contributions of NFM to the real-world problem of electromagnetic interference. The second section includes a brief overview of the cascaded model structure with its advantages. The third summarizes NFM design and provides guidelines on using NFM over other types of numerical modeling techniques. The last point goes over the application of this model to real world interference predictions. Recommendations on future work are listed at the end of the chapter.

5.1 Summary of the Contributions

Contributions are summarized and listed:

1. This study explored the capability of the soft computing techniques in conjunction with linear numerical methods. It provides a proof of the ability of the novel combination to identify, model, simulate and provide meaningful information for complex electromagnetic wave propagation phenomenon.
2. The first cascaded model, with linear fuzzy logic module and nonlinear neural network module, for prediction of pathloss across all windows of an aircraft for systems operating in either low or high band is presented. It provides a model with better performance.
3. The first model of interference pathloss predictions using real IPL data and actual aircraft characteristics, instead of scaled is successfully incorporated.
4. This study presents and demonstrates an efficient NFM designing strategy. It includes graphical analysis, fuzzy inductive reasoning, and parametric optimization through neural network training.
5. The results provides new insights into the coupling phenomenon in terms of rule surface, similarity and individual difference between various aircraft systems and their coupling patterns.
6. This study presents and demonstrates a new way to solve electromagnetic problems by using expert systems instead of numerical techniques. It provides many potential application opportunities.

5.2 Conclusions about the Model Structure

Nonlinear soft computing techniques are capable of identifying, modeling, simulating and providing meaningful information about complex electromagnetic coupling phenomenon onboard aircraft due to wireless devices. Rather than purely linear assumption, or exclusive nonlinear modeling techniques, the effective combination of both the linear and nonlinear techniques could present the complex dynamics with higher accuracy. Using the same technology, other systems could be modeled.

The following are the characteristics of this combined model structure. The final model is a cascaded structure of Fuzzy (linear) model and Neural network (non-linear) model. It is based on our hypothesis from expert knowledge that the measured pathloss consists of linear intrinsic mechanisms and nonlinear noisy inputs. Fuzzy logic is an expert system technique specified in efficiently modeling linear predictions. Here, it is used to interpret the linear effects on pathloss values due to the location of aircraft exits as well as effects from angle and aircraft system's polarization. Neural network is a non-linear modeling technique aimed to model complex, unclear or vague systems with self-learning ability. The resulting analysis shows that this hybrid model not only has the capability to model the pathloss pattern, but also has better generalization properties than the previous numerical techniques.

Therefore, proposing and testing this novel cascaded model structure is one of main contributions of this work to the field of modeling and simulation of electromagnetic propagation, which can even extend to other complex systems. We feel that it is important to implement soft computing techniques, which are intelligent, self-learning, and robust, into electromagnetic systems, which are nonlinear, complex, unclear, and expert-subjective.

5.3 Conclusion about NFM

Although the use of neural networks and fuzzy logic together in modeling is not a new concept, the technique has not been applied to complex electromagnetic systems. The results show that proper designing of fuzzy rules can generate a NFM system with good performance. The contribution of our study is that an effective prediction tool using NFM is investigated. The study includes extensive graphical analysis of IPL data, fuzzy inductive reasoning, and parametric optimization through neural network training.

Comparison with the previous model illustrates both advantages and disadvantages of NFM. Our study shows that NFM has fewer parameters and less computational load compared to traditional numerical techniques, although the final pathloss predictions for the tested systems are not as precise as those found through FDTD analysis [48]. Also, NFM, in general, has less sensitivity with respect to pathloss patterns from other systems, is capable of learning from and modeling complex systems, and can be easily interpreted to provide meaningful results. As a consequence, it paves a broad way to real-world implementation. Hopefully, our contribution in modeling electromagnetic propagation dynamics could assist in better designing the future aircraft to decrease the threat to aviation systems due to PEDs.

5.4 Conclusion about Applications Domain

As mentioned earlier, the use of NFM over standard numerical techniques is not only advantageous because of the linear and nonlinear cascaded structure, incorporation of large frequency band, but also because unlike other models, NF model incorporated expert knowledge about the system. The fuzzy rule base could be interpreted easily by physiological meanings. The disadvantage of NFM modeling approach is that this modeling approach needs pre-training process, therefore, requiring as much data as possible for the most effective prediction. Also, the model can become computationally extensive, but more accurate, if the number of nodes in the neural networks is increased to include more inputs.

The model can be used to understand the effects of antenna locations along with their polarizations on the coupling patterns inside an aircraft. It can assist aircraft manufacturers in creating better designs with least locations of coupling inside the aircraft by changing the locations of antennas and exits. Although the overall IPL pattern across all windows did not match the actual IPL pattern exactly, the model was able to predict the minimum and maximum IPL values very precisely. The minimum IPL value is of most concern when assessing safety issues and creating rules on the approved amount of coupling with antenna systems. The NFM can also be used to predict coupling patterns in other complex domains, such as buildings.

5.5 Recommendation for Future Work

Our original motivation of this study was to predict the pathloss patterns for selected systems inside a commercial aircraft using a computationally efficient model which yielded comparable results. The developed method met the basic objectives; however, the following major areas need to be further investigated.

1. The model should be further verified for other systems on A320 besides VHF-L and DME-L.
2. The location of the aircraft wing has also been determined to play a large role in the overall coupling pattern. Therefore, in future work, a new rule needs to be added to the fuzzy rules which incorporated the location of the wing and its effect on pathloss pattern. This would require additional inputs of wing locations from the aircraft schematics.
3. Mitigation work has been studied in previous work [23], however, due to limited time, it was not incorporated in modeling. The effects of shielding should be included in the fuzzy model and should effectively predict shielding's effect on pathloss values throughout an aircraft.
4. B737, B757, A319 and A320 are aircraft of similar structure. Much more IPL data has been recorded for much smaller aircraft, such as regional jets. The model should be verified and improved after testing the IPL results from smaller aircraft.
5. The modeled developed in this study should be incorporated in a user-friendly software, which should contain a database of all IPL values ever collected. The software will be more effectively utilized by interested agencies, instead of stepping through the code currently written.

In summary this study is just a beginning step of applying the expert knowledge-based techniques to electromagnetic propagation phenomenon. The initial results are very promising, and provide an insight for future work.

APPENDICES

Appendix A: IPL Measurement overview

Appendix B: Fuzzy logic system definition

Appendix C: Neural networks definition

Appendix D: Measured IPL Data

Appendix A: IPL Measurement Overview

To address the interference issue, NASA entered into a cooperative agreement with United Airlines, Delta Airlines and Eagles Wings Incorporated to conduct additional Interference Pathloss (IPL) measurements and to address several technical issues. One issue was to measure additional IPL data using a thorough and consistent set of procedures. IPL is the measurement of the radiated field coupling between passenger cabin locations and aircraft communication and navigation receivers, via their antennas and is required for assessing the threat of PEDs to aircraft radios. IPL data is very dependent upon airplane size, the interfering transmitter position within the airplane, and the location of the particular antenna for the aircraft system of concern. Systems considered were the instrument landing system Glideslope (GS), Traffic Alert and Collision Avoidance System (TCAS), VHF Communication Systems (VHF), instrument landing system Localizer (LOC), Marker Beacon (MB), Distance Measuring Equipment (DME), Air Traffic Control (ATC), VHF Omnidirectional System (VOR), and Global Positioning System (GPS) [42].

Another issue concerned aircraft-to-aircraft repeatability. This repeatability issue resulted in measurements on six similar B737, seven similar B757, two similar A319 and four similar A320 aircraft. NASA provided measurement instrumentation, data acquisition and test control software development and support, and staff. EWI was tasked to lead the overall effort and to conduct analysis. While the actual aircraft were made available by United Airlines and Delta Airlines during independent trips to Victorville, CA, San Francisco, CA and Atlanta, GA.

IPL measurements were conducted on the nineteen airplanes for VOR/LOC, VHF Comm., GS, TCAS, and GPS, DME, ATC and MB systems. The interference source, simulated with dipole, bi-conical and dual-ridge horn antennas, was positioned to radiate toward each of the windows and the door exits on one side of the aircraft. When taking IPL measurements, it was assumed that for PEDs interference problems, the interference source is located within the passenger cabin, and the victims are aircraft radio receiver systems. A common path of PED interference is through the windows or door seams, along the aircraft body, and into the aircraft antennas. The interference signal picked up

by the antennas is channeled back into the receivers to potentially cause interference if they are higher than the receiver interference thresholds. Figure A.1 shows an illustration of typical radio receiver interference coupling paths. The signals are transmitted through the windows and doors of the aircraft, and creep along the aluminum surface of the fuselage to reach the antenna system of the aircraft.

Figure A.2 shows a basic setup for conducting IPL measurements. IPL data was taken by radiating a low powered continuous wave (CW) test signal, frequency-synchronized to the spectrum analyzer sweep and fed to the test transmitting antenna via a double-shielded RF cable. The spectrum analyzer, laptop computer controller, and preamplifiers were located inside the aircraft. The spectrum analyzer input cable was connected to the aircraft radio receiver rack cable in the avionics equipment bay.

To perform an IPL measurement, the team measured the RF power loss between the calibrated signal source and a spectrum analyzer, via the entire length of test cables plus the aircraft cable, plus the free space loss between the reference antenna and the aircraft antenna. Swept CW was preferred over discrete frequency measurement, according to RTCA/DO-233. A pair of test cables were used to connect the instruments to the aircraft antenna cable and to the transmit antenna. An amplifier (optional) was used to increase the signal strength depending upon the capability of the tracking source and the path loss level. Sometimes, a preamplifier is needed in the receive path near the spectrum analyzer for increased dynamic range; however, in this particular setup, the preamplifier was internal to the spectrum analyzer.

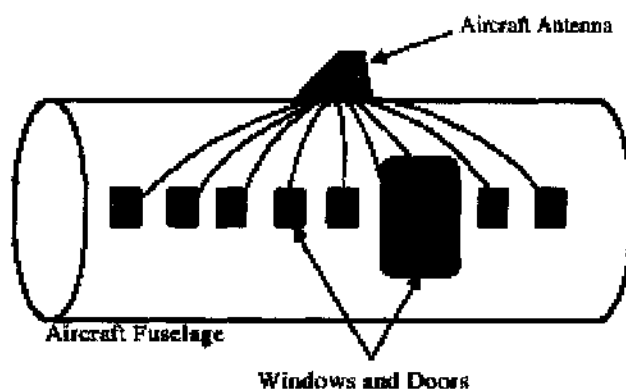


Figure A.1. Illustration of Typical Radio Receiver Interference Coupling Paths.

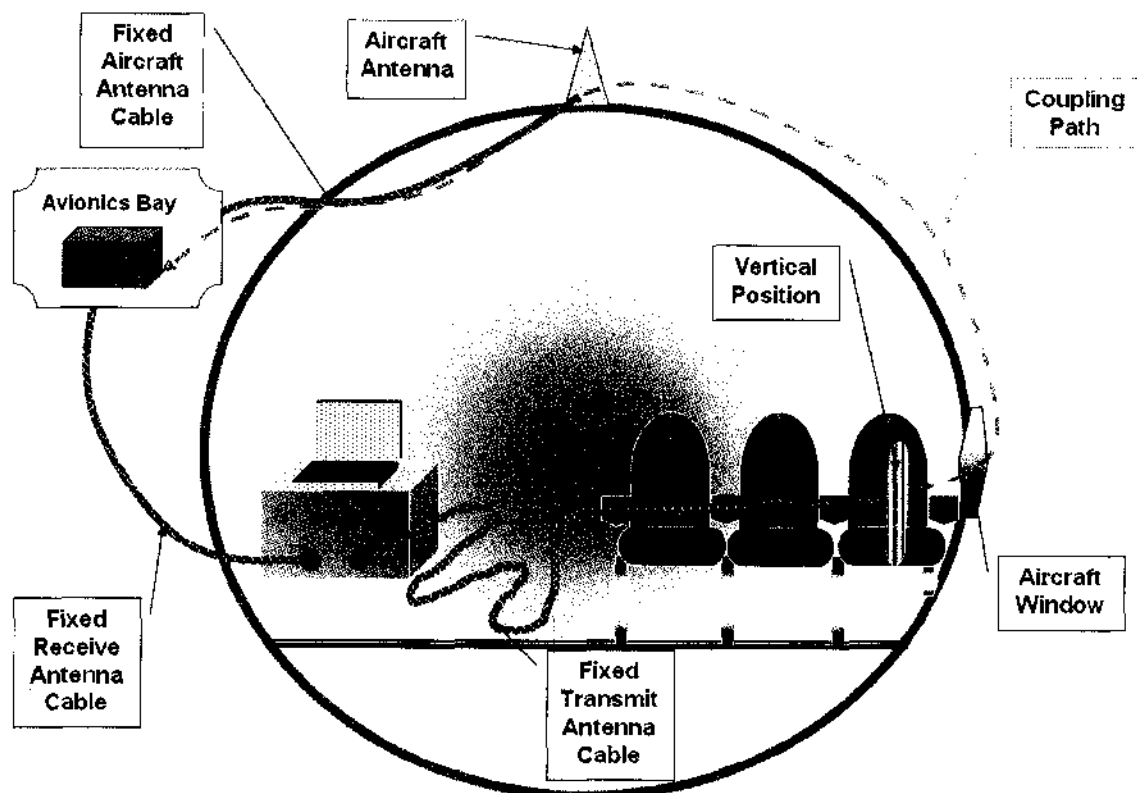


Figure A.2. Illustration of Instrumentation setup for IPL measurements.

Table A.1. Aircraft System and Measurement Antenna Characteristics.

Aircraft Systems	Spectrum (MHz)	Measurement Frequency Range (MHz)	Transmit Antenna Type	Free-Space Antenna Gain (dBd)
MB	75	70 – 80	Bicon	-19.32
LOC	108.1 – 111.95	108 – 118	Dipole	+1.25
LOC	108.1 – 111.95	108 – 118	Bicon	-12.85
VOR	108 – 117.95	108 – 118	Bicon	-12.85
VHF	118 – 137	116 – 138	Dipole	+0.05
VHF	118 – 137	116 – 138	Bicon	-10.9
GS	328.6 – 335.4	325 – 340	Dipole	+0.25
GS	328.6 – 335.4	325 – 340	Bicon	+1.03
DME	962 – 1213	960 – 1215	Bicon	+5.32
ATC	1030	1020 – 1040	Dual-Ridge Horn	+4.85
TCAS	1090	1080 – 1100	Dual-Ridge Horn	+5.26
GPS	1575±2	1565 – 1585	Dual-Ridge Horn	+7.5

For most systems, IPL was defined by the ratio (in dBm), or the difference in dB, between the power radiated from the transmit antenna to the power received in the avionic bay's receiver. For GPS testing, however, IPL was defined to be the differences in power between transmit antenna and aircraft antenna only. The antennas used in the measurement include dipoles for frequencies in the GS band and below, and a dual-ridge horn antenna for the frequencies in the TCAS band and above. Due to obstacles in the plane, such as seats, walls, windows etc, it was considered best not to correct for the free space antenna gain in the definition for IPL. However, free-space antenna gains, as provided by the antenna manufacturers, are shown in Table A.1 that can be used to factor in the transmit antenna free-space gain, if so desired. As shown in table A.1, a transmit antenna was used to simulate an interference source. The tuned dipole or biconical transmit antenna was used for measurements in MB, LOC, VOR, VHF and GS bands, and a dual-ridge horn antenna was used for measurements in the DME, ATC, TCAS, and GPS bands.

Testing Details

This section includes a step-by-step procedure of conducting IPL measurements, used by Delta Airlines. The procedure includes the instrumentation needed, as well as the detailed connections and set-up.

The following instruments and cables are required to perform IPL measurements, please refer to figure A.3 for the pictures of the parts defined below:

- a. Laptop Computer with HP VEE Path Loss Measurement Software.
- b. Spectrum Analyzer. Used Agilent E4407B ESA-E Series Spectrum Analyzer in this write-up.
- c. Calibration Cable
- d. Power Amplifier with SMA Power-Amp Cable and Power Supply
- e. 2 Coaxial cables for Aircraft Antenna and Transmit Antenna
- f. Transmitting Antenna (i.e. Biconical, Dipole, Horn etc.)



Figure A.3: Instrumentation required for IPL Measurements.

Instrumentation Set-up

In the testing procedure, the laptop will be used to capture screen shots from the spectrum analyzer as well as for storing data.

After powering up the laptop using the power supply, enter the username and password. (Sticker on computer keyboard) From desktop, launch “PathLossMeas_SA_AutoDownload_ver3.0.1” by double clicking on the icon. As shown in Figure A.4, connect the 120VAC cable to the spectrum analyzer. Using another set of cable, connect laptop’s PCMCIA-GPIB card (National Instruments) with the spectrum analyzer’s HP-IB parallel port. Turn the Spectrum Analyzer on by using the power button on the lower left corner on the front panel. Let the Spectrum Analyzer perform initial alignments automatically. Calibrate the Spectrum Analyzer by using the Calibration cable shown in figure A.5. Connect one end of the calibration cable to “Input 50Ω” while the other end to “AMPTD ref out” connector on the front panel of the spectrum analyzer. Go to Systems² → alignments³ → align now → All

² Boxed names refer to physical soft buttons found on the *front panel* of the Spectrum Analyzer

³ Underlined names refer to options available on the *display screen* of the Spectrum Analyzer.

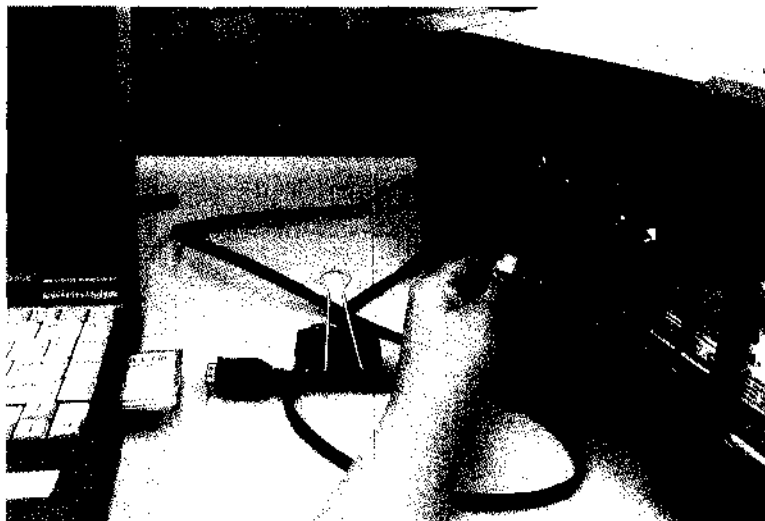


Figure A.4. Illustration of Laptop to Spectrum Analyzer connection

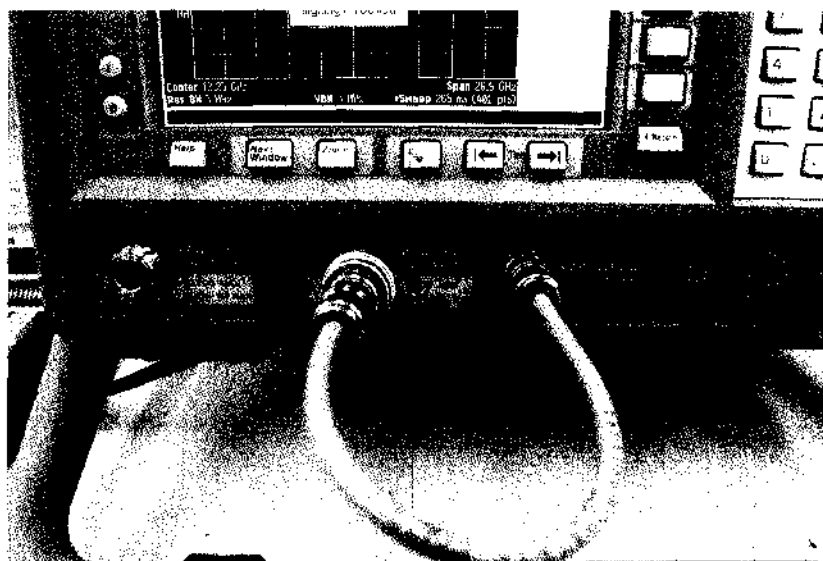


Figure A.5. Illustration for Spectrum Analyzer's Calibration.

Test Cable Loss (TCL) Measurements:

After setting up the spectrum analyzer, a TCL measurement needs to be performed for each system tested. TCL Measurements are necessary to observe the power loss incurred in the double shielded RF Cables. This procedure must be performed every time for each system of the aircraft during testing, i.e. VHF, TCAS etc.

Set the Start and Stop frequencies for the system of concern. Please refer to table A.1 for aircraft systems and their frequency bands. For example, VOR ranges from 108 MHz to 118 MHz: Go to "Frequency" → "Start Freq" → "1 0 8" → "MHz" to set starting frequency. Similarly, go to "Stop Freq" → "1 1 8" → "MHz" to set the stopping frequency. Turn the Source on by going to "Source" → "on". Make sure that the Source "Amplitude" is -10 dBm. If not, then change to "1 0" → "-dBm"

Set the reference to 0 dBm and attenuation to "auto" by going to "Amplitude" and changing the "Ref" to "0" → "dBm"; and "Atten" to "Auto" on the display screen. Go to "View/Trace" → "ClearWrite" to begin the tracing of the signal on the spectrum analyzer. Perform peak search to calculate and record the TCL Measurement by pressing "Peak Search".

$$\text{TCL Measurement} = \text{Source Amplitude} - (\text{result})$$

Where the Source Amplitude was set to -10 dBm in this case, and the "result" is found from the peak search above. Therefore, if the "result" was -11.19 dBm, then $\text{TCL} = -10 - (-11.19) = 1.19 \text{ dBm}$.

IPL Measurements

The following section includes the connections necessary to perform the IPL measurements:

Using Figure A.6 as a summary, connect an SMA Power-amp cable from “RF out 50Ω” connector on the spectrum analyzer to the input of the Power Amp. Then connect a double-shielded RF cable from the output of the Power-amp to the transmitting antenna. Connect the power supply to the power-amp⁴.

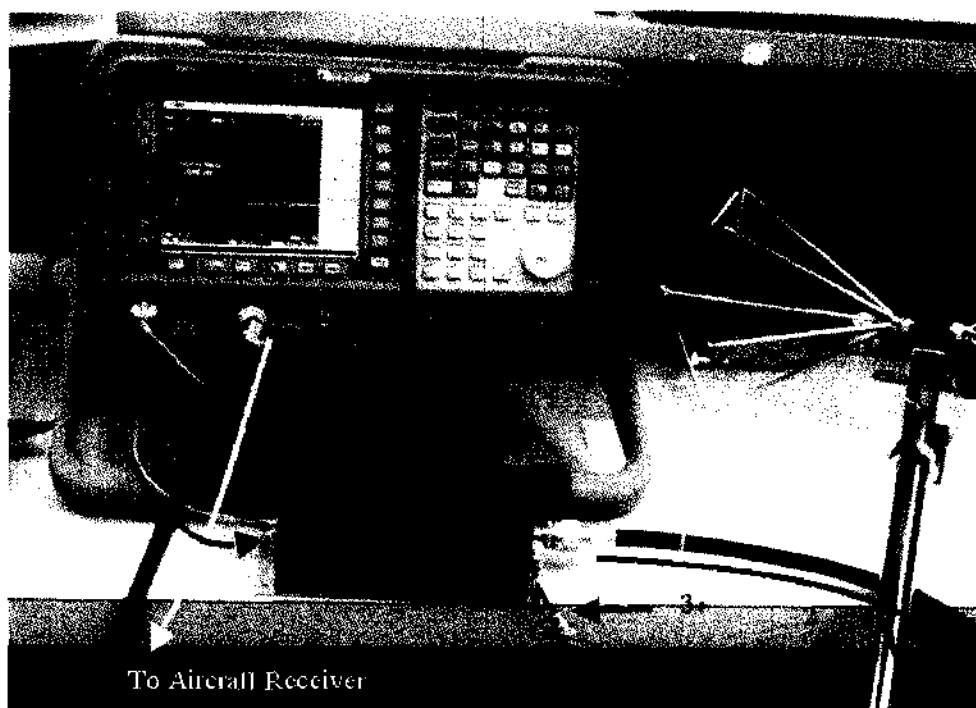


Figure A.6. Complete hook-up of Spectrum Analyzer with power-amp, coaxial cables, transmitting antenna and laptop computer.

Connect a double-shielded RF cable from the “Input 50Ω” connector of the spectrum analyzer to the receiver of the aircraft, usually located in the avionics bay. Before proceeding to measuring and recording IPL Measurements, make sure to change the following settings on the spectrum analyzer: Go to “Source” → “Amplitude” → “1”

⁴ *** Caution: Make sure that steps 1 and 2 above are performed before performing this step! ***

0” → “-dBm”. Also make sure that the “Ref” under “Amplitude” is “-10 dBm” while the “Atten” is “0 dBm Manual”⁵.

Take IPL Measurement by going to “View/Trace” → “ClearWrite” and performing “Peak Search”

To capture the data in the laptop, please refer to the screen shot in figure A.7. Begin by clicking on the check box next to “Enter Data Dir & Filename Root”. In the pop-up directory, find the folder named which will be used to store all data collected during testing. Open the folder, enter test name and click “save”. On the original screen (in figure 2.8), observe that the software should have identified the type of spectrum analyzer connected to the system (in this case, “E4407B” on the right hand column). Click on the check box next to “Change File Index Number” whenever it needs to be set. Initially, indexing begins at 1, and automatically increments upon each recording; therefore, use this feature if an erroneous measurement was occurred and data needed to be retaken.

Finally, click on the check box next to “Download & Record Trace”. This step should result in the capture of the screen currently on the spectrum analyzer (after “View/Trace” → “ClearWrite” → “Peak Search” was performed on the spectrum analyzer). Observe that the software confirms the start and stop frequency as well as records the maximum frequency measured by the spectrum analyzer, denoted by “Marker Amp” (in this case, -11.16 dBm).

⁵ Side Note: The source amplitude is set to -10 dBm because the power amplifier ZHL-42W has a gain of approximately 37 dB across all frequencies possible. The power amplifier also only has a power output capability of around 27 dBm. Therefore, to make sure that the actual power output remains less than 27 dBm (which can possibly be as high as 37 dBm), we set the source amplitude to 10 dBm, instead of leaving it at 0 dBm.

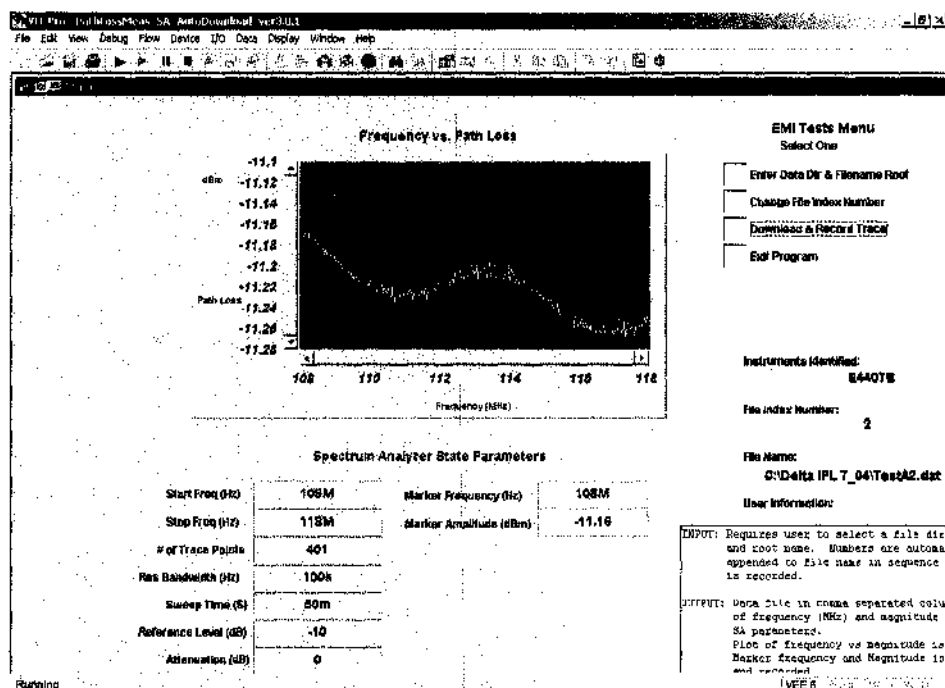


Figure A.7. Illustration of HP VEE Path Loss Measurement Software.

Summary of Steps for Measuring IPL Data

The measurement process for each system on each aircraft typically involved the following steps:

1. Conduct 1-meter path loss measurement. IPL was measured with the transmit antenna positioned one meter from the aircraft antenna. This simple step established a baseline measurement and helped detect any excessive aircraft antenna cable loss. Excessive cable loss could indicate possible signs of connector corrosion in the path. These data were not needed to compute the IPL.
2. Configure the spectrum analyzer to the proper reference level, resolution bandwidth, attenuation level and desired measurement frequency band. Configure the tracking source to track the frequency sweep of the spectrum analyzer. Set the tracking source output to desired power level.
3. Measure test cable and aircraft cable “through” losses.
4. Position the transmit antenna at a desired location, typically near a window or door. Point the antenna to radiate toward a window or door seam.
5. Clear spectrum analyzer’s trace. Set spectrum analyzer to “Trace Max Hold” and sweep continuously across the desired measurement band.

6. Scan the transmit antenna slowly along the door seam, while the spectrum analyzer is still set at "Trace Max Hold". No scanning was needed at the windows due to small window sizes.
7. Record trace and the peak marker value. For systems that experience narrowband peaks caused by strong local transmitters such as LOC, position the marker at the peak of the broadband envelope while avoiding the narrowband peaks. Record data at this marker location.
8. Change polarization and repeat from step 2 so that both vertical and horizontal polarizations of the transmit antenna are included.
9. Relocate the transmit antenna to another window/door and repeat from step 4.

Post processing involved removing the measured system "through" loss from the total path loss data. The system loss includes the effects of test cable losses, amplifier gains, and other types of losses/gains in the measurement path. For step 1 above, please refer to Figure A.8 for an illustration of a 1-meter path loss measurement near a B737 VOR/LOC antenna located in the tail. A 1-meter path loss measurement was conducted to check the integrity of the aircraft antenna path. The results were not used to calculate IPL and are not reported in this document.



Figure A.8. Illustration of 1-meter path loss measurement near B737 VOR/LOC Antenna.

Figure A.9 shows a measurement being conducted with the transmit antenna at a window, and the computer and software used for data acquisition (detailed steps provided in previous sections). Although the testing instruments and computers were located within the passenger cabin, spurious emissions from these equipment are too low to cause significant error in measurement.

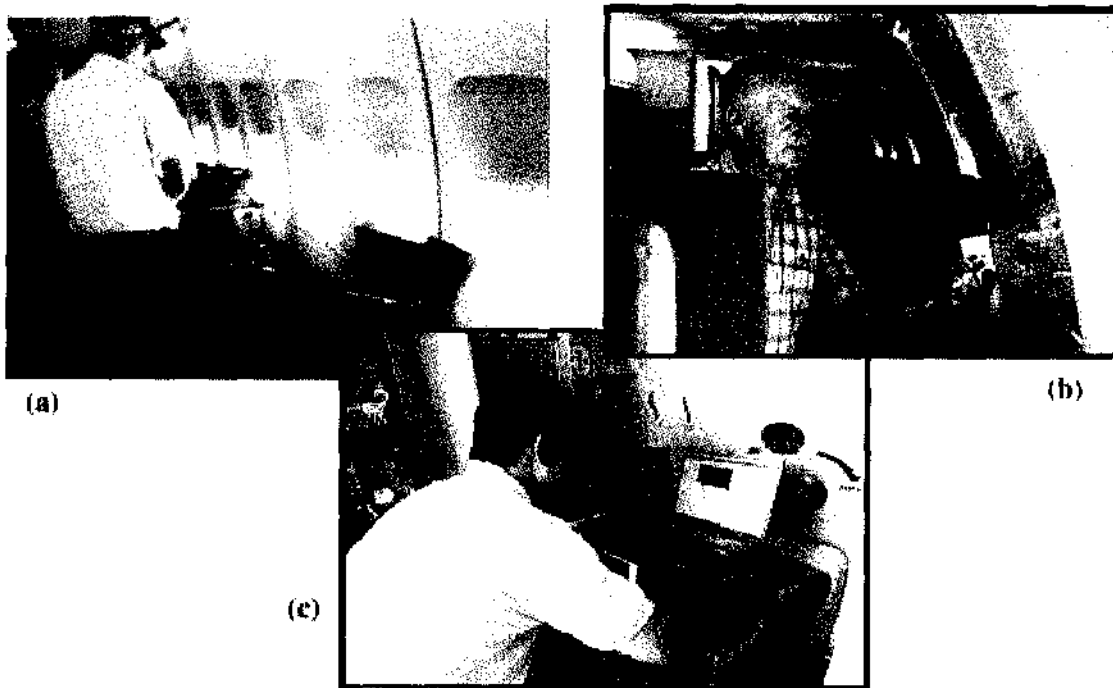


Figure A.9. Illustration of various phases of testing performed by the test team.

Appendix B: Fuzzy Logic System Definition

Here, we briefly review basic concepts of fuzzy sets and fuzzy logic theoretical operations [20, 21].

Definition B.1 (Fuzzy set): For an assumed universe of discourse, X , a fuzzy set, A in X is specified by its membership function, μ_A ,

$$\mu_A : X \rightarrow [0,1].$$

Thus, each element, x in set X has a degree of membership in set A which takes one value between 0 and 1. A fuzzy set may be viewed as a generalization of the concept of an ordinary set (that is, a crisp set), whose membership value takes on 0 or 1 only.

The fuzzy membership functions for fuzzy sets can have many different shapes, depending on definition. Figure B.1 illustrates some of the possible membership functions, we have: (a) the Γ -function: an increasing membership function with straight lines; (b) the L -function: a decreasing function with straight lines; (c) the Λ -function: a triangular function with straight lines; (d) the singleton: a membership function with a membership function value 1 for only one value and the rest is zero. (e) the Gaussian function: a membership function with gaussian distribution curve. There are many other possible functions such as trapezoidal, sigmoidal or even arbitrary.

Definition B.2 (Support, Center, Fuzzy singleton) The support of a fuzzy set F is the crisp set of all points $x \in U$ such that $\mu_F(x) > 0$. The center of a fuzzy set F is the point $x \in U$ at which $\mu_F(x)$ achieves its maximum value. If the support of a fuzzy set F is a single point in U at which $\mu_F(x)=1$, then f is called a fuzzy singleton.

Definition B.3 (Intersection, Union, Complement) Let A and B be two fuzzy sets in U . The intersection $A \cap B$ of A and B is a fuzzy set in U with membership function defined for all $x \in U$ by

$$\forall x \in U : \mu_C = \min \left[\mu_A(x), \mu_B(x) \right]$$

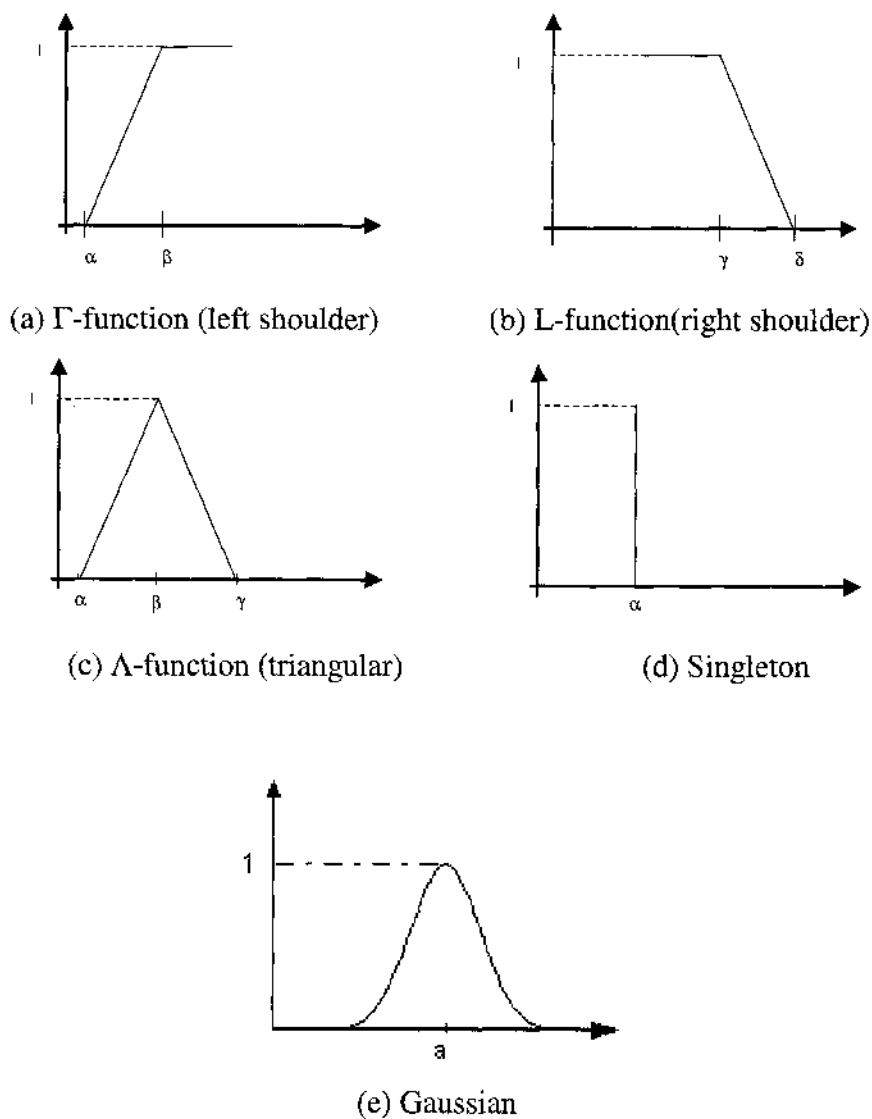


Figure B.1. Examples of Membership Functions.

Definition B.3 (Intersection, Union, Complement) Let A and B be two fuzzy sets in U. The intersection $A \cap B$ of A and B is a fuzzy set in U with membership function defined for all $x \in U$ by

$$\forall x \in U : \mu_C = \min \left[\mu_A(x), \mu_B(x) \right]$$

The union of $A \cup B$ of A and B is a fuzzy set in U with the membership defined for all $x \in U$ by

$$\forall x \in U : \mu_C = \max[\mu_A(x), \mu_B(x)]$$

The complement of A is a fuzzy set in U with the membership function defined for all $x \in U$ by

$$\forall x \in U : \mu_{\bar{A}} = 1 - \mu_A(x)$$

In more general terms, we're defining what is known as the fuzzy intersection or conjunction (AND), fuzzy union or disjunction (OR), and fuzzy complement (NOT).

Definition B.4 (Fuzzy rule base) a fuzzy rule base, an extraction of an expert's knowledge, consists of a collection of fuzzy IF-THEN rules in the following form:

$$R(L): \text{ IF } \underline{x}_1 \text{ is } F_1^L \text{ and } \dots \text{ and } \underline{x}_n \text{ is } F_n^L, \text{ THEN } y \text{ is } G^L$$

Where F_i^L and G^L are fuzzy sets in $U_i \subset R$ and $V \subset R$ respectively. $\underline{X} = (x_1 \dots x_n)^T \in U_1 \times \dots \times U_n$ and $y \in V$ are linguistic variables. Let M be the number of fuzzy IF-THEN rules in the form of (B.5) in the fuzzy rule base; that is $L=1, 2, \dots, M$. The \underline{x} and y are the input and output to the fuzzy logic system, respectively. Basic pure fuzzy inference is composed from fuzzy rules shown in Figure B.2.

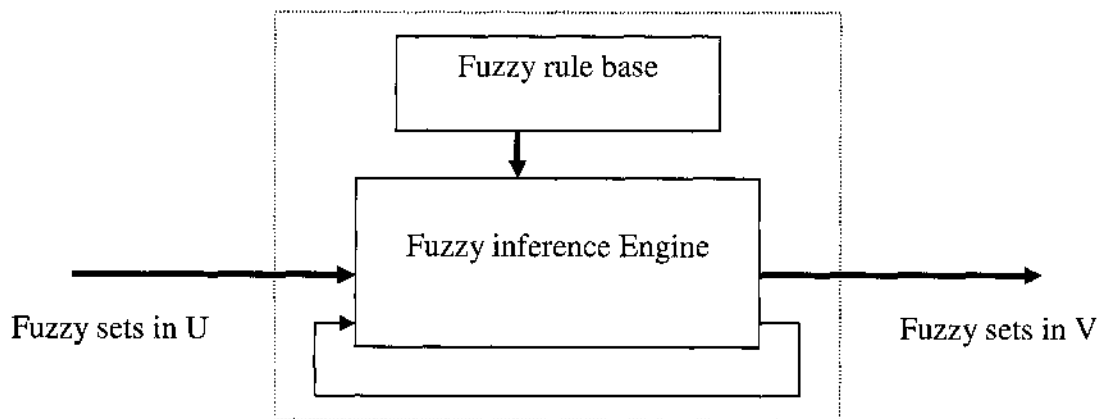


Figure B.2. Basic configuration of pure logic system.

Definition B.5 (Fuzzifier, Defuzzifier) the fuzzifier performs a mapping from a crisp point $\underline{x} = (x_1, \dots, x_n)^T \in U$ into a fuzzy set A, in U. There are at least two possible choices of this mapping. We introduce the most popular one.

- Non singleton fuzzifier: $\mu_A(\underline{x}) = 1$. The $\mu_A(\underline{x}')$ decrease from 1 as \underline{x}' moves away from \underline{x} , for example, $\mu_A(\underline{x}') = \exp[-\frac{(\underline{x}' - \underline{x})^T (\underline{x}' - \underline{x})}{\sigma^2}]$, where σ^2 is a parameter characterizing the shape of $\mu_A(\underline{x}')$.

The defuzzifier performs a mapping from fuzzy sets in V to a crisp point $y \in V$. There are several possible choices of this mapping. We introduce the most popular one.

- Center of gravity defuzzifier:

$$y_c = \frac{\int y \cdot \mu_A(y) dy}{\int \mu_A(y) dy}$$

Figure B.3 shows the process of two rules execution union before defuzzification.

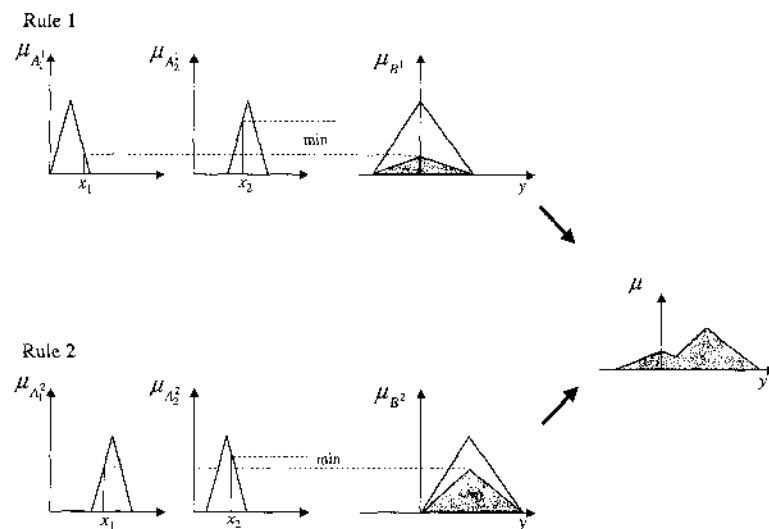
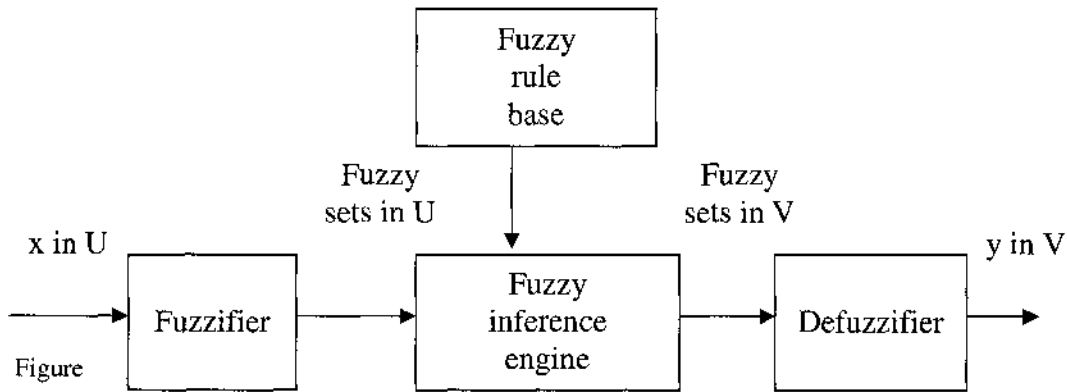


Figure B.3. Centroid Defuzzification diagram.

A fuzzy inference system shown in Figure B.4 consists of the fuzzifier, the fuzzy inference engine and the defuzzifier. Fuzzifier maps crisp points into fuzzy sets in U , and defuzzifier maps fuzzy sets in V to crisp points. In a fuzzy inference engine, fuzzy logic operations are used to combine the fuzzy IF-THEN rules in the fuzzy rule base into a mapping from input fuzzy sets in U to output fuzzy sets in V .

There are two types of fuzzy inference. The most popular one, which we are referring to so far, is known as Mamdani's fuzzy inference. The other is the so-called Sugeno, or Takagi-Sugeno-Kang fuzzy inference.

Definition B.6 (Mamdani-type inference) A type of fuzzy inference in which the fuzzy sets from the consequent of each rule are combined through the aggregation operator and the resulting fuzzy set is defuzzified to yield the output of the system.



B.4. Basic configuration of fuzzy logic system with fuzzifer and defuzzifier.

Definition B.7 (Sugeno-type inference) A type of fuzzy inference in which the consequent of each rule is a linear combination of the inputs. The output is a weighted linear combination of the consequents.

A typical fuzzy rule in a zero-order Sugeno fuzzy model has the form

if x is A and y is B then $z = k$, where A and B are fuzzy sets in the antecedent, while k is a crisp constant in the consequent. The defuzzifier is defined by weighted average method usually in terms of next equation.

$$output = \frac{\sum_{i=1}^n W_i Z_i}{\sum_{i=1}^n W_i} \quad W_i \text{ is the } i\text{th weight; } N \text{ is the number of rules}$$

These two types are similar in many respects. In fact the first two parts of the fuzzy process, fuzzifying the inputs and applying the fuzzy operator, are exactly the same. The main difference between Mamdani-type of fuzzy inference and Sugeno-type is that the output membership functions are only linear or constant for Sugeno-type fuzzy inference.

Appendix C: Neural Networks Definition

A simple neuron is an information-processing unit that is fundamental to the operation of a neural network. The block diagram of Figure C.1 shows the model of a neuron, which forms the basis for designing neural networks. Here we identify three basic elements of the neuronal model [24, 67]:

1. A set of synapses or connecting links, each of which is characterized by a weight or strength of its own as W_{ki} .
2. An adder for summing the input signals, weighted by the respective synapses of the neuron;
3. An activation function $\varphi(\cdot)$ for limiting the amplitude of the output of a neuron. The activation function is also referred to as squashing function in that it squashes the permissible amplitude range of the output signal to some finite value. There are various types of activation functions, such as threshold function, piecewise-linear function, and sigmoid function.

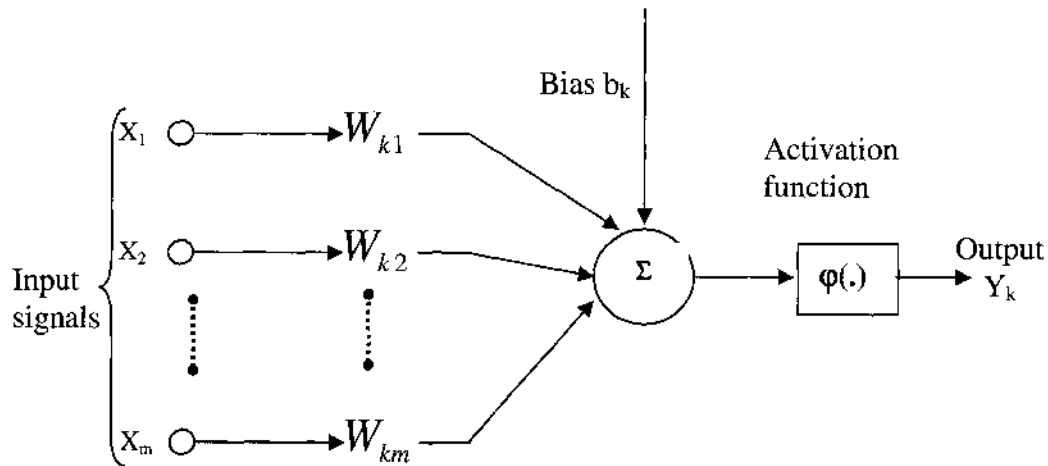


Figure C.1. Nonlinear model of a neuron.

The neuronal model of Figure C.1 also includes an externally applied bias, denoted by b_k . It has the effect of increasing or lowering the net input of the activation function. In mathematical term, we may describe a neuron k by the following pair of equations:

$$u_k \approx \sum_{j=1}^m w_{kj} x_j$$

$$y_k = \varphi(u_k + b_k)$$

where x_1, x_2, \dots, x_m are the input signals; $w_{k1}, w_{k2}, \dots, w_{km}$ are the synaptic weights of neuron k ; u_k is the linear combination output due to the input signals, b_k is the bias, $\varphi(\cdot)$ is the activation function, and y_k is the output signal of the neuron.

The manner in which the neurons of a neural network are structured is intimately linked with the learning algorithm used to train the network. Here we introduce some fundamentally different classes of architecture of neural networks.

1. Single-layer feed forward networks: In a layered neural network the neurons are organized in the form of layers. In the simplest form of layered network, we have an input layer of source nodes that projects onto an output layer of neurons. It is illustrated in Figure C.2 for the case of four nodes in both input and output layers.
2. Multilayer feed forward networks: In the multilayer network there are one or more hidden layers, whose computation nodes are correspondingly called hidden neurons. The function of hidden layer neurons is to intervene between the external input and network output in some useful manner. An example is shown in Figure C.3.
3. Recurrent networks: A recurrent neural network distinguishes itself from a feed forward neural network in that it has at least one feedback loop. For example, a recurrent network may consist of a single layer of neurons with each neuron feeding its output back to the inputs of all the other neurons, as illustrated in Figure C.4.

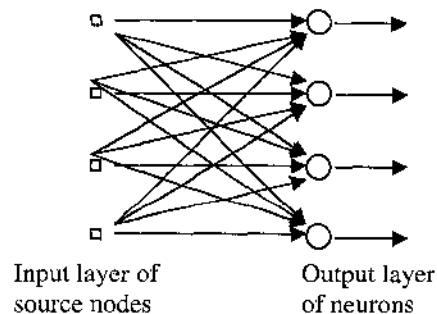


Figure C.2. Feed forward network with single layer of neurons.

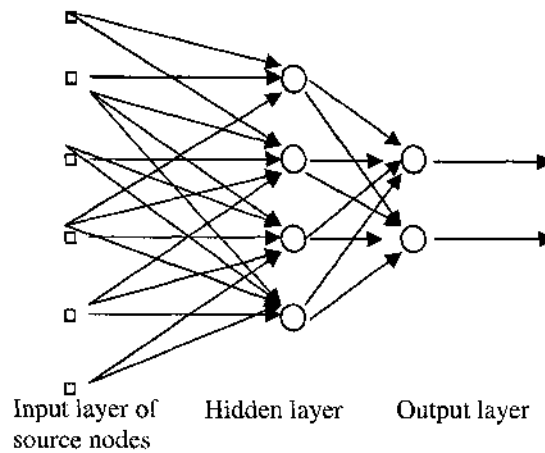


Figure C.3. Feed forward network with one hidden layer and one output layer.

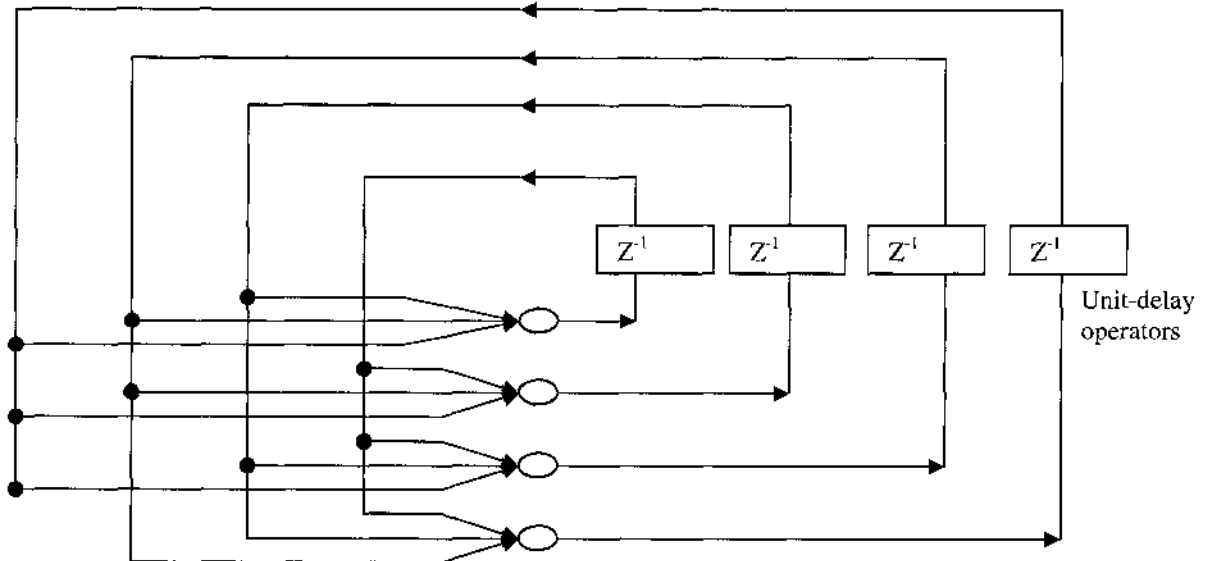


Figure C.4. Recurrent network.

The property that is of primary significance for a neural network is the ability of the network to learn from its environment and to improve its performance through learning. Learning is a process by which the free parameters of a neural network are adapted through a process of stimulation by the environment in which the network is embedded. The type of learning is determined by the manner in which the parameter changes take place. There is no unique learning algorithm. In fact, a great diverse variety of learning algorithms are implemented in practical applications. Learning algorithms fall into two broad categories: supervised learning, and unsupervised learning. The popular

supervised algorithms include perceptions, back propagation, least mean square error (LMS) algorithm and Radial basis function memory-based learning. The most used unsupervised learning algorithms are competitive learning and information-theoretic principles. Details can be found in related books.

Appendix D: Measured IPL Data

The following sections include IPL data from all four aircraft types (B737, B757, A319 and A320) for all systems of concern. Data for Vertical polarization is reported before horizontal polarization for each aircraft type. It is crucial to notice the polarizations noted in the first column of all tables (underlined). Each column includes the correction factors, IPL data, along with aircraft and system characteristics for each measurement. In order to use the recorded IPL data for further studies, one must add the total calibration value (recorded in the 7th row in the “Correction Factors” section) to the individual window IPL measurements. It is also critical to note that the recorded values represent pathloss and are therefore positive. If using the notation of coupling, then the final value to be used will need to be negated.

B737	ID	1989	1983	1983	1979	1981	1987	1994	1989	1983	1979	1981	1997
		GS	GS	GS (S)	GS	GS	GS	GS	GS	TCAS-I	TCAS	TCAS	TCAS
Correction Factors	System	15	15	15	0	0	0	0	15	0	0	0	0
	Pre-Amp	0	25	25	25	25	0	0	0	25	25	25	0
	TCL	-9.8	-9.8	-9.8	-2.8	-11.5	-5.5	-5.7	-9.8	-9.8	-8.5	-11.5	-11.53
	ACL	0	0	0	0	0	0	0	0	0	0	0	0
	PAR-Amp	0	0	0	0	0	0	0	0	0	0	0	0
	Tx-Gain	0.25	0.25	0.25	0.25	0.25	0.25	0.25	5.26	5.26	5.26	5.26	5.26
	Total	5.45	30.45	30.45	22.45	13.75	-5.35	-5.45	10.46	20.46	21.76	18.76	-6.27
	win 1	62.5	36.0	36.3	46.0	38.3	77.3	79.1	50.5	36.3	39.3	39.8	66.8
	win 2	61.8	36.2	34.7	49.0	41.8	73.8	78.7	47.8	36.5	40.2	42.0	65.8
	win 3	59.0	30.7	34.7	50.7	40.8	77.0	78.7	52.3	40.0	40.3	44.2	69.3
win 4	61.5	37.2	36.0	52.3	39.8	78.1	77.4	55.7	39.2	42.5	45.0	69.9	
win 5	60.3	40.0	34.0	54.5	41.7	79.8	77.8	53.2	39.0	42.7	46.8	72.0	
win 6	56.3	39.2	35.3	51.8	43.8	81.2	77.9	57.3	40.3	46.8	45.5	73.5	
win 7	56.5	38.0	36.5	53.2	40.3	81.4	81.3	58.2	38.0	46.2	52.8	74.1	
win 8	58.0	39.5	39.8	52.8	41.3	77.0	78.0	65.3	45.5	44.5	50.2	76.5	
win 9	63.2	41.8	40.5	52.3	42.3	77.6	79.5	55.5	45.0	45.0	53.8	82.0	
win 10	62.7	41.0	39.5	57.7	48.5	80.4	78.9	63.0	46.0	51.8	52.7	78.0	
win 11	61.8	38.5	41.2	54.0	49.0	81.0	73.7	58.3	45.5	49.7	55.5	83.6	
win 12	60.7	42.3	39.2	54.8	46.0	77.9	81.1	58.8	48.7	60.3	51.3	75.2	
win 13	61.0	42.7	36.8	58.2	42.8	81.8	83.4	58.8	45.5	50.2	52.5	76.9	
win 14	59.3	38.5	45.0	53.0	48.3	76.8	86.6	60.0	49.7	52.3	67.2	78.2	
win 15	62.7	42.0	38.3	58.5	46.3	79.3	78.2	58.3	48.8	53.7	57.5	77.7	
win 16	63.7	40.0	38.2	58.5	46.8	76.7	86.2	58.8	47.2	53.3	52.2	76.2	
win 17	68.8	45.2	43.3	57.7	52.3	81.3	86.5	58.5	44.5	51.0	55.2	80.0	
win 18	62.2	41.5	43.2	61.3	49.8	83.5	84.5	58.0	49.2	54.7	57.8	77.7	
win 19	62.7	39.8	44.0	57.8	49.7	79.6	81.8	62.2	52.3	57.3	63.7	79.9	
win 20	64.3	43.7	42.2	56.7	51.0	85.2	83.0	58.5	49.3	55.2	50.5	85.5	
win 21	63.3	38.7	44.0	58.7	51.0	84.0	83.4	62.7	50.3	55.5	56.7	80.0	
win 22	65.2	43.7	44.2	57.8	51.2	82.5	82.2	60.7	48.7	55.0	55.3	80.6	
win 23	67.2	44.2	45.5	56.8	52.0	85.1	86.0	64.9	50.0	65.2	53.8	84.1	
win 24	67.0	47.8	44.0	64.2	54.5	85.5	82.4	68.5	50.0	56.8	58.8	83.2	
win 25	68.3	45.8	38.0	57.8	53.5	82.1	93.4	68.0	51.3	66.5	60.0	83.1	
win 26	68.2	43.2	46.0	55.7	51.7	86.8	86.2	66.2	48.0	63.5	56.3	82.1	
win 27	69.3	40.8	44.7	58.2	52.0	84.5	87.0	63.2	50.8	64.2	58.8	88.5	
win 28	68.5	45.2	44.7	57.5	52.7	89.1	91.9	61.0	50.8	63.7	57.7	81.9	
win 29	68.5	47.7	46.7	61.2	54.7	82.4	87.5	64.2	49.2	62.5	64.5	82.2	
win 30	70.0	49.8	41.0	58.5	53.0	86.5	86.3	65.8	51.5	60.2	52.5	85.2	
win 31	67.2	47.7	44.5	62.7	52.5	87.8	91.4	68.8	52.5	54.8	59.0	86.9	
win 32	66.7	52.0	38.7	61.0	51.0	84.5	91.9	68.7	52.3	66.0	67.2	83.3	
win 33	68.5	51.8	38.7	63.0	52.7	85.6	89.5	68.0	56.7	66.0	61.0	83.5	
Aircraft Characteristics	Length	2954	2954	2954	2954	2954	2954	2954	2954	2954	2954	2954	2954
	Wins	33	33	33	33	33	33	33	33	33	33	33	33
	Exits	2	2	2	2	2	2	2	2	2	2	2	2
	Exit1	491	491	491	491	491	491	491	491	491	491	491	491
	Exit2	2333	2333	2333	2333	2333	2333	2333	2333	2333	2333	2333	2333
	Exit3	2333	2333	2333	2333	2333	2333	2333	2333	2333	2333	2333	2333
	Em Exits	1	1	1	1	1	1	1	1	1	1	1	1
	EmEx1	1250	1250	1250	1250	1250	1250	1250	1250	1250	1250	1250	1250
	EmEx2	1250	1250	1250	1250	1250	1250	1250	1250	1250	1250	1250	1250
	x-loc	200	200	200	200	200	200	200	680	680	680	680	680
y-loc	0	0	0	0	0	0	0	200.5	200.5	200.5	200.5	200.5	
start (Hz)	325	325	325	325	325	325	325	1080	1080	1080	1080	1080	
stop (Hz)	340	340	340	340	340	340	340	1100	1100	1100	1100	1100	
pol (v/n)	0	0	0	0	0	0	0	1	1	1	1	1	

B737: Vertical Polarization Data.

B737	Correction Factors											
	1994	1989	1989	1983	1983	1979	1981	1987	1994	1989	1989	1983
System	TCAS	VHF-1	VHF-1 (DI)	VHF-1	VHF-1 (DI)	VHF-1	VHF-1	VHF	VHF	LOC	LOC (DI)	LOC
Tx-Pwr	0	15	15	0	0	0	0	1.5	0	15	15	0
Pre-Amp	0	0	0	25	25	25	25	0	0	25	25	25
TCL	-11.2	-9.8	-9.8	-9.8	-9.8	-9.8	-1.7	-3.4	-3.2	-9.8	-9.8	-9.8
ACL	0	0	0	0	0	0	1.7	0	4.9	0	0	0
Pwr-Amp	0	0	0	0	0	0	0	0	0	0	0	0
Tx-Gain	8.26	0.05	-10.9	0.05	-10.9	0.05	0.05	0.05	0.05	1.25	-12.85	1.25
Total	-3.94	3.25	-3.7	15.25	4.3	25.55	23.35	3.05	-3.15	31.45	17.35	16.45
Window IPL Data (Vertical Polarization)												
win 1	68.8	54.3	59.7	47.7	46.3	40.0	44.0	69.1	74.9	45.5	51.5	52.8
win 2	68.9	57.3	63.3	50.0	47.7	40.3	46.8	70.4	72.1	48.8	52.5	53.5
win 3	67.8	53.8	61.5	47.2	49.3	41.3	37.3	74.2	78.0	49.5	49.0	63.8
win 4	71.8	61.5	62.8	44.8	45.7	45.3	42.3	66.7	73.8	49.0	52.3	64.0
win 5	75.3	55.5	62.3	48.7	43.5	42.7	42.8	70.9	73.1	50.5	52.7	60.0
win 6	72.8	55.7	60.0	46.0	48.2	44.5	42.8	69.7	73.7	50.7	50.8	63.2
win 7	76.8	57.0	58.0	46.2	43.5	41.3	33.3	69.6	71.1	45.0	44.7	56.2
win 8	81.7	59.0	57.7	43.3	43.7	44.0	38.8	70.8	70.0	48.3	55.5	63.3
win 9	75.1	59.2	55.3	39.7	41.8	35.8	38.3	70.7	69.2	39.7	54.2	63.0
win 10	79.9	59.5	60.2	39.0	42.8	39.2	36.7	72.4	70.4	41.5	49.0	59.3
win 11	77.0	55.2	57.3	40.8	39.8	37.0	37.0	65.6	65.5	48.2	52.3	60.7
win 12	82.4	54.2	56.0	39.7	39.3	41.3	37.3	66.4	69.8	45.0	59.7	60.0
win 13	79.5	49.8	56.3	40.3	34.3	37.5	32.8	64.1	68.1	59.2	59.3	54.5
win 14	75.9	51.2	53.5	38.5	38.3	38.0	37.3	63.9	67.6	49.8	51.0	46.3
win 15	66.1	43.7	51.0	36.7	33.0	33.2	34.3	58.3	64.1	50.3	54.2	61.3
win 16	82.6	44.3	53.3	39.2	31.0	30.8	28.5	56.2	63.0	40.0	56.3	56.5
win 17	76.4	47.5	53.5	37.5	34.0	35.7	39.5	63.2	65.3	49.2	47.0	64.0
win 18	80.5	45.8	52.2	38.0	36.0	35.8	35.2	62.7	61.6	48.7	47.7	61.8
win 18	82.6	50.7	52.5	39.0	38.0	37.0	41.5	66.5	67.9	41.2	47.7	61.0
win 20	81.3	48.0	52.2	39.2	36.3	37.8	39.7	66.9	69.2	52.0	46.2	55.7
win 21	85.5	47.3	53.3	39.8	39.5	35.8	36.0	62.7	67.4	43.3	45.0	56.2
win 22	82.7	53.8	54.7	40.7	40.5	39.8	41.2	71.8	70.6	39.5	47.3	55.0
win 23	82.2	53.8	58.5	41.7	39.2	43.0	35.5	65.0	68.4	51.7	55.0	55.3
win 24	81.0	55.8	56.6	42.5	41.5	43.2	40.8	67.8	72.1	48.0	45.7	54.3
win 25	83.9	57.5	58.3	42.3	44.3	44.2	45.0	74.8	75.9	44.8	44.2	56.8
win 26	85.7	56.2	58.8	42.0	41.3	40.7	36.5	63.5	74.0	41.0	45.5	52.0
win 27	80.8	55.3	64.2	47.8	46.8	43.3	41.7	74.3	74.9	41.0	45.0	52.2
win 28	80.0	56.5	60.7	48.8	47.0	44.5	41.0	77.8	74.5	50.2	47.7	56.1
win 29	85.4	63.3	59.5	47.2	40.7	39.3	43.2	69.8	73.1	41.8	43.7	49.8
win 30	88.9	56.3	62.0	49.2	41.3	43.8	48.3	69.7	72.3	37.8	42.5	53.6
win 31	81.5	60.0	60.8	45.2	44.0	49.7	42.7	71.4	74.5	45.7	46.5	52.0
win 32	82.1	59.8	59.5	48.0	43.5	47.2	41.3	72.0	78.8	46.2	45.7	48.0
win 33	89.0	43.2	62.7	45.5	37.8	43.7	45.7	70.9	70.3	37.0	44.5	62.7
Aircraft Characteristics												
Length	2954	2954	2954	2954	2954	2954	2954	2954	2954	2954	2954	2954
Wins	33	33	33	33	33	33	33	33	33	33	33	33
Exits	2	2	2	2	2	2	2	2	2	2	2	2
Exit1	491	491	491	491	491	491	491	491	491	491	491	491
Exit2	2333	2333	2333	2333	2333	2333	2333	2333	2333	2333	2333	2333
Exit3	2333	2333	2333	2333	2333	2333	2333	2333	2333	2333	2333	2333
Em Exits	1	1	1	1	1	1	1	1	1	1	1	1
EmEx1	1250	1250	1250	1250	1250	1250	1250	1250	1250	1250	1250	1250
EmEx2	1250	1250	1250	1250	1250	1250	1250	1250	1250	1250	1250	1250
x-loc	680	1250	1250	1250	1250	1250	1250	1250	1250	2900	2900	2900
y-loc	200.5	200.5	200.5	200.5	200.5	200.5	200.5	200.5	200.5	812.5	812.5	812.5
start (Hz)	1080	116	116	116	116	116	116	116	116	116	108	108
stop (Hz)	1100	138	138	138	138	138	138	138	138	138	118	118
pbl (V/m)	1	1	1	1	1	1	1	1	1	0	0	0

B737: Vertical Polarization Data (cont.).

B737		1879	1887	1897	1894	
Correction Factors	system	LOC	LOC	LOC	LOC	
	Tx-Pwr	0	0	0	0	
	Pre-Amp	25	25	0	0	
	TCL	-10.33	-11.5	-3.1	-2.9	
	ACL	0	0	0	0	
	Pwr-Amp	0	0	0	0	
	Tx-Gain	1.25	1.25	1.25	1.25	
	Total	15.92	14.75	-1.85	-1.65	
	win 1	86.8	65.8	90.3	96.2	
	win 2	52.8	59.8	91.7	97.9	
Window IPL Data (Vertical Polarization)	win 3	53.7	56.8	94.4	91.1	
	win 4	59.0	65.2	98.5	93.7	
	win 5	64.5	54.8	92.5	87.0	
	win 6	65.0	56.3	97.5	91.2	
	win 7	62.0	59.2	96.1	89.1	
	win 8	66.0	61.2	99.7	91.4	
	win 9	63.5	45.5	99.9	89.3	
	win 10	62.0	59.7	96.4	89.5	
	win 11	60.2	55.8	101.0	90.6	
	win 12	65.2	64.5	96.3	91.9	
	win 13	62.5	53.5	97.7	93.3	
	win 14	62.5	53.5	98.7	95.7	
	win 16	61.2	60.5	100.0	86.4	
	win 16	62.0	59.7	95.1	87.1	
	win 17	61.3	63.5	98.9	85.5	
	win 18	57.3	63.8	97.5	85.0	
	win 19	65.2	65.0	97.9	92.5	
	win 20	55.7	60.7	96.5	87.7	
	win 21	56.0	60.5	96.6	90.5	
	win 22	62.3	59.8	99.3	87.8	
	win 23	57.0	57.7	96.4	88.4	
	win 24	59.3	55.5	96.9	83.1	
	win 25	58.2	60.3	98.8	85.9	
	win 26	51.7	56.8	95.2	84.5	
	win 27	57.0	57.3	95.8	86.7	
	win 28	57.3	54.8	96.7	87.7	
	win 29	56.8	62.2	86.9	84.7	
	win 30	60.3	57.3	93.2	87.7	
	win 31	53.0	62.0	95.8	86.4	
	win 32	49.8	57.0	93.8	85.1	
	win 33	59.3	60.8	95.9	84.3	
	Aircraft Characteristics	Length	2954	2954	2954	2954
		Wins	33	33	33	33
Exits		2	2	2	2	
Exit1		491	491	491	491	
Exit2		2333	2333	2333	2333	
Exit3		2333	2333	2333	2333	
Em Exits		1	1	1	1	
EmEx1		1250	1250	1250	1250	
EmEx2		1250	1250	1250	1250	
x-loc		2900	2900	2900	2900	
y-loc	812.5	812.5	812.5	812.5		
start (Hz)	108	108	108	108		
stop (Hz)	118	118	118	118		
pot (Win)	0	0	0	0		

B737: Vertical Polarization Data (cont.).

B737	ID	1989	1993	1993	1979	1981	1987	1994	1989	1983	1979	1981	1997
		US	GS	GS (6)	GS	GS	GS	GS	TCAS-1	TCAS	TCAS	TCAS	TCAS
Correlation Factors	System	15	15	15	0	0	0	0	15	0	0	0	0
	Pwr-Amp	0	25	25	25	25	0	0	0	25	25	25	0
	TCL	-9.8	-9.8	-9.8	-2.8	-11.5	-5.6	-6.7	-9.8	-9.8	-8.5	-11.5	-11.83
	ACL	0	0	0	0	0	0	0	0	0	0	0	0
	Pwr-Amp	0	0	0	0	0	0	0	0	0	0	0	0
	Yx-Gain	0.25	0.25	0.25	0.25	0.25	0.25	0.25	5.26	5.26	5.26	5.26	5.26
	Total	5.45	30.45	30.45	22.45	13.75	-5.35	-5.45	10.46	20.46	21.76	18.76	-6.27
	Win 1	49.5	27.0	24.8	41.3	47.3	66.7	69.0	61.2	60.3	54.3	55.0	61.4
	Win 2	49.5	25.8	23.2	37.5	45.7	69.5	69.7	62.0	50.0	52.8	51.8	61.6
	Win 3	56.7	26.7	23.0	40.0	46.6	68.3	67.1	59.0	44.5	52.3	52.2	79.1
Win 4	53.2	29.3	29.0	47.7	49.3	71.5	67.8	56.8	46.8	52.0	62.3	78.2	
Win 5	54.0	28.5	29.2	45.2	51.3	68.9	70.4	59.0	46.7	47.5	52.0	82.0	
Win 6	53.5	27.0	27.7	45.3	52.8	69.8	71.7	65.3	46.8	55.5	63.3	85.2	
Win 7	51.8	32.0	26.8	49.0	47.3	72.9	71.4	63.8	49.3	51.2	63.3	82.7	
Win 8	54.7	31.0	27.0	45.7	50.8	74.9	69.5	63.8	45.7	50.7	63.7	81.9	
Win 9	53.7	33.0	28.5	47.3	47.8	70.5	73.0	62.7	49.5	51.3	44.3	78.5	
Win 10	55.7	34.0	31.7	51.0	52.0	73.2	68.7	58.0	49.3	48.3	54.0	80.8	
Win 11	58.8	33.8	31.3	52.3	54.5	76.1	76.2	63.0	49.3	53.2	62.6	78.1	
Win 12	55.3	34.7	29.5	49.2	57.2	74.2	74.5	62.7	47.8	51.3	62.7	76.7	
Win 13	57.6	37.0	28.7	49.8	52.2	74.0	75.1	60.7	48.8	50.2	63.2	79.1	
Win 14	57.2	35.8	29.0	47.5	55.3	70.5	76.0	60.5	48.8	49.7	49.5	80.3	
Win 15	57.0	32.2	28.3	51.8	51.7	70.6	77.9	60.8	49.2	50.0	51.8	81.0	
Win 16	59.5	35.5	31.2	50.3	53.8	76.4	76.0	58.0	46.8	46.6	51.5	78.6	
Win 17	55.8	36.3	32.7	51.3	54.8	77.1	78.9	57.2	48.3	50.3	47.7	77.4	
Win 18	58.8	34.7	34.0	52.5	54.2	75.0	74.7	61.0	50.2	50.5	52.0	79.2	
Win 19	61.5	37.0	33.7	51.2	53.8	76.0	78.0	60.8	48.5	48.2	60.7	80.6	
Win 20	55.8	35.7	36.5	52.8	54.8	76.8	78.1	62.5	49.2	54.7	51.8	80.9	
Win 21	58.3	36.3	31.2	53.3	55.3	79.6	78.5	63.2	47.8	52.3	47.5	77.1	
Win 22	60.0	40.2	35.3	53.3	56.8	78.0	79.2	62.8	49.0	52.2	52.0	79.3	
Win 23	62.2	38.2	34.8	52.0	61.5	74.9	79.4	61.3	58.5	49.2	50.8	80.3	
Win 24	56.5	35.7	33.2	53.2	59.8	77.0	81.3	64.2	49.3	50.5	51.8	80.2	
Win 25	58.3	40.0	36.5	56.5	57.2	78.2	79.2	63.0	50.7	61.7	55.3	82.9	
Win 26	61.3	40.0	36.5	54.7	59.0	77.9	78.1	62.0	52.8	52.7	52.0	80.6	
Win 27	61.5	38.7	36.2	54.2	56.2	76.1	81.9	63.0	50.2	52.2	62.2	82.4	
Win 28	61.7	41.0	37.7	52.3	67.8	73.8	81.5	61.7	62.2	53.7	56.3	79.2	
Win 29	62.0	39.0	36.8	56.8	57.3	76.3	79.9	64.3	50.0	53.3	54.5	80.4	
Win 30	62.7	38.3	39.0	54.3	57.5	79.2	80.4	65.0	53.0	56.5	54.8	84.3	
Win 31	64.8	42.2	38.7	55.3	57.7	77.1	82.6	62.2	52.8	48.8	48.0	82.4	
Win 32	64.8	40.5	38.7	53.8	58.5	77.4	81.7	60.2	52.7	62.7	62.8	84.7	
Win 33	64.8	41.3	38.7	56.3	64.0	80.3	84.8	63.0	50.8	55.3	60.7	82.1	
Aircraft Characteristics	Length	2954	2954	2954	2954	2954	2954	2954	2954	2954	2954	2954	2954
	Wins	33	33	33	33	33	33	33	33	33	33	33	33
	Exits	2	2	2	2	2	2	2	2	2	2	2	2
	Exit1	491	491	491	491	491	491	491	491	491	491	491	491
	Exit2	2333	2333	2333	2333	2333	2333	2333	2333	2333	2333	2333	2333
	Exit3	2333	2333	2333	2333	2333	2333	2333	2333	2333	2333	2333	2333
	Em Exits	1	1	1	1	1	1	1	1	1	1	1	1
	EmEx1	1250	1250	1250	1250	1250	1250	1250	1250	1250	1250	1250	1250
	EmEx2	1250	1250	1250	1250	1250	1250	1250	1250	1250	1250	1250	1250
	X-loc	200	200	200	200	200	200	200	680	680	680	680	680
Y-loc	0	0	0	0	0	0	0	200.5	200.5	200.5	200.5	200.5	
start (Hz)	325	325	325	325	325	325	325	1080	1080	1080	1080	1080	
stop (Hz)	340	340	340	340	340	340	340	1100	1100	1100	1100	1100	
por (win)	0	0	0	0	0	0	0	1	1	1	1	1	

B737: Horizontal Polarization Data.

B737	ID	1984	1989	1989	1989	1989	1879	1881	1997	1994	1989	1989	1989	
		System	TCAS	VHF-1	VHF-1 (B)	VHF-1	VHF-1 (B)	VHF-1	VHF-1	VHF	VHF	LOC	LOC (B)	LOC
Correction Factors	Tx-Pwr	0	15	15	0	0	0	0	1.5	0	15	15	0	
	Pre-Amp	0	0	0	25	25	25	25	0	0	25	25	25	
	TCL	-11.2	-9.8	-9.8	-9.8	-9.8	-0.2	-1.7	-3.4	-3.2	-9.8	-9.8	-9.8	
	ACL	0	0	0	0	0	1.7	0	4.9	0	0	0	0	
	Pwr-Amp	0	0	0	0	0	0	0	0	0	0	0	0	
	Tx-Gain	5.26	0.05	-10.9	0.05	-10.9	0.05	0.05	0.05	0.05	0.05	1.25	-12.85	1.25
	Total	-5.94	5.26	-5.7	15.25	4.3	26.55	23.35	3.05	-3.15	31.45	17.35	16.45	
	win 1	84.7	48.1	53.3	36.7	37.2	31.5	32.8	61.9	64.3	36.7	40.5	47.8	
	win 2	83.4	48.7	57.3	39.0	36.7	35.5	31.8	63.2	63.1	32.7	37.7	46.5	
	win 3	86.0	48.2	55.8	38.8	36.3	35.3	33.8	60.6	65.8	32.3	37.7	44.7	
win 4	82.0	46.8	58.0	38.3	36.7	36.7	33.5	59.3	64.8	30.5	41.3	42.5		
win 5	83.2	47.8	53.2	35.7	34.3	35.2	36.0	58.7	63.4	32.2	38.8	42.3		
win 6	82.3	45.8	52.5	37.2	35.8	35.2	32.8	56.6	65.9	32.5	39.0	42.7		
win 7	81.9	48.2	55.8	37.0	35.5	33.0	33.3	58.2	62.3	30.5	37.7	44.8		
win 8	84.2	47.0	52.3	38.2	35.7	31.7	38.7	56.2	62.6	33.8	41.3	44.7		
win 9	79.4	47.5	53.0	38.2	31.8	33.8	34.8	56.5	61.7	26.8	35.7	40.8		
win 10	79.0	49.0	51.8	40.0	30.8	35.3	37.0	57.2	63.7	29.0	36.2	40.7		
win 11	77.5	46.7	53.8	36.7	36.0	30.5	35.8	64.4	64.6	28.2	35.7	40.2		
win 12	79.2	48.3	53.3	40.8	32.7	37.2	33.0	59.1	64.1	28.5	34.8	39.2		
win 13	78.7	49.6	52.5	42.3	35.3	39.0	36.2	61.4	65.4	31.0	38.8	38.0		
win 14	77.0	49.0	55.8	42.0	41.0	40.3	39.0	58.6	64.4	32.2	39.5	38.7		
win 15	79.3	49.0	51.0	47.2	42.0	35.5	40.7	62.6	64.2	30.5	40.8	36.3		
win 16	77.0	60.7	56.0	56.3	38.5	42.7	41.6	65.1	72.7	25.0	40.8	32.3		
win 17	79.3	51.7	59.7	43.5	41.8	42.3	45.5	66.5	70.8	42.0	39.0	38.5		
win 18	82.3	48.2	52.8	40.5	40.3	40.3	39.0	64.0	68.1	35.3	37.2	40.2		
win 19	81.8	47.8	52.8	43.3	36.2	36.3	38.3	59.6	66.0	35.2	44.7	43.8		
win 20	84.8	55.0	59.0	37.7	33.3	35.3	36.0	62.0	64.0	33.8	44.2	40.2		
win 21	82.4	47.3	50.8	39.0	35.7	35.7	35.5	58.5	65.8	35.2	38.2	38.8		
win 22	81.5	45.3	48.7	38.7	31.8	35.3	33.5	60.1	64.5	34.5	39.7	38.7		
win 23	80.9	47.7	49.3	38.7	35.2	35.8	36.0	63.7	62.8	36.7	43.0	37.7		
win 24	81.9	44.0	48.8	36.5	34.3	34.7	33.3	57.8	62.5	35.7	42.5	40.8		
win 25	81.1	45.2	50.5	38.7	30.7	33.5	36.2	57.0	62.8	33.3	39.3	38.0		
win 26	80.1	44.3	50.5	40.2	32.0	33.2	32.7	59.1	61.2	36.2	43.0	38.2		
win 27	78.9	45.7	49.2	38.2	35.5	36.3	34.3	56.9	64.1	36.8	42.7	39.2		
win 28	79.4	48.7	50.7	37.3	34.5	34.8	32.7	60.3	61.9	35.0	40.8	36.8		
win 29	80.6	45.3	50.5	35.3	34.7	33.3	31.6	61.8	63.4	33.0	36.0	36.5		
win 30	82.9	48.0	50.2	38.7	32.7	32.3	36.3	61.4	59.5	30.8	39.0	37.7		
win 31	84.4	44.0	50.7	37.3	34.7	34.2	35.5	57.6	63.5	34.0	40.3	36.5		
win 32	84.0	43.2	49.5	37.8	31.8	32.7	31.8	55.5	60.9	30.0	37.0	37.5		
win 33	81.8	43.2	50.0	38.5	34.8	37.0	34.8	64.6	64.6	34.2	37.3	36.0		
Aircraft Characteristics	Length	2954	2954	2954	2954	2954	2954	2954	2954	2954	2954	2954	2954	
	Wins	33	33	33	33	33	33	33	33	33	33	33	33	
	Exits	2	2	2	2	2	2	2	2	2	2	2	2	
	Exit1	491	491	491	491	491	491	491	491	491	491	491	491	
	Exit2	2333	2333	2333	2333	2333	2333	2333	2333	2333	2333	2333	2333	
	Exit3	2333	2333	2333	2333	2333	2333	2333	2333	2333	2333	2333	2333	
	Em Exits	1	1	1	1	1	1	1	1	1	1	1	1	
	EmEx1	1250	1250	1250	1250	1250	1250	1250	1250	1250	1250	1250	1250	
	EmEx2	1250	1250	1250	1250	1250	1250	1250	1250	1250	1250	1250	1250	
	x-loc	680	1250	1250	1250	1250	1250	1250	1250	1250	2500	2500	2900	
y-loc	200.5	200.5	200.5	200.5	200.5	200.5	200.5	200.5	200.5	200.5	812.5	812.5	812.5	
start (Hz)	1080	116	116	116	116	116	116	116	116	116	108	108		
stop (Hz)	1100	138	138	138	138	138	138	138	138	138	118	118		
pol (v/n)	1	1	1	1	1	1	1	1	1	0	0	0		

B737: Horizontal Polarization Data (cont.).

B737		1879	1881	1997	1994	
Correction Factors	System	LOC	LOC	LOC	LOC	
	Rx-Pwr	0	0	0	0	
	Pre-Amp	25	25	0	0	
	YCL	-10.33	-11.5	-3.1	-2.9	
	ACL	0	0	0	0	
	Pwr-Amp	0	0	0	0	
	Rx-Gain	1.25	1.25	1.25	1.25	
	Total	15.92	14.75	-1.85	-1.65	
	win 1	56.7	49.8	87.7	76.5	
	win 2	54.0	48.0	87.4	76.6	
Window PL Data (Horizontal Polarization)	win 3	51.3	49.2	85.0	77.3	
	win 4	49.2	45.3	91.1	77.9	
	win 5	56.7	47.3	87.3	76.6	
	win 6	50.0	46.3	85.5	76.2	
	win 7	54.0	49.3	87.8	79.3	
	win 8	50.3	50.5	87.2	74.0	
	win 9	49.0	46.0	83.8	73.5	
	win 10	49.5	47.7	84.6	75.4	
	win 11	47.2	50.2	83.9	75.2	
	win 12	45.6	45.3	84.3	74.2	
	win 13	45.3	46.2	85.5	72.4	
	win 14	45.8	48.3	84.1	71.9	
	win 15	44.3	47.0	83.6	71.4	
	win 16	46.8	52.0	85.0	75.8	
	win 17	50.3	56.0	95.1	80.4	
	win 18	46.0	50.3	87.5	76.9	
	win 19	46.7	50.3	88.2	76.1	
	win 20	47.7	52.7	89.1	78.7	
	win 21	46.8	55.3	87.5	77.3	
	win 22	44.2	51.2	86.8	76.3	
	win 23	45.2	51.8	88.4	78.0	
	win 24	44.8	51.5	87.7	76.5	
	win 25	46.7	50.3	88.6	78.8	
	win 26	46.0	51.7	88.4	76.7	
	win 27	46.3	54.5	88.2	79.9	
	win 28	43.8	49.5	86.9	75.8	
	win 29	41.7	46.3	84.5	73.0	
	win 30	39.5	49.3	84.4	73.3	
	win 31	41.5	46.7	87.0	76.4	
	win 32	41.3	46.3	84.2	73.0	
	win 33	38.0	49.7	83.1	68.5	
	Aircraft Characteristics	Length	2954	2954	2954	2954
		Wins	33	33	33	33
Exits		2	2	2	2	
Exit1		491	491	491	491	
Exit2		2333	2333	2333	2333	
Exit3		2333	2333	2333	2333	
Em Exits		1	1	1	1	
EmEx1		1250	1250	1250	1250	
EmEx2		1250	1250	1250	1250	
x-loc		2900	2900	2900	2900	
y-loc	812.5	812.5	812.5	812.5		
start (Hz)	108	108	108	108		
stop (Hz)	118	118	118	118		
pot (V/m)	0	0	0	0		

B737: Horizontal Polarization Data (cont.).

		B757		
		ID	660	6707
Correction Factors		System	VOR-L	VOR-L
	ICP/W	0	0	-20
	Freq Amp	0	0	0
	ICL	-5.82	-5.55	-5.5
	ACL	0	0	0
	PWR/Amp	31	37	37
	IC Gain	-12.85	-12.85	-12.85
	Total	12.3	18.6	-1.4
Window IPL Data (Vertical Polarization)		win 1	88.3	80.0
		win 2	85.3	82.3
		win 3	84.0	85.1
		win 4	81.9	85.7
		win 5	87.8	82.1
		win 6	85.1	85.7
		win 7	85.8	88.5
		win 8	88.1	84.4
		win 9	85.5	82.5
		win 10	85.1	86.0
		win 11	84.6	87.4
		win 12	82.7	89.3
		win 13	85.8	89.4
		win 14	80.9	83.2
		win 15	83.7	85.5
		win 16	81.8	85.8
		win 17	80.3	89.5
		win 18	86.8	82.0
		win 19	87.0	85.8
		win 20	88.7	89.5
		win 21	84.1	88.8
		win 22	87.4	87.5
		win 23	89.0	86.6
		win 24	84.9	84.4
		win 25	89.0	88.5
		win 26	82.0	87.4
		win 27	84.5	88.7
		win 28	80.3	87.5
		win 29	85.9	88.8
		win 30	84.6	88.5
		win 31	87.2	82.0
		win 32	86.5	84.6
		win 33	82.9	83.6
		win 34	88.3	84.5
		win 35	80.9	81.2
		win 36	83.9	80.6
		win 37	89.6	87.7
		win 38	88.3	84.6
		win 39	80.2	85.4
		win 40	82.5	88.9
		win 41	89.8	83.8
		win 42	83.0	87.0
		win 43	84.9	82.7
		win 44	82.8	83.0
		win 45	85.1	80.8
		win 46	85.7	88.4
		win 47	80.8	80.6
		win 48	80.5	84.7
		win 49	86.2	84.9
		win 50	89.4	84.7
		win 51	87.9	84.5
		win 52	88.0	85.3
		win 53	83.9	84.0
Aircraft Characteristics		Length	1697	1697
	Wings	53	50	53
	Exits	3	3	3
	EXRT	580	686	580
	EXRZ	7400	14100	14800
	EXR3	4127	4127	4127
	Em Exit6	2	2	2
	EMEXIT	2036	2036	2036
	EMEX2	2080	2088	2080
	X-loc	4600	4800	4600
	Y-loc	931.5	931.5	931.5
	start (Hz)	108	108	108
	stop (Hz)	118	118	118
	pos (V/M)	U	U	U

B757: Vertical Polarization Data (cont.).

		B757		
	U	894	880	8407
	System	VOR	VOR-L	VOR-L
Correction Factors				
	Pre-Amp	0	0	0
	TCL	-5.82	-5.55	-5.5
	ACL	0	0	0
	Post-Amp	31	37	37
	TX Gain	-12.85	-12.85	-12.85
	Total	12.5	18.6	17.4
Window IPL Data (Horizontal Polarization)				
win 1	58.3	51.5	74.2	
win 2	57.8	51.7	75.0	
win 3	52.6	52.4	71.9	
win 4	55.2	50.0	71.4	
win 5	57.0	49.3	77.0	
win 6	54.8	52.5	69.2	
win 7	56.3	51.5	72.4	
win 8	53.7	53.3	72.4	
win 9	55.4	52.6	70.3	
win 10	56.2	54.4	80.9	
win 11	54.7	49.2	73.8	
win 12	54.7	52.2	74.6	
win 13	53.0	51.6	75.2	
win 14	51.0	50.2	73.7	
win 15	53.8	52.4	72.5	
win 16	53.2	47.5	73.8	
win 17	50.3	48.5	72.3	
win 18	52.2	49.8	65.1	
win 19	53.1	48.4	68.3	
win 20	55.7	46.0	67.9	
win 21	53.7	43.9	73.3	
win 22	48.5	40.2	63.5	
win 23	43.1	43.5	63.4	
win 24	45.4	45.0	68.3	
win 25	34.7	50.9	75.0	
win 26	47.1	46.9	72.3	
win 27	50.1	46.9	79.1	
win 28	50.6	47.6	69.2	
win 29	53.8	51.7	71.6	
win 30	55.1	45.5	75.0	
win 31	54.1	46.1	74.1	
win 32	50.7	47.6	79.0	
win 33	55.9	48.7	73.4	
win 34	54.6	48.1	74.8	
win 35	54.4	43.1	77.9	
win 36	53.9	45.0	69.2	
win 37	50.2	44.7	72.5	
win 38	49.0	43.1	75.7	
win 39	57.4	49.0	71.6	
win 40	53.7	50.0	75.8	
win 41	54.0	43.4	72.7	
win 42	54.4	45.6	70.2	
win 43	54.1	51.5	70.9	
win 44	54.3	46.8	74.8	
win 45	52.0	51.7	75.8	
win 46	55.5	53.9	72.1	
win 47	55.7	46.8	75.7	
win 48	48.1	49.5	72.9	
win 49	57.9	43.5	75.4	
win 50	54.5	45.3	82.2	
win 51	52.1	45.3	74.3	
win 52	55.1	45.3	72.6	
win 53	45.9	45.3	75.3	
Aircraft Characteristics				
Langth	4697	4697	4697	
Wings	53	50	53	
EX19	3	3	3	
EX11	580	580	580	
EX12	1400	1400	1400	
EX13	4127	4127	4127	
Em. Freqs	2	2	2	
EMEX1	2036	2036	2036	
EMEX2	2080	2080	2080	
xloc	4600	4600	4600	
yloc	931.5	931.5	931.5	
start (Hz)	108	108	108	
stop (Hz)	118	118	115	
por (v/n)	U	U	U	

B757: Horizontal Polarization Data (cont.).

A319		807	807	807	807	
Correction Factors	System	VHF-R(P)	VHF-R(S)	VHF-C(P)	VHF-C(S)	
	Tx-Pwr	-10	-10	-10	-10	
	Pre-Amp	0	0	0	0	
	TCL	-5.2	-5.2	-5.2	-5.2	
	ACL	0	0	0	0	
	Pwr-Amp	37	37	37	37	
	Tx-Gain	-10.9	-10.9	-10.9	-10.9	
	Total	10.9	10.9	10.9	10.9	
	Window IPL Data (Vertical Polarization)	win 1	53.2	56.2	51.3	50.8
		win 2	58.9	62.0	53.5	54.9
win 3		57.3	58.7	53.5	50.0	
win 4		61.4	62.5	55.7	57.1	
win 5		58.5	58.1	51.9	53.3	
win 6		62.4	58.8	55.8	53.7	
win 7		60.7	57.1	50.5	57.1	
win 8		62.3	63.9	56.6	57.0	
win 9		57.4	58.9	50.1	49.2	
win 10		60.8	59.1	52.2	53.0	
win 11		59.2	57.9	57.0	53.9	
win 12		64.9	57.5	52.7	45.6	
win 13		57.8	58.4	46.6	44.8	
win 14		57.9	55.7	47.5	41.8	
win 15		60.8	57.8	56.8	49.5	
win 16		53.8	52.5	54.6	51.2	
win 17		48.6	49.5	53.0	47.0	
win 18		47.4	52.3	49.9	49.3	
win 19		48.8	50.8	52.7	47.3	
win 20		47.6	51.3	45.5	45.7	
win 21		51.2	53.8	42.6	46.9	
win 22		55.6	53.2	46.0	44.0	
win 23		50.6	50.1	45.3	44.2	
win 24		49.4	49.0	45.7	43.5	
win 25		54.1	51.1	50.5	46.7	
win 26		50.1	52.1	45.6	45.4	
win 27		48.0	53.4	46.3	44.8	
win 28		48.0	54.5	51.0	49.3	
win 29		50.1	49.5	48.8	45.1	
win 30		45.7	46.9	46.5	46.5	
Aircraft Characteristics	Length	3383	3383	3383	3383	
	Wins	32	32	32	32	
	Exite	2	2	2	2	
	Exit1	767	767	767	767	
	Exit2	2810	2810	2810	2810	
	Exit3	2810	2810	2810	2810	
	Em Exite	1	1	1	1	
	EmEx1	1604	1604	1604	1604	
	EmEx2	1604	1604	1604	1604	
	x-loc	2003	2003	2056	2056	
	y-loc	-206.8	-206.8	206.8	206.8	
start (Hz)	116	116	116	116		
stop (Hz)	138	138	138	138		
pol (v/h)	1	1	1	1		

A319: Vertical Polarization Data (cont.).

ID	807	807	807	807
	VHF-R(P)	VHF-R(S)	VHF-C(P)	VHF-C(S)
System	-10	-10	-10	-10
Tx-Pwr	0	0	0	0
Pre-Amp	0	0	0	0
TCL	-5.2	-5.2	-5.2	-5.2
ACL	0	0	0	0
Pwr-Amp	37	37	37	37
Tx-Gain	-10.9	-10.9	-10.9	-10.9
Total	10.9	10.9	10.9	10.9
win 1	48.8	52.6	42.0	44.9
win 2	51.3	55.1	44.1	41.0
win 3	47.0	52.4	39.7	40.2
win 4	56.9	56.3	48.5	45.6
win 5	55.4	49.1	43.2	44.7
win 6	58.0	52.3	49.6	42.2
win 7	55.9	52.3	41.4	41.2
win 8	58.0	60.1	45.5	39.3
win 9	52.6	53.5	41.8	39.7
win 10	52.2	52.4	42.7	46.5
win 11	54.4	61.1	50.0	47.3
win 12	56.7	56.6	44.4	41.9
win 13	46.5	37.9	31.4	23.0
win 14	49.0	44.1	37.5	30.7
win 15	51.3	53.5	48.4	43.8
win 16	51.0	49.3	46.5	45.4
win 17	46.4	47.6	44.0	42.1
win 18	48.5	48.7	46.7	43.5
win 19	45.8	51.7	48.6	42.3
win 20	48.0	47.2	41.7	44.6
win 21	46.5	48.5	45.8	49.5
win 22	50.9	51.2	45.7	44.8
win 23	47.7	48.9	47.1	46.3
win 24	48.7	50.7	47.2	44.1
win 25	48.5	54.0	48.2	46.5
win 26	46.4	50.2	41.1	41.8
win 27	45.8	47.5	40.8	39.9
win 28	54.7	47.9	45.5	44.2
win 29	42.7	45.7	39.9	39.4
win 30	43.4	41.7	41.2	37.9
Length	3383	3383	3383	3383
Wins	32	32	32	32
Exits	2	2	2	2
Exit1	767	767	767	767
Exit2	2810	2810	2810	2810
Exit3	2810	2810	2810	2810
Em Exits	1	1	1	1
EmEx1	1604	1604	1604	1604
EmEx2	1604	1604	1604	1604
x-loc	2003	2003	2056	2056
y-loc	-206.8	-206.8	206.8	206.8
start (Hz)	116	116	116	116
stop (Hz)	138	138	138	138
pol (v/h)	1	1	1	1

A319. Horizontal Polarization Data (cont.).

A320	ID	477		493		477		467		481		481	
		GS(P)	GS(S)	LOC(P)	LOC(S)	DME-R(P)	DME-R(S)	VHF-L(P)	VHF-L(S)	AIC-L(P)	AIC-L(S)	AIC-B(P)	AIC-B(S)
Correction Factors	System	-10	-10	-10	-10	-10	-10	-10	-10	-10	-10	-10	-10
	Pre-Amp	0	0	0	0	0	0	0	0	0	0	0	
	TCL	-8.8	-8.8	-4.9	-4.9	-15.7	-15.7	-5.2	-5.2	-16.4	-16.4	-16.4	-16.4
	ACL	0	0	0	0	0	0	0	0	0	0	0	
	Pwr-Amp	37	37	37	37	37.5	37.5	37	37	37.5	37.5	37.5	37.5
	Tx-Gain	1.03	1.03	-12.85	-12.85	5.32	5.32	-10.9	-10.9	4.85	4.85	4.85	4.85
	Total	19.23	19.23	9.25	9.25	17.12	17.12	10.9	10.9	15.95	15.95	15.95	15.95
Window IPL Data (Vertical Polarization)	win 1	51.5	51.9	62.0	63.6	46.0	49.4	45.1	42.4	43.0	52.2	50.5	49.3
	win 2	50.4	52.6	62.2	66.0	44.2	50.0	45.9	48.8	45.8	61.8	49.7	43.6
	win 3	51.7	53.0	70.0	72.3	54.0	47.3	46.0	46.3	41.1	53.5	50.6	46.1
	win 4	49.6	53.1	70.0	72.1	46.9	48.6	46.3	53.6	41.3	53.0	50.9	47.0
	win 5	51.5	48.8	77.0	75.2	46.9	47.5	47.7	52.9	44.1	54.6	50.6	45.0
	win 6	54.1	53.1	71.3	69.0	49.4	46.6	53.0	52.2	47.4	61.7	51.2	45.4
	win 7	49.9	54.8	76.6	71.3	50.2	50.0	55.7	53.2	49.7	55.4	48.0	45.2
	win 8	52.1	53.2	76.1	79.6	52.7	48.8	47.8	52.4	48.2	54.1	56.1	45.8
	win 9	54.2	51.6	81.0	67.5	52.5	49.4	54.1	59.4	55.2	56.1	51.2	46.6
	win 10	53.3	53.9	79.8	70.0	53.2	50.6	49.4	55.1	54.1	62.1	48.4	49.2
	win 11	51.7	53.4	77.5	72.1	61.8	49.3	56.8	56.7	54.8	56.7	50.4	46.7
	win 12	53.7	50.2	77.4	73.0	51.2	49.9	55.3	53.5	49.7	56.5	56.0	52.2
	win 13	53.3	52.0	70.7	69.8	52.4	51.2	52.3	50.0	50.2	57.8	56.2	47.5
	win 14	56.8	55.5	82.4	72.0	49.3	51.6	53.8	54.7	53.1	56.5	51.9	47.9
	win 15	61.2	53.0	77.4	77.0	49.2	53.7	60.0	52.6	50.2	59.7	57.6	47.3
	win 16	54.9	59.6	74.3	64.6	51.8	53.7	47.0	48.4	47.0	55.6	55.7	49.5
	win 17	57.2	61.1	75.2	65.1	51.6	53.8	51.2	54.1	50.5	56.8	57.6	48.6
	win 18	58.8	56.1	83.2	77.3	50.7	54.9	52.0	56.4	53.4	58.3	58.4	53.3
	win 19	60.4	56.7	75.7	75.7	53.8	55.9	48.3	53.5	51.1	59.3	60.5	56.9
	win 20	58.1	58.8	69.9	71.1	51.4	57.2	53.0	57.9	48.3	62.1	56.3	53.2
	win 21	56.3	60.8	79.3	75.4	53.6	55.1	54.0	54.8	54.7	63.2	58.5	57.3
	win 22	58.3	57.7	79.6	79.3	54.3	58.2	59.3	56.5	54.0	58.4	57.8	55.5
	win 23	61.8	62.1	74.4	78.3	50.4	57.6	56.2	56.8	51.4	58.4	57.1	56.0
	win 24	62.5	57.7	79.4	74.3	53.7	56.8	54.9	56.2	56.5	61.4	60.8	59.2
	win 25	54.9	58.3	82.5	82.2	53.6	60.0	64.7	59.0	56.7	58.5	58.2	53.2
	win 26	56.7	60.0	83.4	85.6	54.2	57.3	58.6	57.0	55.1	57.8	59.0	57.0
	win 27	64.3	54.7	82.9	81.5	55.8	57.3	56.1	57.4	62.1	60.3	58.4	57.1
	win 28	60.0	63.1	94.0	82.7	53.8	60.9	69.7	56.9	58.5	61.7	62.2	56.5
	win 29	60.0	54.6	86.4	80.4	53.5	57.8	57.9	57.5	57.1	63.2	60.5	53.2
	win 30	62.0	56.1	83.4	75.9	56.8	57.8	55.8	56.5	59.6	60.1	62.6	56.5
	win 31	66.8	60.0	79.9	83.7	56.1	57.6	55.2	66.2	59.5	63.0	64.7	59.9
	win 32	63.2	57.4	83.5	78.9	56.5	57.6	53.5	60.7	55.5	60.6	63.5	55.9
	win 33	58.5	56.5	76.9	75.3	65.5	59.1	55.1	56.5	56.3	62.5	60.8	59.5
	win 34	60.5	58.6	80.1	82.7	56.7	58.7	55.3	56.8	55.2	61.7	63.8	56.4
	win 35	62.0	63.9	79.2	78.5	57.8	60.0	59.9	56.9	58.0	59.6	60.6	54.8
	win 36	56.7	59.9	85.2	82.0	55.8	59.1	56.2	56.1	56.3	66.5	59.3	53.8
	win 37	63.2	61.4	85.0	84.1	55.7	61.8	56.7	56.7	55.4	64.1	59.6	54.4
	win 38	62.4	56.2	82.5	84.5	56.9	62.4	64.3	58.1	58.6	66.5	57.8	56.3
	win 39	60.5	63.3	80.1	79.8	53.9	61.4	57.7	57.7	55.9	63.0	59.6	56.5
	win 40	61.8	59.9	92.7	81.4	52.3	61.6	52.6	58.4	55.1	63.2	57.7	57.5
Aircraft Characteristics	Length	3750	3750	3750	3750	3750	3750	3750	3750	3750	3750	3750	3750
	Wings	40	40	40	40	40	40	40	40	40	40	40	40
	Exits	2	2	2	2	2	2	2	2	2	2	2	2
	Exit1	780	780	780	780	780	780	780	780	780	780	780	780
	Exit2	3050	3050	3050	3050	3050	3050	3050	3050	3050	3050	3050	3050
	Exit3	3050	3050	3050	3050	3050	3050	3050	3050	3050	3050	3050	3050
	Em Exits	2	2	2	2	2	2	2	2	2	2	2	2
	EmEx1	1002	1002	1002	1002	1002	1002	1002	1002	1002	1002	1002	1002
	EmEx2	1709	1709	1709	1709	1709	1709	1709	1709	1709	1709	1709	1709
	x-loc	200	200	200	200	400	400	811	811	920	920	870	870
y-loc	-113	-113	0	0	-206.8	-206.8	206.8	206.8	206.8	206.8	-206.8	-206.8	
start (Hz)	325	325	108	108	960	960	116	116	1020	1020	1020	1020	
stop (Hz)	340	340	113	113	1215	1215	138	138	1040	1040	1040	1040	
pol (v/h)	0	0	0	0	1	1	1	1	1	1	1	1	

A320: Vertical Polarization Data.

A320	ID	467	467	493	493
	System	GPS(P)	GPS(S)	VHF-C(P)	VHF-L(S)
Correction Factors	Tx-Pwr	-30	-30	-10	-10
	Pre-Amp	0	0	0	0
	TCL	-21.4	-21.4	-5.2	-5.2
	ACL	0	0	0	0
	Pwr-Amp	37	37	37	37
	Tx-Gain	7.5	7.5	-10.9	-10.9
	Total	-6.9	-6.9	10.9	10.9
	win 1	82.7	71.3	63.2	60.8
	win 2	76.9	70.5	62.0	64.6
	win 3	71.6	74.2	64.2	64.5
win 4	75.3	73.1	56.7	67.7	
win 5	77.6	74.0	57.5	67.4	
win 6	76.9	73.3	63.0	62.5	
win 7	79.0	76.1	71.1	56.6	
win 8	82.6	71.8	61.5	64.7	
win 9	78.5	73.3	66.6	67.7	
win 10	80.1	72.9	60.6	57.6	
win 11	82.2	74.2	58.1	62.2	
win 12	81.3	74.4	61.7	60.3	
win 13	80.6	76.6	60.7	66.2	
win 14	81.4	75.6	56.7	66.3	
win 15	80.9	75.2	48.1	52.2	
win 16	78.6	71.2	56.4	56.8	
win 17	81.3	74.0	56.7	59.6	
win 18	82.9	77.4	56.9	46.7	
win 19	84.9	76.2	55.2	51.4	
win 20	83.2	74.9	60.4	59.2	
win 21	84.8	78.4	55.3	56.6	
win 22	86.4	78.9	56.6	59.0	
win 23	85.1	74.9	61.5	63.0	
win 24	84.6	81.6	58.5	56.4	
win 25	82.3	82.5	50.6	50.9	
win 26	83.9	78.2	61.7	49.1	
win 27	82.5	79.4	49.6	50.0	
win 28	84.6	78.8	45.4	47.2	
win 29	87.0	80.6	47.3	49.0	
win 30	83.7	81.2	48.6	51.5	
win 31	85.3	83.7	47.0	47.7	
win 32	85.2	77.7	49.0	50.5	
win 33	86.8	85.4	47.9	49.3	
win 34	89.1	82.0	49.4	56.2	
win 35	86.1	78.3	56.3	57.7	
win 36	86.2	82.4	50.1	54.9	
win 37	86.8	83.0	53.9	55.5	
win 38	87.7	83.9	53.7	57.4	
win 39	87.5	83.3	59.4	56.8	
win 40	84.9	80.6	63.5	51.9	
Aircraft Characteristics	Length	3750	3750	3750	3750
	Wins	40	40	40	40
	Exits	2	2	2	2
	Exit1	780	780	780	780
	Exit2	3050	3050	3050	3050
	Exit3	3050	3050	3050	3050
	Em Exits	2	2	2	2
	EmEx1	1002	1002	1002	1002
	EmEx2	1709	1709	1709	1709
	x-loc	1217	1217	2456	2456
y-loc	206.8	206.8	206.8	206.8	
start (Hz)	1585	1585	138	138	
stop (Hz)	1585	1585	138	138	
pot (wh)	0	0	1	1	

A320: Vertical Polarization Data (cont.).

A320		Correction Factors									
ID	477	477	493	493	477	477	467	467	481	481	481
System	GS/P	GS/S	LC/P	LC/S	DM/EP	DM/ES	WH-L/P	WH-L/S	ALC-L/P	ALC-L/S	ALC/B/P
Pre-Amp	0	0	0	0	0	0	0	0	0	0	0
ACL	-8.8	-8.8	-4.9	-4.9	-15.7	-15.7	-5.2	-5.2	-16.4	-16.4	-16.4
Per-Amp	0	0	0	0	0	0	0	0	0	0	0
Kv Gain	1.03	1.03	-12.85	-12.85	5.32	5.32	-10.9	-10.9	4.85	4.85	4.85
Gain	19.23	19.23	9.28	9.28	17.12	17.12	10.9	10.9	15.95	15.95	15.95
win 1	47.1	41.5	58.3	54.6	52.8	52.7	46.3	48.9	52.8	60.2	52.8
win 2	47.1	41.5	54.4	54.6	51.7	58.0	50.8	46.3	53.5	63.8	56.8
win 3	43.9	38.2	66.8	54.2	50.9	54.2	39.2	44.3	57.9	59.9	53.9
win 4	46.9	41.1	64.4	60.2	51.7	54.6	42.7	48.0	56.1	56.6	55.5
win 5	46.2	45.5	62.5	59.5	51.7	54.8	24.3	42.1	52.3	58.9	58.1
win 6	42.4	43.9	61.0	55.5	53.5	53.8	45.3	44.2	51.3	59.3	55.5
win 7	48.2	47.8	68.6	61.6	53.8	53.1	45.9	41.6	44.9	62.6	57.8
win 8	44.4	43.2	61.7	55.5	54.1	56.0	43.5	47.0	47.0	51.6	54.0
win 9	44.0	44.5	65.1	63.7	56.2	56.3	43.2	46.0	45.8	55.6	54.5
win 10	47.4	47.7	64.5	58.5	56.7	53.7	44.8	42.0	46.8	54.5	56.8
win 11	49.1	44.1	63.7	58.3	53.0	54.9	45.9	42.3	46.0	58.7	52.6
win 12	44.8	48.7	66.6	57.9	55.8	53.5	45.9	50.0	47.3	57.3	56.8
win 13	44.5	45.3	66.5	58.6	53.7	56.4	43.8	44.5	46.7	57.5	54.5
win 14	45.8	48.7	75.3	59.8	54.3	58.9	45.5	45.2	46.7	54.6	55.2
win 15	52.3	49.9	77.6	67.1	53.0	56.9	36.7	40.8	48.4	57.6	52.7
win 16	48.5	48.9	71.6	61.7	54.2	55.3	34.6	35.4	49.0	56.7	52.7
win 17	48.5	48.9	70.6	61.7	54.2	55.3	34.6	35.4	46.8	55.5	51.9
win 18	48.9	46.3	59.8	52.4	53.7	56.4	31.8	30.9	48.2	58.2	60.6
win 19	47.3	51.0	72.3	56.3	55.4	58.8	43.1	43.9	51.7	55.8	57.5
win 20	53.0	50.1	68.7	63.2	56.2	58.5	44.1	47.4	49.0	58.5	55.8
win 21	47.5	49.2	72.0	63.2	56.3	59.1	43.2	43.5	48.8	58.6	57.7
win 22	47.1	48.5	66.8	64.6	58.6	58.6	42.2	42.8	46.4	55.6	57.5
win 23	53.3	52.1	74.0	74.0	51.0	62.7	46.8	47.7	48.7	54.3	56.4
win 24	46.3	51.2	71.4	68.0	58.9	62.0	46.1	45.5	46.6	55.3	57.0
win 25	48.6	48.9	69.1	65.5	47.2	61.5	45.9	43.4	48.3	56.2	59.1
win 26	57.3	52.0	75.8	69.3	58.9	63.7	46.6	46.4	51.5	57.3	58.5
win 27	51.9	48.1	74.0	76.3	58.3	63.9	45.0	46.0	49.9	57.5	59.2
win 28	51.2	47.9	73.3	67.3	55.8	63.4	42.1	43.1	50.2	56.7	59.0
win 29	57.4	52.3	74.5	73.3	59.9	66.1	42.1	43.5	51.8	56.7	60.4
win 30	48.5	50.3	70.5	74.5	58.5	60.9	47.2	44.4	50.8	54.1	60.7
win 31	49.8	48.0	70.7	65.3	59.3	60.7	46.2	43.7	49.8	58.3	59.2
win 32	52.4	50.8	71.9	72.0	62.0	60.6	47.1	44.7	50.6	57.8	59.8
win 33	55.1	51.1	67.8	67.4	68.8	60.9	46.6	45.2	51.1	56.7	61.2
win 34	54.4	49.3	67.6	63.3	55.6	64.6	42.7	44.7	51.8	56.5	57.5
win 35	57.6	52.4	70.4	69.3	58.9	62.4	46.2	46.7	53.9	58.3	60.7
win 36	53.5	51.1	67.8	68.8	58.8	59.9	45.7	47.5	53.1	56.0	62.2
win 37	50.3	47.8	69.7	66.5	56.9	61.5	44.8	43.7	51.4	57.5	56.0
win 38	53.5	49.7	75.0	69.9	57.5	60.2	48.6	46.9	51.9	57.3	55.4
win 39	51.5	53.4	62.3	62.3	58.2	60.4	46.3	48.9	53.5	57.9	58.6
win 40	50.8	51.7	69.4	67.7	58.7	61.1	45.5	44.0	53.6	58.6	58.9
Length	3750	3750	3750	3750	3750	3750	3750	3750	3750	3750	3750
Width	40	40	40	40	40	40	40	40	40	40	40
Exit	2	2	2	2	2	2	2	2	2	2	2
Exit1	780	780	780	780	780	780	780	780	780	780	780
Exit2	3050	3050	3050	3050	3050	3050	3050	3050	3050	3050	3050
Exit3	3050	3050	3050	3050	3050	3050	3050	3050	3050	3050	3050
Em Exit	2	2	2	2	2	2	2	2	2	2	2
EMERK1	1002	1002	1002	1002	1002	1002	1002	1002	1002	1002	1002
EMERK2	1709	1709	1709	1709	1709	1709	1709	1709	1709	1709	1709
KLOG	200	200	200	200	400	400	811	811	946	920	870
Y LOG	113	113	0	0	-206.8	206.8	206.8	206.8	206.8	206.8	-206.8
Start Freq	325	325	108	108	980	980	116	116	1020	1020	1020
stop Freq	340	340	113	113	1215	1215	138	138	1040	1040	1040

A320: Horizontal Polarization Data.

A320		467	467	493	493
Correction Factors	ID	467	467	493	493
	System	GPS(P)	GPS(S)	VHF-C(P)	VHF-C(S)
	Tx-Pwr	-30	-30	-10	-10
	Pre-Amp	0	0	0	0
	TCL	-21.4	-21.4	-5.2	-5.2
	ACL	0	0	0	0
	Pwr-Amp	37	37	37	37
	Tx-Gain	7.5	7.5	-10.9	-10.9
	Total	-5.9	-6.9	10.9	10.9
Window PL Data (Horizontal Polarization)	win 1	74.8	78.6	48.7	47.6
	win 2	77.7	79.7	55.5	51.3
	win 3	78.8	80.3	46.7	49.0
	win 4	77.5	77.7	54.1	49.8
	win 5	80.9	80.9	45.3	47.7
	win 6	83.0	82.6	47.9	48.5
	win 7	79.0	81.0	52.4	50.1
	win 8	83.9	80.8	45.4	49.5
	win 9	82.7	82.0	48.7	47.0
	win 10	84.6	81.6	43.3	44.4
	win 11	83.4	83.5	47.0	45.8
	win 12	82.8	80.5	53.1	46.5
	win 13	82.6	78.5	44.9	45.7
	win 14	82.3	81.5	45.7	47.9
	win 15	82.9	83.2	45.9	47.6
	win 16	84.0	83.6	37.6	36.1
	win 17	84.7	81.7	37.7	34.3
	win 18	85.5	80.8	34.5	29.4
	win 19	85.6	82.7	38.8	47.2
	win 20	85.6	80.7	52.7	52.6
	win 21	84.4	80.8	26.1	47.9
	win 22	87.9	84.7	47.1	46.4
	win 23	86.9	85.9	51.6	52.0
	win 24	88.6	82.4	45.4	48.7
	win 25	85.8	82.2	47.3	44.9
	win 26	87.5	87.6	47.6	47.6
	win 27	87.9	84.3	50.9	51.3
	win 28	86.7	89.0	57.5	55.4
	win 29	87.8	82.8	53.5	53.6
	win 30	85.5	84.0	47.1	51.1
	win 31	90.1	85.9	45.3	47.3
	win 32	86.1	83.3	44.6	46.8
	win 33	87.2	87.4	44.1	44.6
	win 34	87.1	84.6	42.9	44.8
	win 35	88.3	86.0	45.2	44.0
	win 36	84.4	85.3	44.5	46.9
	win 37	85.6	84.8	41.5	43.5
	win 38	88.6	88.2	44.4	47.3
	win 39	85.6	85.7	46.8	48.0
	win 40	87.3	89.9	43.0	43.3
Aircraft Characteristics	Length	3750	3750	3750	3750
	Wins	40	40	40	40
	Exits	2	2	2	2
	Exit1	780	780	780	780
	Exit2	3050	3050	3050	3050
	Exit3	3050	3050	3050	3050
	Em Exits	2	2	2	2
	EmEx1	1002	1002	1002	1002
	EmEx2	1709	1709	1709	1709
	x-loc	1217	1217	2456	2456
y-loc	206.8	206.8	206.8	206.8	
start (Hz)	1585	1585	116	116	
stop (Hz)	1585	1585	138	138	
pol (VH)	0	0	1	1	

A320: Horizontal Polarization Data (cont.).

BIBLIOGRAPHY

- [1] L. Ljung, *System Identification: Theory for the User*. Prentice Hall PTR, 1999.
- [2] L. Ljung; and T. Glad, "Modeling of Dynamic Systems," Prentice Hall PTR, pp. 14-15, 1994.
- [3] C. Hafner, *The Generalized Multipole Technique for Computational Electromagnetics*. Boston: Artech House, 1990.
- [4] T. K. Sarkar, "The Conjugate Gradient Method as Applied to Electromagnetic Field Problems," *IEEE Antennas and Prop. Soc. Newsletter*, vol. 28, pp. 5-14, 1986.
- [5] E. H. Newman and D. M. Pozar, "Electromagnetic Modeling of Composite Wire and Surface Geometries," *IEEE Trans. Antenna Prop.*, vol. AP-26, pp. 784-789, 1978.
- [6] R. G. Kououmjian and P. H. Pathak, "A Uniform Geometrical Theory of Diffraction for an Edge in Perfectly Conducting Surface," *Proc. IEEE*, vol. 62, pp. 1448-1461, 1974.
- [7] P. P. Silvester and R. L. Ferrari, *Finite Elements for Electrical Engineers*, 2nd ed. Cambridge: Cambridge University Press, 1990.
- [8] G. L. Maile, "Three-Dimensional Analysis of Electromagnetic Problems by Finite Element Methods," in *Electrical Engineering*: University of Cambridge, 1979.
- [9] A. V. S. Rao and D. K. Pratihari, "Fuzzy-logic-based Expert System to Predict Results of Finite Element Analysis," *Knowledge-Based Systems*, vol. 20, pp. 37-50, 2007.
- [10] J. P. Webb, "Developments in a Finite Element Method for Three-Dimensional Electromagnetic Problems," in *Electrical Engineering*: University of Cambridge, 1981.
- [11] N. K. Uzunoglu, K. S. Nikita, D. I. Kaklamani, and North Atlantic Treaty Organization. Scientific Affairs Division., *Applied computational electromagnetics : state of the art and future trends*. Berlin ; New York: Springer, 2000.

- [12] *MAXWELL 3D*. Finite Element Software. Ansoft Corporation, Pittsburg, <http://www.ansoft.com/products/em/max3d/>, 2007.
- [13] R. F. Harrington, *Field Computation by Moment Methods*. New York: The Macmillan Co., 1968.
- [14] "MiniNEC." Method of Moments Software. Norwood: Artech House Publishers, <http://www.emsci.com/Mininec.htm>, 1992.
- [15] G. J. Burke and A. J. Poggio, "Numerical Electromagnetic Code (NED)," in *NOSC Tech. Document 116*. San Diego: Naval Ocean Syst. Center, 1981.
- [16] D. R. Wilton and S. U. Hwu, "Junction Code User's Manual," in *NOSC Tech. Document 1324*. San Diego: Naval Ocean Syst. Center, 1988.
- [17] R. Holland, V. P. Cable, and L. Wilson, "A 2-D Finite-Volume Time-Domain Technique for RCS Evaluation," *Proc. 7th Annual Rev. of Progress in Applied Computational Electromanetics*, pp. 667-681, 1991.
- [18] W. J. Hoefler, *The Electromagnetic Wave Simulator: A Dynamic Visual Electromagnetic Laboratory Based on the Two Dimensional TLM Method*. West Sussex, England: John Wiley & Sons, 1991.
- [19] P. B. Johns, "A Symmetrical Condensed Node for the TLM Method," *IEEE Trans. Microwave Theory Tech.*, vol. MTT-35, pp. 370-377, 1987.
- [20] L. A. Zadeh, "Fuzzy Sets," *Information and Controls*, vol. 8, pp. 338-352, 1965.
- [21] H. J. Zimmermann, *Fuzzy Set Theory and its Applications*, 4th ed: Kluwer Academic Publishers, 2001.
- [22] M. Tayarani, "A New Modeling Approach in Engineering Electromagnetics using Fuzzy Inference," *International Symposium on Electromagnetic Compatibility*, pp. 106-109, 1999.
- [23] M. Jafri, "Fuzzy Modeling of Electromagnetic Emissions from Portable Electronic Devices Onboard Commercial Aircraft," in *Electrical Engineering*. Norfolk: Old Dominion University, 2004.
- [24] S. Haykin, *Neural Networks: A comprehensive foundation*, 2nd ed: Prentice Hall Inc., 1999.
- [25] S. Abe, *Pattern Classification: Neuro-fuzzy methods and their comparison*. London: Springer-Verlag, 2001.

- [26] Q. J. Zhang and K. C. Gupta, *Neural Networks for RF and Microwave Design*. Norwood, MA: Artech House, 2000.
- [27] M. Jafri, J. Ely, and L. Vahala, "Classification and Prediction of Interference Pathloss Measurements inside B757 Using Feed Forward Neural Networks," *IEEE Conference on Electromagnetic Field Computation*, 2006.
- [28] M. Jafri, J. Ely, and L. Vahala, "Classification and Prediction of RF Coupling Inside A320 and A319 Airplanes Using Feed Forward Neural Networks," *25th Digital Avionics Systems Conference*, 2006.
- [29] "Report of Electromagnetic Compatibility Between Passenger Carried Portable Electronic Devices (PEDs) and Aircraft Systems.," in *ED-118: EUROCAE*, 2003.
- [30] L. Li, J. Xie, O. Ramahi, M. Pecht, and B. Donham, "Airborne Operation of Portable Electronic Devices," in *IEEE Antennas and Propagation*, vol. 44, 2004.
- [31] B. Donham, "Electromagnetic Interference from Passenger-Carried Portable Electronic Devices," in *Boeing Aeromagazine*, pp. 13-18, 2000.
- [32] "Code of Federal Regulations, Title 14, Chapters I and III: Federal Aviation Regulations, Section 91.21." 2007.
- [33] P. Ladkin, "Electromagnetic Interference with Aircraft Systems: Why Worry?," University of Bielefeld Article RVS-J-97-03, 1997.
- [34] "Portable Electronic Devices Carried on Board Aircraft," <http://aviation-safety.net/airlinesafety/exits/>, 1996.
- [35] "Use of Portable Electronic Devices Aboard Aircraft," FAA Advisory Circular 91.21-1A, 2006.
- [36] "Telecommunication: Public Mobile Services: Prohibition on Airborne Operation of Cellular Phones," Code of Federal Regulations, Title 47, Part 22, Section 22.925. 2007
- [37] "Interference to Aircraft Electronic Equipment from Devices Carried Aboard," RTCA Document DO-119, 1963.
- [38] "Potential Interference to Aircraft Electronic Equipment from Devices Carried Aboard," RTCA Document DO-199, 1988.
- [39] "Portable Electronic Devices Carried On Board Aircraft," RTCA Document DO-233, 1996.

- [40] "Database Report Set - Passenger Electronic Devices," NASA Aviation Safety Reporting System, 2000.
- [41] B. Strauss, "Avionics Interference from Portable Electronic Devices: Review of the Aviation Safety Reporting System Database," presented at Proceedings of the 21st Digital Avionics Systems Conference, 2002.
- [42] M. Jafri, J. Ely, and L. Vahala, "Graphical and Statistical Analysis of Airplane Passenger Cabin RF Coupling Paths to Avionics," presented at 22nd Digital Avionics Systems Conference, 2003.
- [43] M. Jafri, J. Ely, and L. Vahala, "Fuzzification of Electromagnetic Interference Patterns Onboard Commercial Airliners Due to Wireless Technology," *IEEE Antennas and Prop.*, 2004.
- [44] T. Perry and L. Geppert, "Do Portable Electronics Endanger Flight?," in *IEEE Spectrum*, 2003.
- [45] "Aviation Safety Network." <http://aviation-safety.net/airlinesafety/exits/>
- [46] L. Vahala and T. Nguyen, "Effect of Lag Correlation on the Statistical Modeling of Wave Propagation in a Complex Cavity," *IEEE Antennas and Prop.*, 2004.
- [47] R. W. Devereux and B. Archambeault, "Electromagnetic Analytical Modeling Used to Aid Aircraft EMI Data Analysis," *IEEE*, 1998.
- [48] S. V. Georgakopoulos, C. R. Birtcher, C. A. Balanis, and R. A. Renaut, "HIRF Penetration and PED Coupling Analysis for Scaled Fuselage Models Using a Hybrid Subgrid FDTD(2,2)/FDTD(2,4) Method," *IEEE Transactions on Electromagnetic Compatibility*, vol. 45, 2003.
- [49] C. R. Birtcher, S. V. Georgakopoulos, and C. A. Balanis, "In-Flight EMI from Portable Electronic Devices (PEDs): FDTD Prediction vs. Measurements," *IEEE*, 2002.
- [50] R. W. Devereux, B. Archambeault, and G. L. Fuller, "Assessment of Analytical Codes for Use in Modeling Aircraft Onboard EMI Threats," presented at 16th Digital Avionics Systems Conference Proceedings, 1997.
- [51] F. S. Adana, O. G. Blanco, I. G. Diego, J. P. Arriaga, and M. F. Catedra, "Propagation Model Based on Ray Tracing for the Design of Personal

- Communication Systems in Indoor Environments," *IEEE Transactions on Vehicular Technology*, vol. 49, pp. 2105 - 2112, 2000.
- [52] Z. Ji, B. H. Li, H. X. Wang, H. Y. Chen, and Y. G. Zhou, "A New Indoor Ray-Tracing Propagation Prediction Model," Shanghai Jiao-Tong University, 2003.
- [53] A. R. Lopez, "The Geometrical Theory of Diffraction Applied to Antenna Pattern and Impedance Calculations," *IEEE Transactions on Antennas and Propagation*, vol. AP-14, 1966.
- [54] R. J. W. D. H. Martic, R. J. Martin, "The Use of the Geometrical Theory of Diffraction in the Calculation of Antenna Patterns of Sub-millimeter and Millimeter-wave radiometers," *International Journal of Infrared and Millimeter Waves*, vol. 9, 1988.
- [55] L. Vahala and T. Nguyen, "Extension of the Multi-Scattering Approach to Stochastic Polarized Wave Propagation in Complex Cavities," *IEEE Antennas and Prop.*, 2005.
- [56] L. Vahala and T. Nguyen, "Random Wave Propagation in a Two-Dimensional Complex Medium," *IEEE Antennas and Prop.*, 2003.
- [57] S. Sefi and F. Bergholm, "Extrapolation and Modeling of Method of Moments Currents on a PEC Surface," Royal Institute of Technology, 2005.
- [58] W. D. Rawle and S. Aerospace, "The Method of Moments: A Numerical Technique for Wire Antenna Design," in *High Frequencies Electronics*, 2006.
- [59] S. E. Metker, R. J. Luebbers, M. Chevalier, J. W. Schuster, H. S. Langdon, and M. Bushbeck, "Finite Difference Time Domain Modeling of an Indoor Antenna Chamber with Phased Planar Array," *IEEE*, 1997.
- [60] C. M. Furse, Q. Yu, and O. P. Gandhi, "Validation of the Finite Difference Time Domain Method for Near-field Biomagnetic Simulations," *Microwave and Optical Technology Letters*, vol. 16, 1997.
- [61] "B737- Schematics," Boeing.
<http://www.boeing.com/commercial/airports/acaps/737sec2.pdf>
- [62] "B757- Schematics," Boeing.
<http://www.boeing.com/commercial/airports/acaps/753sec2.pdf>

- [63] "A319- Schematics." Airbus.
http://www.aad.gov.au/MediaLibrary/asset/mediaitems/ml_390314724537037_A319-drawing.gif
- [64] "A320- Schematics." Airbus.
<http://www.ana.co.jp/eng/aboutana/corporate/galleryclassi/1983/image/320.gif>
- [65] L. W. Li, M. S. Leong, T. S. Yeo, and P. S. Kooi, "Electromagnetic Dyadic Green's Functions in Spectral Domain for Multilayered Cylinders," *J. Electromagnetic Waves Application*, vol. 14, pp. 961-986, 2000.
- [66] S. Sykora, "Approximations of Ellipse Perimeters and a Complete Elliptical Integral $E(x)$ (Review of known formulae)," in *Stan's Library*, 1 ed. Castano Primo, 2005.
- [67] "MATLAB 7: The Language of Technical Computing," 7.1.0.246 (R14) Service Pack 3 ed., 2005.

VITA

Madiha Jamil Jafri, born in Riyadh, Saudi Arabia, on August 15, 1982, is the daughter of Ghazala Siraj Jafri and Syed Jamil A. Jafri. After completing her work at Maury High School, Norfolk, Virginia, in 1999, she entered Virginia Polytechnic Institute and State University at Blacksburg, Virginia. In 2001, she transferred to Old Dominion University at Norfolk, Virginia, where she received various scholarships to initiate her work on Electromagnetics at NASA Langley Research Center, Hampton, Virginia, with Mr. Jay Ely as the mentor. She received the degree of Bachelor of Science with a major in Computer Engineering from Old Dominion University in December 2003. She received Master of Science degree in Electrical Engineering from Old Dominion University in August 2004, with Dr. Linda Vahala as the advisor. In December 2004, she married Hamid Mahmood of Philadelphia. While pursuing the Doctorate of Philosophy program in Electrical Engineering at Old Dominion University since 2004, she also enrolled in a Post Doctoral program in Biomedical Engineering at Olin Neuropsychiatry Research Center, Hartford, Connecticut, with Dr. Vincent Calhoun from Yale University. In 2007, she completed her doctoral degree as well as postdoctoral research and joined Lockheed Martin Corporation as a Systems Engineer, with expertise in Modeling and Simulation, Electromagnetics, Probability and Statistics as well as Cryptography.

Permanent Address

43 Woodduck Drive, Mullica Hill, NJ 08062

Scholarships/ Grants

Graduate Student Research Proposal Grant	(2003 – 2007)
Virginia Space Grant Consortium	(2001 – 2003)
NASA Langley Research Student Scholar	(2001 – 2002)
CSEM Scholarship	(2001 – 2003)
Bradley Scholarship for Computer Engineers	(2000 – 2001)
ACCESS Scholarship	(1999 – 2001)
PRATT Engineering Scholarship	(1999 – 2001)
Pamplin Leadership Award	(1999 – 2001)

Publications/ Proceedings

- M. Jafri, M. Stevens, G. Pearlson and V. Calhoun. "A Method of Functional Connectivity Among Spatially Independent Resting-State Components in Schizophrenia." *NeuroImage*, 2007. (*in press*)
- M. Jafri, J. Ely, and L. Vahala. "Prediction of Interference Pathloss Inside B737 and B757 Using Modulated Fuzzy Logic and Neural Networks." *IEEE DASC*, Dallas, TX, 2007.
- M. Jafri, J. Ely, and L. Vahala. "Prediction of Interference Pathloss Inside A319 and A320 Using Modulated Fuzzy Logic and Neural Networks." *IEEE NAFIPS*, San Diego, CA, 2007.
- M. Jafri, G. Pearlson, and V. Calhoun. "Resting State Functional Connectivity Among ICA Components Using Bayesian Networks." *OHBM*, Chicago, IL, 2007.
- M. Jafri, G. Pearlson, and V. Calhoun. "Investigations into Resting-State Networks in Schizophrenia using Independent Component Analysis." *ISMRM*, Berlin, Germany, 2007.
- M. Jafri, G. Pearlson, and V. Calhoun. "A Maximal-Correlation Approach Using ICA for Testing Functional Network Connectivity Applied to Schizophrenia." *IEEE ISBI*, Washington, DC, 2007.
- M. Jafri, J. Ely, and L. Vahala. "Classification and Prediction of RF Coupling Inside A320 and A319 Airplanes using Feed Forward Neural Networks." *DASC*, Portland, OR, 2006.
- M. Jafri, G. Pearlson, and V. Calhoun. "Functional Classification of Schizophrenia using Feed Forward Neural Networks." *IEEE EMBC*. New York, NY 2006.
- M. Jafri, J. Ely, and L. Vahala. "Classification and Prediction of Interference Pathloss Measurements Inside B757 Using Feed Forward Neural Networks." *IEEE CEFC*, Miami, FL, 2006.
- M. Jafri, J. Ely, and L. Vahala. "Graphical Analysis of Electromagnetic Coupling on B737 and B757 Aircraft for VOR and LOC IPL Data." *IEEE ACES*, Honolulu, HI, 2005.
- M. Jafri, J. Ely, and L. Vahala. "Comparative Analysis of Interference Pathloss Coupling Patterns on B737 vs. B757 Airplanes." *DASC*, Washington, DC, 2005.

- M. Jafri, J. Ely, and L. Vahala. "Graphical Analysis of B737 Airplane Pathloss Data for GPS and Evaluation of Coupling Mitigation Techniques." *IEEE EMC*, Santa Clara, CA, 2004.
- M. Jafri, J. Ely, and L. Vahala. "Fuzzification of Electromagnetic Interference Patterns Onboard Commercial Airliners Due to Wireless Technology." *IEEE APS*, Monterey, CA 2004.
- M. Jafri, J. Ely, and L. Vahala. "Graphical and Statistical Analysis of Airplane Passenger Cabin RF Coupling Paths to Avionics." *DASC*, Indianapolis, IN 2003.
- M. Jafri, J. Ely, and L. Vahala. "Graphical Representation of the Effects of Antenna Locations on Pathloss Data." *IEEE APS*, Columbus, OH, 2003.